Efficient Multiconfigurational Time-Dependent Simulation of Conjugated Polymers

Rafael Peixoto Miranda

A thesis submitted in partial fulfillment of
the requirements for the degree of Doctor of Philosophy

November, 2014

I, Rafael Peixoto Miranda, confirm that the work presented in this thesis is my own. Where information has been derived from other sources, I confirm that this has been indicated through an appropriate reference.

Abstract

Conjugated polymers have become an important class of functional materials for a wide range of optoelectronic applications, from which polymer-based solar cells stand out as one of the most promising new devices. While experimental progress has been made at a good pace over the last couple of decades, the fundamental processes governing the photophysics of conjugated polymers are not yet completely understood.

A theoretical description is challenging, since these systems exhibit both strong electron-electron and electron-nuclear interactions. A detailed understanding of the photoexcitation process, and of the steps following photoexcitation, requires a nonadiabatic treatment of the electron-nuclear dynamics, and a proper description of the excited electronic states and interchain interactions, for which many-body effects are important. Some of these ingredients have often been neglected in dynamical calculations. In particular, most studies which include electron-electron interactions have ignored the singlet character of the photoexcited state, by restricting the wavefunction to the form of a single Slater determinant.

In this thesis, we develop a nonadiabatic molecular dynamics method which allows for the coupled evolution of the nuclear degrees of freedom and of multiconfigurational electronic wavefunctions. The proposed scheme effectively establishes a compromise between efficiency and accuracy, which enables the study of large systems. Furthermore, it is designed to take into account the appropriate spin symmetry of the electronic wavefunction, thus allowing us to distinguish between singlet and triplet excited states, which exhibit quite different properties.

The formalism is applied to semiempirical single- and double-strand models of a prototypical conjugated polymer, in order to investigate the effects of Coulomb in-

teractions and interchain coupling on the dynamics of low-lying excitations. The nature of the photoexcited states and the issue of charge photogeneration in conjugated polymers are also addressed, as well as the charge transfer process at donor/acceptor interfaces.

Acknowledgements

First and foremost, I would like to thank my supervisors, Prof. Andrew Fisher and Dr. Andrew Horsfield, for their enthusiastic guidance, invaluable words of advice, and incredible patience towards my utter disregard for deadlines. I feel very fortunate for having had the opportunity to work closely with such talented and accomplished scholars.

I am also grateful to my senior colleague, and esteemed friend, Lorenzo Stella, for his many constructive comments and suggestions which have helped immensely to develop the ideas in this thesis. His willingness to put aside his own demanding work whenever I needed assistance has been very much appreciated.

I further wish to thank the remaining members and collaborators of the "Materials Modelling Initiative" consortium at University College London, Imperial College London, and Queen's University Belfast, for numerous useful discussions. The generous financial support of the Engineering and Physical Sciences Research Council is also gratefully acknowledged.

On the personal side, I would like to thank the many wonderful people I have met during my time at the London Centre for Nanotechnology, all of whom have contributed to make London feel like home. I am especially grateful to Flemming, Wisdom, Hoi, Angie, Aida, Marc, Mathew, and Alex, for the countless hours of fun and adventure which have helped keeping me sane and cheerful.

Finally, I wish to thank my parents, Lídia and António, and my brother, Vasco, for their unconditional support and encouragement to pursue my interests.

List of publications

The work presented in this thesis has been partly published in the following journal articles:

- R. P. Miranda, A. J. Fisher, L. Stella, and A. P. Horsfield, "A multiconfigurational time-dependent Hartree-Fock method for excited electronic states. I. General formalism and application to open-shell states", *Journal of Chemical Physics* **134**, 244101 (2011)

- R. P. Miranda, A. J. Fisher, L. Stella, and A. P. Horsfield, "A multiconfigurational time-dependent Hartree-Fock method for excited electronic states. II. Coulomb interaction effects in single conjugated polymer chains", *Journal of Chemical Physics* **134**, 244102 (2011)

- E. J. McEniry, Y. Wang, D. Dundas, T. N. Todorov, L. Stella, R. P. Miranda, A. J. Fisher, A. P. Horsfield, C. P. Race, D. R. Mason, W. M. C. Foulkes, and A. P. Sutton, "Modelling non-adiabatic processes using correlated electron-ion dynamics", *European Physical Journal B* **77**, 305 (2010)

Contents

Part I

Introduction

Chapter 1

Overview

1.1 Motivation

Until the late 1970s, it was thought that all carbon-based polymers were insulators, and any manifestation of electrical conductivity in polymers was generally regarded as a nuisance. Indeed, this property inherent of *plastics* has long been exploited by the electronics industry, primarily for inactive packaging and insulating purposes. However, the discovery, in 1977, of a new family of polymers that exhibit high electrical conductivity [1, 2] changed this limited perspective and established a new field of research, which continues to grow to this day. Although still at the outset, the potential applications of these novel materials, known as *conjugated polymers*, *intrinsically conductive polymers*, or *synthetic metals*, are quite significant.

The unique properties of conjugated polymers arise from the presence of alternating single and double or triple bonds along the polymer backbone, which leads to electron delocalisation and allows the charge carriers to move throughout the chain. While exhibiting the electrical and optical properties of metals or semiconductors, they retain the advantages of conventional insulating polymers: mechanical flexibility and ease of processing. Organic devices using conjugated polymers as active components are expected to rival their inorganic counterparts, particularly in applications that require flexibility or fitting to extensive surfaces, or for those which would benefit from the reduced cost of large-scale manufacturing [3, 4].

Numerous electrical and optical organic devices relying on the properties of conjugated polymers have already been demonstrated. These include mechanical actuators [5], batteries [6], photochromic [7] and electrochromic [8] devices, lasers [9, 10], light-emitting electrochemical cells [11], light-emitting diodes [12–15], biological and chemical sensors [16, 17], field-effect transistors [18–20], photodetectors [21], and solar cells [22–34].

Polymer-based solar cells are one of the most promising new devices. The demands for cheaper and cleaner energy sources have driven major research efforts to develop this technology, which exploits the semiconducting properties of conjugated polymers to generate electrical current from incident light. By using conjugated polymers, it is possible to produce lightweight and flexible devices at a fraction of the cost of current silicon-based technology. On the downside, these organic devices still struggle with uncompetitive power-conversion efficiencies, limited stability, and degradation issues [33, 34].

Progress in this new technology has been essentially empirical. Early devices, based solely on a *single layer* of polymer sandwiched between two electrodes, showed extremely poor performances, with power-conversion efficiencies of the order of 0.001% [22, 23]. A significant breakthrough, which revolutionised the design of polymer-based solar cells, was achieved in the early 1990s with the discovery of ultrafast photoinduced charge transfer in composites of conjugated polymers as donors and fullerene or its derivatives as acceptors [35, 36]. The efficiencies of the first devices produced from polymer/fullerene composites, arranged in a *bilayer* or *planar heterojunction* structure, were almost two orders of magnitude higher than those of single layer devices [24, 25], a figure still unsatisfactory for practical applications. It was later realised that blending a suitable fullerene derivative directly into the conjugated polymer film, thus forming an *interpenetrating donor/acceptor network* or *bulk heterojunction*, was an improved solution [26]. The resulting cells had a power-conversion efficiency of about 1%, as a consequence of the increased donor/acceptor interfacial area and charge transfer efficiency [26]. Over the past decades, the performance of polymer-based solar cells has continued to improve, through the optimisation of the film morphology [27], the introduction of *optical spacers* [28] and

tandem architectures [29], and, more recently, the use of *alternating copolymers* [30–32], specifically designed to increase the spectral coverage of the solar radiation. The efficiency of state-of-the-art polymer/fullerene bulk heterojunction solar cells is now above 10% [32], and approaching the limit of commercial viability [34]. But before the widespread use of these cells becomes a reality, the efficiency will have to be further increased. Also, achieving long-term environmental stability remains an important challenge that will have to be tackled [33, 34].

Despite all the technological developments, the fundamental processes underlying the operation of organic donor/acceptor solar cells are not yet completely understood. It is generally agreed that one of the limiting factors to the efficiency is the lack of an optimised charge transfer at the polymer/fullerene interface [33, 34], but the precise mechanism which governs the charge transfer process is still elusive [37]. Moreover, the nature of the photoexcited states in conjugated polymers is particularly controversial [38–43]. A central question, that theory has yet to reconcile with experiments, pertains to the time scale and efficiency of charge carrier photogeneration. The presence of free charges is evidenced by photoconductivity measurements [38], but it is unclear whether the carriers are created on ultrafast time scales, or produced on longer time scales through the dissociation of bound electron-hole pairs, i.e., excitons. Achieving a theoretical understanding of these elementary processes is not only of academic interest, but can also have a practical impact on improving the performance of organic devices such as polymer-based solar cells.

1.2 Aims and objectives

The theoretical treatment of the photophysics of conjugated polymers and polymer/fullerene composites is challenging, since these systems exhibit both strong electron-electron and electron-nuclear interactions. The coupling between the electrons and the nuclei leads to a rich variety of nonlinear excitations [44–46], such as solitons and polarons, a characteristic feature which establishes an important distinction between conjugated compounds and inorganic semiconductors. On the other

hand, electron correlation effects have a drastic influence on the electronic structure, playing a crucial role in determining the energetic ordering of the electronic states [45], which explains why not all conjugated polymers luminesce. Thus, both types of interactions are essential to describe the behaviour of conjugated systems.

A detailed understanding of the photoexcitation process, and of the steps following photoexcitation, requires a nonadiabatic treatment of the electron-nuclear dynamics, and a proper description of the excited electronic states and interchain interactions, for which many-body effects are important. Some of these ingredients have often been neglected in photoexcitation dynamics calculations [43, 47–56]. In particular, most studies which include electron-electron interactions have ignored the singlet character of the photoexcited state [53–56], by restricting the wavefunction to the form of a single Slater determinant. The present research aims at bridging this gap, and achieving a better understanding of the photophysics of conjugated polymers and polymer/fullerene composites. To this end, we define the following objectives:

1) To develop a nonadiabatic molecular dynamics method which allows for the coupled evolution of the nuclear degrees of freedom and of multiconfigurational electronic wavefunctions, thus capturing the proper spin symmetry of photoexcited states;

2) To assess the importance of electron-electron interactions on the dynamics of low-lying excitations in conjugated polymers, by applying the method to semiempirical models with and without Coulomb interactions;

3) To investigate the effect of interchain coupling on the dynamics of photoexcitations in conjugated polymers, by applying the method to semiempirical models which include interchain interactions;

4) To study the nature of the photoexcited states and address the question of charge photogeneration in conjugated polymers (both in dilute solution and in the dense form);

5) To study the charge transfer dynamics at donor/acceptor interfaces and assess the conditions which lead to an optimised charge transfer process.

1.3 Outline

This thesis is divided into four parts and nine chapters, which are now briefly outlined. The remainder of this first part introduces the basic concepts of conjugated polymers and some of the terminology used throughout the thesis (chapter 2). Part II presents the analytical framework and the various methodological tools required for the efficient simulation of excited-state dynamics in conjugated polymers. Chapter 3 is devoted to a discussion of the approximations leading to simple semiempirical models, which have been successfully used to study the properties of conjugated polymers. Chapter 4 deals with the approximate solution of the time-independent Schrödinger equation, which is necessary for setting up the initial conditions of a time-dependent simulation. The Hartree-Fock method is derived in detail, and self-consistent field algorithms are briefly surveyed. Chapter 5 provides a derivation of the Ehrenfest molecular dynamics and the multiconfigurational time-dependent Hartree-Fock methods. When combined, these schemes provide a powerful tool to study the dynamics of photoexcited states. The resulting formalism is applied to the dynamics of low-lying excitations in conjugated polymers and polymer/fullerene composites in part III. In chapter 6, we focus on the effects of electron-electron interactions, by comparing results obtained using single-strand models of a prototypical conjugated polymer, both with and without Coulomb interactions. In chapter 7, we turn to the effects of interchain interactions, by investigating a double-strand model of the same prototypical polymer, considering different regimes of the interchain coupling strength. Both of these chapters also discuss the nature of the photoexcited states and the issue of charge photogeneration. Chapter 8 is devoted to the study of charge transfer dynamics at donor/acceptor interfaces. By varying several key parameters of a coupled-chain model, the conditions which lead to an optimised charge transfer process are assessed. Finally, in the last part, we summarise our main conclusions and discuss possible future research directions (chapter 9).

Chapter 2

Basic concepts of conjugated polymers

2.1 Chemical structure

The carbon atom has the ground state configuration $1s^2\,2s^2\,2p^2$, with four electrons in the valence orbitals. In the vicinity of other atoms, these levels may hybridise into *sp*, sp^2, or sp^3 orbitals, in order to maximise the overlap with adjacent wavefunctions, thus leading to a chemically stable bond [45, 57]. For instance, in *saturated polymers*, the valence orbitals hybridise into the sp^3 configuration, shown in figure 2.1(a), and each carbon forms bonds with four surrounding atoms. The classical example is polyethylene, whose chemical structure is depicted in figure 2.1(b). In this macromolecule, the sp^3 hybrids overlap with similar wavefunctions

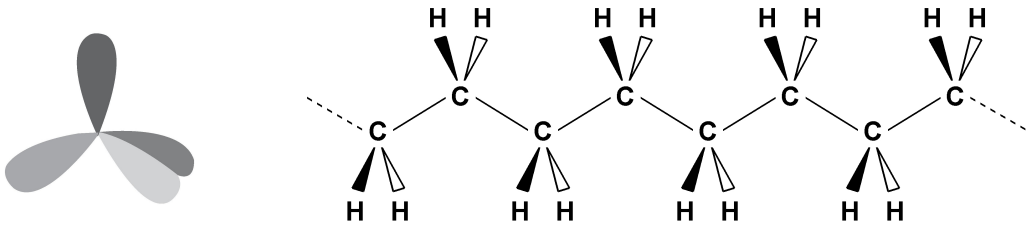

(a) *(b)*

Figure 2.1: sp^3 orbital hybridisation (a), and the chemical structure of polyethylene (b), a saturated polymer.

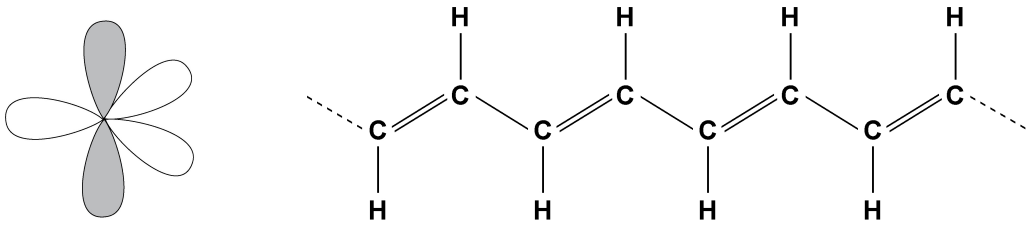

(a) *(b)*

Figure 2.2: $sp^2\,p_z$ orbital hybridisation (a), and the chemical structure of trans*-polyacetylene (b), a conjugated polymer.*

on neighbouring carbon atoms, and also with the $1\,s$ orbitals on adjacent hydrogen atoms, forming molecular *σ-bonds*, which are highly directional and have a strong covalent character [45, 57]. The lowest excitations in saturated polymers are created by transferring an electron from a bonding σ-orbital to an antibonding σ^*-orbital, for which a large amount of energy is required. Hence, there is a large energy gap separating the valence and conduction bands, and these materials are insulators.

In *conjugated polymers*, on the other hand, the valence orbitals are typically sp^2 hybridised [unshaded lobes in figure 2.2(a)], and every carbon forms bonds with only three other atoms. The chemical structure of the prototype of this class of materials, *trans*-polyacetylene, is depicted in figure 2.2(b). In this linear polyene, two of the sp^2 orbitals give rise to covalent σ-bonds with surrounding carbon atoms, while the third sp^2 hybrid leads to a covalent σ-bond with the hydrogen $1\,s$ orbital. The remaining unhybridised p_z orbitals [shaded lobes in figure 2.2(a)], which lie perpendicular to the sp^2 hybrids, overlap in a sideways manner to form molecular *π-bonds*, resulting in a structure of alternating single and double bonds [45, 57]. Since the π-bonds are weak, the positions of the single and double bonds may interchange at small or no energy cost. The π-electrons in a conjugated polymer are thus delocalised throughout the entire chain, whereas the electrons in the σ-orbitals are strongly localised [45, 57]. Furthermore, the energy required to promote an electron from a bonding π-orbital to an antibonding π^*-orbital is much lower than the energy needed to produce a $\sigma \rightarrow \sigma^*$ excitation. Conjugated polymers are typically semiconductors with an energy gap between 1 and 3 eV [45, 57], a range

similar to that of conventional inorganic semiconductors. The chemical structures of some of the conjugated polymers most frequently encountered in the literature are shown in figure 2.3.

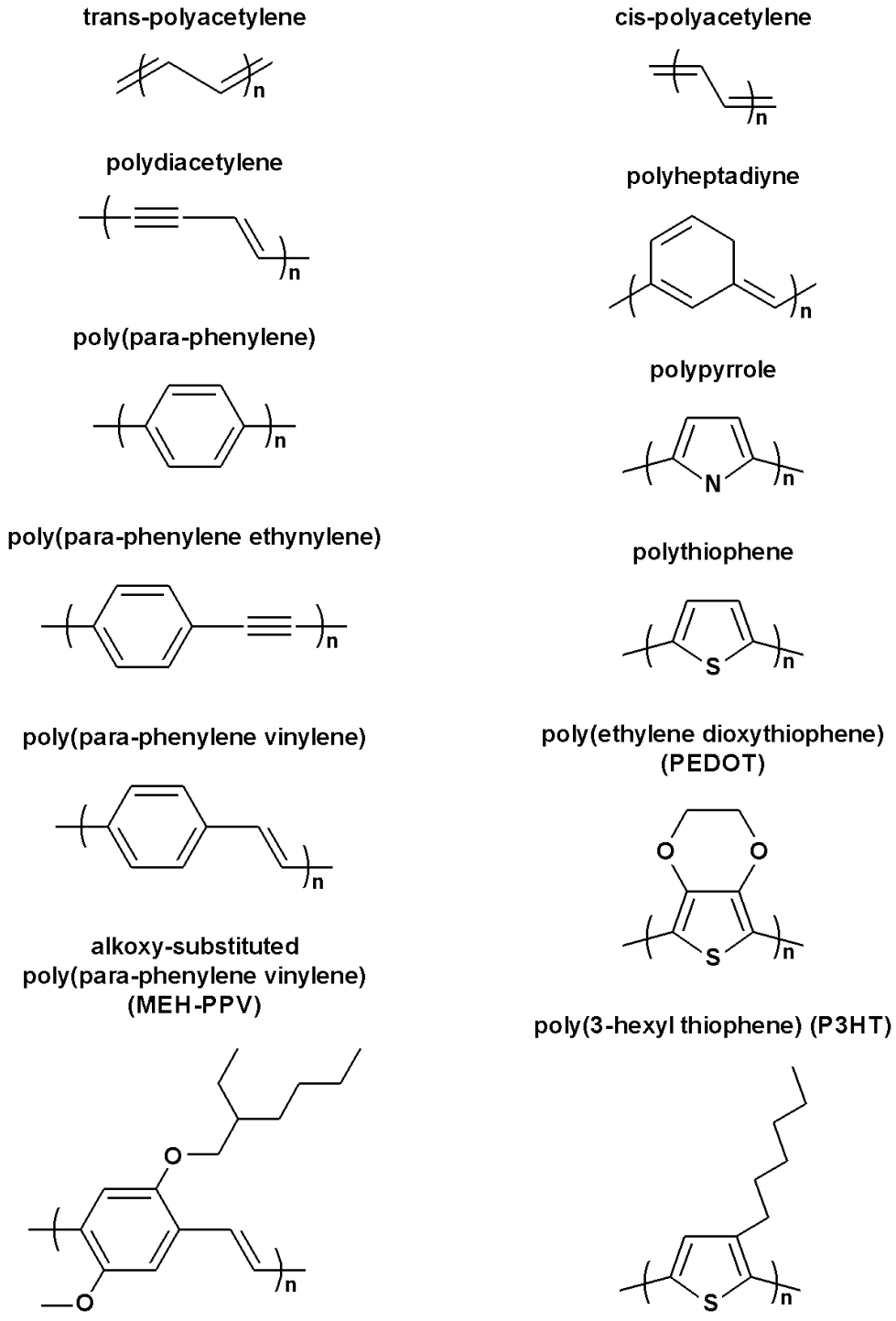

Figure 2.3: Chemical structures of some frequently studied conjugated polymers.

2.2 Symmetry and ordering of the electronic states

Most conjugated polymers exhibit a twofold rotational symmetry about an axis passing through their centre and perpendicular to the plane of the nuclei [45]. Such polymers belong to the C_{2h} symmetry point group [58], whose character table is shown below (table 2.1). The C_{2h} symmetry point group contains the symmetry operations E, C_2, i, and σ_h, respectively denoting identity, rotation around a twofold axis, inversion through a centre of symmetry, and reflection through a horizontal plane. The wavefunctions may be labelled by establishing whether they are symmetric or antisymmetric with respect to rotation around the C_2 axis (a, b), and under inversion at the symmetry centre (g, u). In the case of π-electron states, the a_g and b_u representations can be discarded, since the p_z atomic orbitals are antisymmetric with respect to reflection in the mirror plane [58]. As can be seen in table 2.1, this leaves only the a_u and b_g possibilities.

The many-body wavefunctions describing the electronic states of conjugated polymers are built by populating π-electron levels in Slater determinants. Their overall symmetry can be derived from the a_u or b_g character of the occupied single-particle orbitals, with the help of the multiplication rules [58, 59]

$$\begin{aligned} &a \otimes a = b \otimes b = a, \\ &a \otimes b = b \otimes a = b, \\ &g \otimes g = u \otimes u = g, \\ &g \otimes u = u \otimes g = u. \end{aligned} \tag{2.1}$$

The above relationships imply that the many-body states with an even number of

Table 2.1: Character table of the C_{2h} symmetry point group [58].

C_{2h}	E	$C_2\,(z)$	i	σ_h	
a_g	1	1	1	1	R_z, x^2, y^2, z^2, $x\,y$
b_g	1	−1	1	−1	R_x, R_y, $x\,z$, $y\,z$
a_u	1	1	−1	−1	z
b_u	1	−1	−1	1	x, y

electrons have two possible symmetries, conventionally labelled using capital letters [45, 59]:

$$\begin{aligned} a_u \otimes a_u = b_g \otimes b_g = A_g, \\ a_u \otimes b_g = b_g \otimes a_u = B_u. \end{aligned} \tag{2.2}$$

As depicted in figure 2.4, in the ground state the lowest π-electron levels are all doubly occupied, which leads to an overall A_g character. Given that the symmetry of the single-particle orbitals alternates between a_u and b_g [45] (with a_u corresponding to the lowest energy level), an excitation from the highest occupied molecular orbital (HOMO) to the lowest unoccupied molecular orbital (LUMO) possesses B_u character. There are also two possible ways of producing an excitation with A_g symmetry: by promoting two electrons by an odd number of levels, or one electron by an even number of states [59] (see figure 2.4). If we neglect the effect of electron correlation, we may simply sum the single-particle contributions to obtain the energies of the many-body states. In this case, the ordering of the first singlet electronic states reads

$$1\,^1A_g < 1\,^1B_u < 2\,^1A_g. \tag{2.3}$$

However, electronic correlation has a drastic influence and, if sufficiently strong, can lead to the reversal of the lowest excited states [45, 59]:

$$1\,^1A_g < 2\,^1A_g < 1\,^1B_u. \tag{2.4}$$

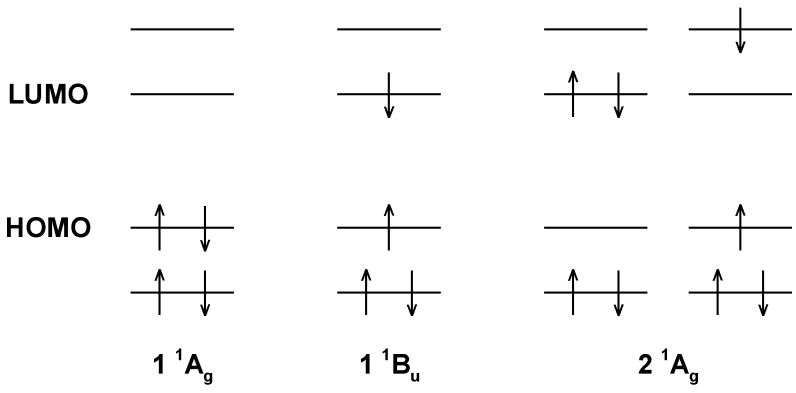

Figure 2.4: Symmetry of the first singlet electronic states in conjugated polymers.

This effect has been verified by two-photon spectroscopy experiments conducted for polyene oligomers [60]. The ordering of the excited states may be further influenced by such diverse factors as conformational disorder, chain ends, interchain interactions, and the presence of other chemical species in the molecule [59].

The relative energetic positioning of the first excited states is of utmost importance, since it is responsible for the optical properties of the system. The transition $1\,^1B_u \rightarrow 1\,^1A_g$ is dipole-allowed, whereas the transition $2\,^1A_g \rightarrow 1\,^1A_g$ is forbidden [45, 59]. Consequently, when the $1\,^1B_u$ state lies below the $2\,^1A_g$ state, the polymer is expected to luminesce strongly. Such is the case of phenyl-based systems, like poly(*para*-phenylene) and poly(*para*-phenylene vinylene). If the $1\,^1B_u$ state lies above the $2\,^1A_g$ state, then the compound is nonluminescent, as in the case of linear polyenes, such as polyacetylene and polydiacetylene.

2.3 Elementary excitations

One of the most distinctive features of conjugated compounds is the strong interdependence of the electronic and geometric structures. Introducing electrons or holes in the polymer chain through chemical doping, photoexcitation, or charge injection, leads to a drastic rearrangement of the π-electron bonding surrounding the charge. The emergence of solitons in *trans*-polyacetylene is a prime example of the important role of structural relaxation [44–46].

The ground state configuration of *trans*-polyacetylene is *degenerate*, since the

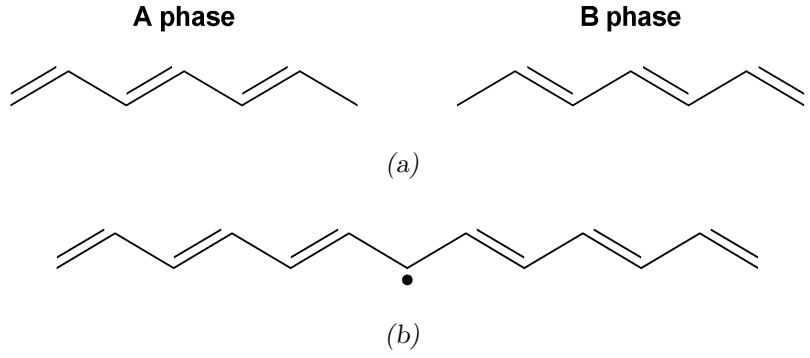

Figure 2.5: Degenerate ground state configurations (a), and the structure of a neutral soliton (b) in trans*-polyacetylene.*

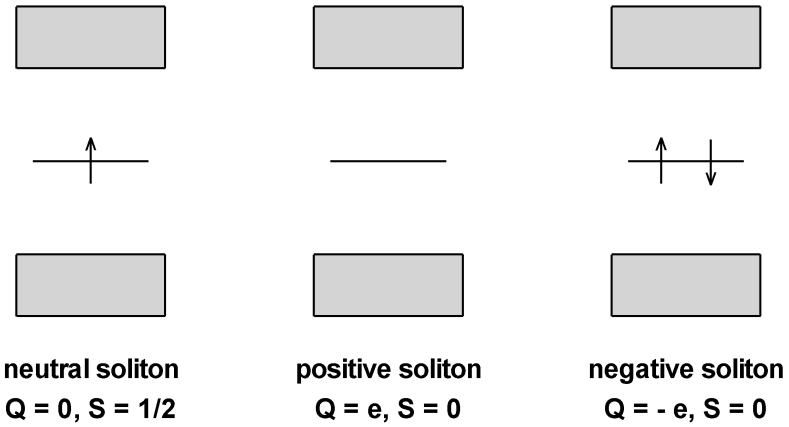

Figure 2.6: Different soliton excitations that arise depending on the occupancy of the associated midgap state. Notice how the spin-charge relation is reversed compared to electrons.

positions of the single and double bonds may be interchanged at no energy cost. There are two resonant chemical structures, known as the 'A' and 'B' phases [44–46], as illustrated in figure 2.5(a). An additional charge leads to the creation of a modified region in the chain, separating the two degenerate configurations. In order to ensure the tetravalency of the carbon atom at the defect, a dangling bond must form [see figure 2.5(b)]. This bond-defect is usually referred to as a *soliton* [44–46]. Whenever a soliton is present in degenerate ground state systems, an energy level appears in the middle of the π–π^* gap [44–46]. Depending on the occupation of the midgap state, solitons may be neutral, as well as positively and negatively charged, as shown in figure 2.6. In the case of the dangling bond, there is an electron and a positively charged ion occupying the same lattice site [46]. The electronic and ionic charges are balanced, which gives rise to a neutral excitation. However, since we are left with an unpaired electron in the associated midgap state, the neutral soliton has spin $\frac{1}{2}$. When there is no electron to balance the ion, the soliton becomes positively charged. Similarly, two electrons overbalance the ion and the soliton is negatively charged. In both cases, the resulting excitation is spinless, since all the states in the system are spin-paired (see figure 2.6). The spin-charge relation of solitons is thus reversed in comparison with that of electrons.

In contrast to *trans*-polyacetylene, most conjugated polymers favour a specific state of bond alternation and possess a *nondegenerate* ground state [45, 46]. An

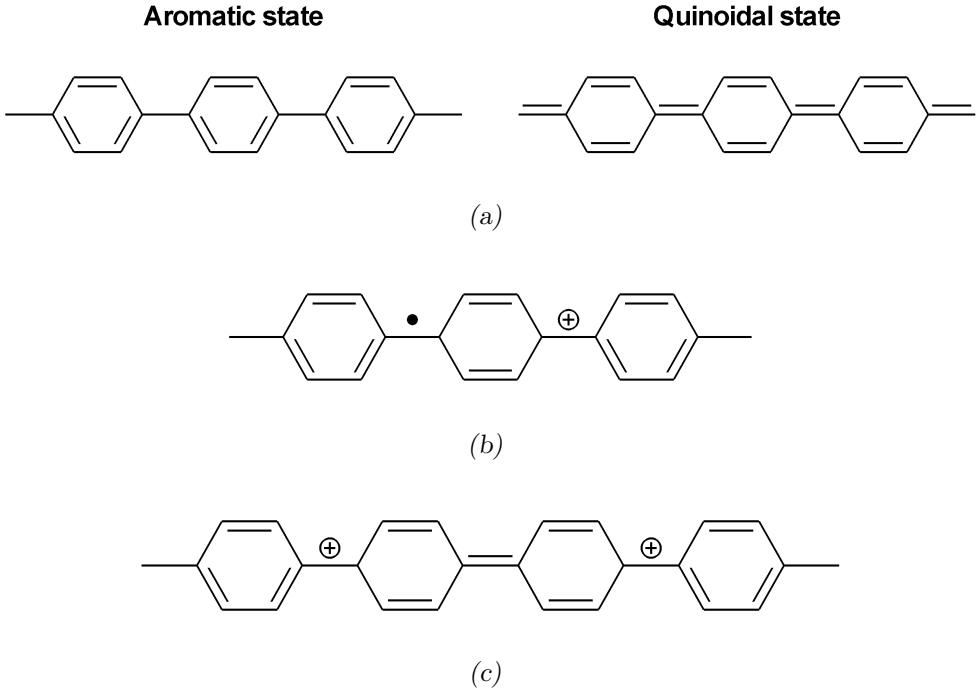

*Figure 2.7: Nondegenerate ground state configurations (a), and the structures of a positively charged polaron (b) and bipolaron (c) in poly(*para*-phenylene).*

example is poly(*para*-phenylene), whose possible ground state structures are depicted in figure 2.7(a). In this case, the aromatic configuration (with three double bonds in each ring) is more stable than the quinoidal structure [46] (with only two double bonds in each ring, but with the rings connected by double bonds rather than single bonds). For polymers with nondegenerate ground states, solitons are no longer stable excitations. Indeed, a soliton in such a system would be pushed to the chain end, turning high-energy regions into low-energy ones as it moved along [46]. Conjugational defects may be stabilised in these polymers by creating bound double-defects, which are generally termed *polarons* [44–46]. Figure 2.7(b) shows a polaron in poly(*para*-phenylene). This particular species is composed of a neutral and a positive soliton, which are driven towards one another by the lattice, so as to minimise the extent of the quinoidal region of the chain [46]. However, they are unable to recombine, because there is only one unpaired electron, which is insufficient to create a bond. Figure 2.7(c) illustrates a defect consisting of two positive solitons. This is usually referred to as a *bipolaron*, since when two polarons are brought together, the neutral solitons may produce a bond and only the two charged solitons

remain [44, 46].

The two confined midgap states associated with the soliton constituents of a polaron interact to produce two levels equidistant from the midgap [44–46]. Depending on the occupation of the gap states, several species with different character emerge. As shown in figure 2.8, polarons exhibit the usual spin-charge relationship, while bipolarons are charged but spinless. The two possibilities of populating each of the polaron levels with a single electron are analogous to the case of excitons in

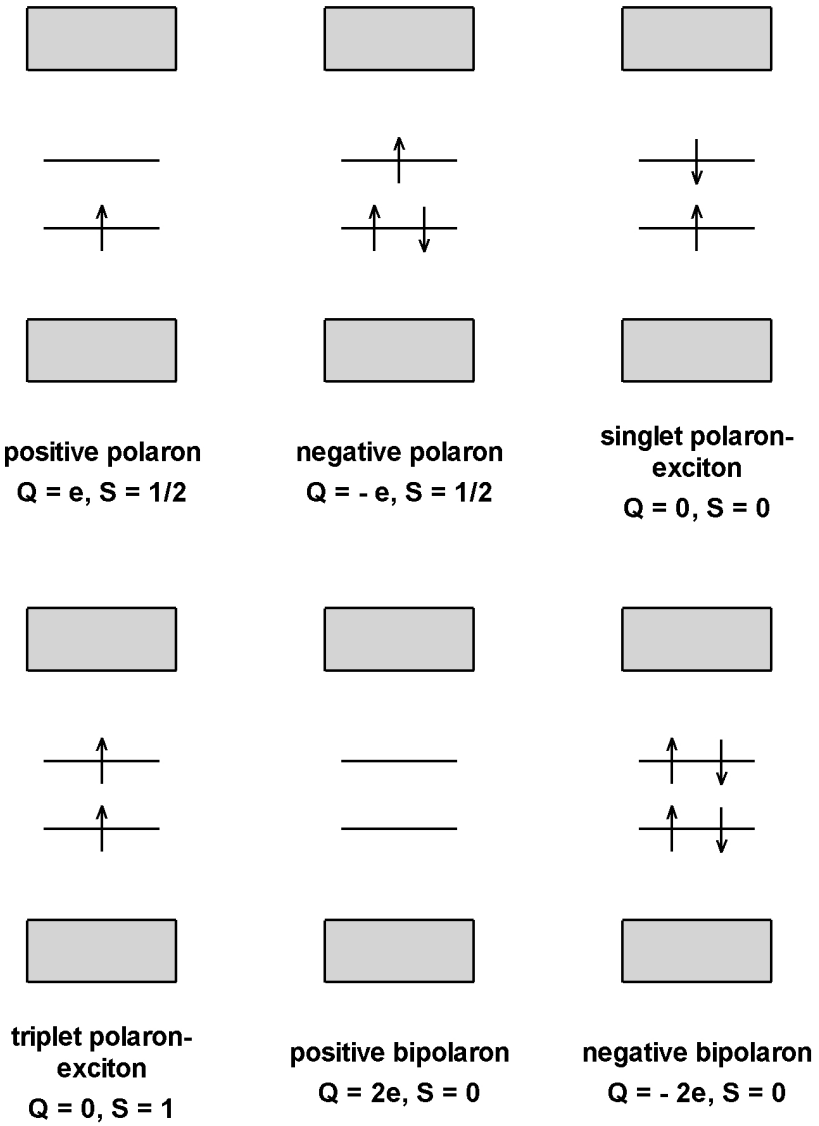

Figure 2.8: Different polaron and bipolaron excitations that arise depending on the occupancy of the associated gap states. The spin-charge relation of polarons is the usual one, while bipolarons are charged but spinless.

inorganic semiconductors. Hence, these defects are called *polaron-excitons* [45, 46]. Throughout this thesis, we will mostly refer to such excitations simply as 'excitons', while the term 'polaron' will be used for the charged species.

2.4 Photophysical properties

The photophysics of conjugated polymers exhibits a wealth of excitation and relaxation processes, which strongly depend on the electronic and structural properties [57, 61]. Absorption of a photon brings an isolated organic molecule into a phonon level of one of the excited singlet electronic states, of B_u character. Excitation into a phonon level of the lowest excited singlet state (if dipole-allowed) is followed by ultrafast *vibrational relaxation* into the phonon ground state, within a time scale of the order of 100 fs [62, 63]. Provided that the excitation energy is large enough, a higher lying singlet level may be initially excited. In this case, ultrafast *internal conversion* into the lowest excited singlet state occurs within about 50 fs [64], and this is followed by relaxation into the vibrational ground state. Depending on whether the $1\,^1B_u$ state lies below the $2\,^1A_g$ state, the molecule may decay into the electronic ground state *radiatively*. This process, known as *fluorescence*, usually takes place on a time scale in the range 0.1–1 ns [65]. Alternatively, the excitation may decay *nonradiatively*, most notably through fast vibrational relaxation channels, which compete efficiently with the radiative decay process and contribute to decreasing the luminescence efficiency [57, 61]. The lowest excited singlet state may be further deactivated through *intersystem crossing* to the triplet manifold. This process populates the lowest triplet state, which is usually long-lived. After a lifetime of up to 1 ms [65], the triplet level decays into the electronic ground state, mainly via nonradiative channels.

In polymeric systems consisting of several chains, the photophysics is further complicated by the prevalence of *intermolecular interactions*. A central question that has been much debated in the literature [38–43] is whether excitons or polaron pairs are the primary products of photoexcitation. The presence of the charged species is evidenced by photoconductivity measurements [38], but the time scale

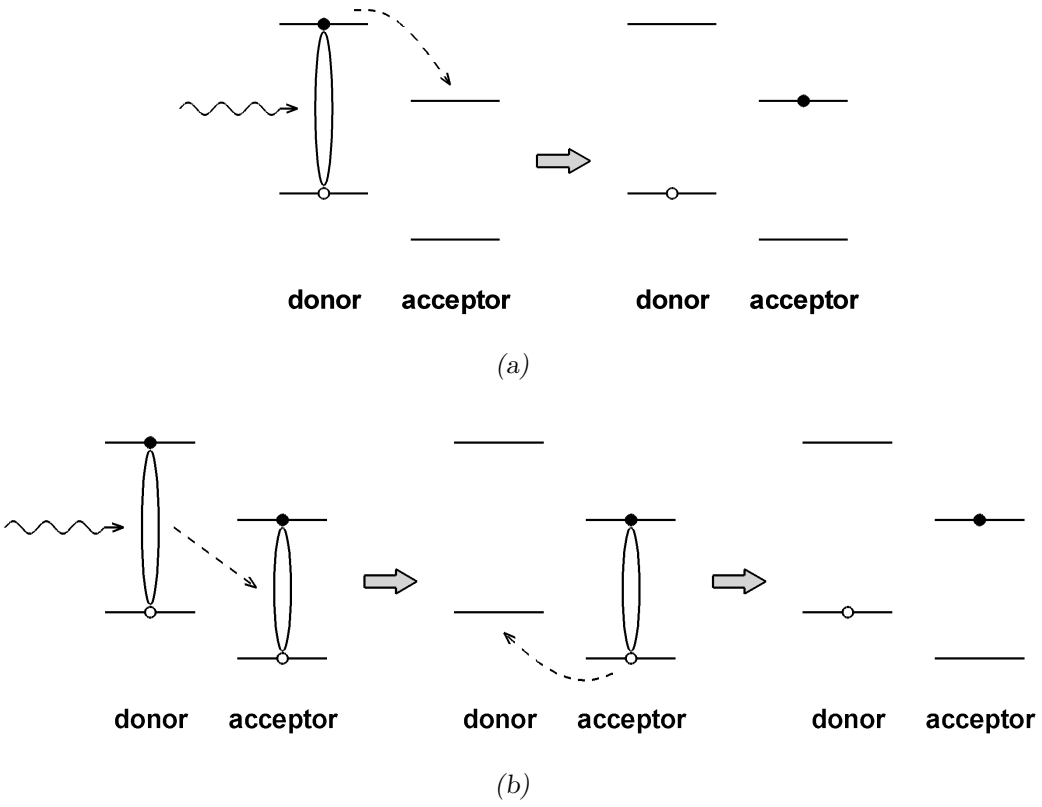

Figure 2.9: Possible charge generation mechanisms at donor/acceptor interfaces: (a) exciton dissociation through electron transfer to the acceptor, and (b) exciton hopping to the acceptor, followed by hole transfer to the donor. In both cases, the final state is the same.

and efficiency of charge carrier photogeneration are unclear. From the experimental viewpoint, this question appears to be settled, with considerable evidence [39–42] suggesting that, in general, both excitons and polaron pairs are created on ultrafast time scales, but the branching ratio of such products depends critically on the *strength of interchain interactions*. In dense conjugated polymer films, for which the interchain coupling is typically strong, the charge carrier photogeneration yield can approach about 25% [39, 42]. In the case of conjugated polymers in dilute solution (and also of films depending on the preparation conditions [40, 42]), where the interchain interactions are weak, this efficiency is considerably lower [41, 42] ($\lesssim 1\%$), and the formation of polaron pairs must rely almost exclusively on external *exciton dissociation* mechanisms, such as the field-induced splitting. On the theory front, however, there is still some inconsistency, with predictions presumably valid only for isolated chains being used to explain results observed for dense conjugated polymer

films [43]. Clarifying this issue is one of the main goals of the present thesis.

In addition to being dissociated into polaron pairs, excitons can move along and between chains, mainly via Förster-type dipole-dipole interactions [66]. In this process, known as *exciton migration* or *hopping*, the excitons navigate the density of states in a random walk fashion, losing energy at each step, until they find a suitable "trap", i.e., a low-energy site from which light emission may occur [66]. Depending on certain material properties, such as chain conformation and packing, exciton hopping can be a very efficient energy relaxation process, with time scales as low as 1 ps for dense conjugated polymer films [57, 61].

In a photovoltaic device built from a single conjugated polymer material, most photoexcitations decay via radiative or nonradiative recombination channels and do not contribute to the power conversion. One possibility of enhancing the charge carrier photogeneration yield is to combine the conjugated polymer with a suitable *electron acceptor* material. Prominent examples of such acceptors include fullerene and its derivatives [35, 36]. In polymer/fullerene composites, the excitons created in the donor phase (usually the polymer) can undergo dissociation after reaching the interface with the fullerene acceptor, by transferring an electron due to the favourable energy offset of the bands [see figure 2.9(a)]. The *photoinduced charge transfer* typically takes place within about 50 fs [67], a time scale much faster than that of alternative loss mechanisms. Thus, the charge transfer can be nearly complete. It has also been suggested [68] that the charge generation can occur in a *two-step* process, through exciton hopping to the fullerene and subsequent hole transfer to the polymer, as depicted in figure 2.9(b). The precise mechanism is not yet known [37], and it may be very much system-dependent. Understanding the charge transfer dynamics at donor/acceptor interfaces, as well as assessing which conditions lead to an optimised charge transfer process, are two major goals of this thesis.

Part II

Theoretical framework

Chapter 3

Semiempirical π-electron models

3.1 The Born-Oppenheimer approximation

In the nonrelativistic approximation, the many-body Hamiltonian describing a system of interacting electrons and nuclei can be written as

$$\hat{H} = \hat{H}_{\mathrm{n-n}}\left(\boldsymbol{R}\right) + \hat{H}_{\mathrm{e-e}}\left(\boldsymbol{r}\right) + \hat{H}_{\mathrm{e-n}}\left(\boldsymbol{r}, \boldsymbol{R}\right), \tag{3.1}$$

where the term

$$\hat{H}_{\mathrm{n-n}}\left(\boldsymbol{R}\right) = -\sum_{\alpha} \frac{\hbar^2}{2M_\alpha} \boldsymbol{\nabla}_\alpha^2 + \frac{1}{2} \sum_{\alpha,\beta\neq\alpha} \frac{Z_\alpha Z_\beta e^2}{\left|\boldsymbol{R}_\alpha - \boldsymbol{R}_\beta\right|} \tag{3.2}$$

includes the nuclear kinetic energy and the potential energy arising from repulsive Coulomb interactions between the nuclei,

$$\hat{H}_{\mathrm{e-e}}\left(\boldsymbol{r}\right) = -\sum_{i} \frac{\hbar^2}{2m_{\mathrm{e}}} \boldsymbol{\nabla}_i^2 + \frac{1}{2} \sum_{i,j\neq i} \frac{e^2}{\left|\boldsymbol{r}_i - \boldsymbol{r}_j\right|} \tag{3.3}$$

describes the electronic kinetic energy and the electron-electron Coulomb repulsion energy, and

$$\hat{H}_{\mathrm{e-n}}\left(\boldsymbol{r}, \boldsymbol{R}\right) = -\sum_{i,\alpha} \frac{Z_\alpha e^2}{\left|\boldsymbol{r}_i - \boldsymbol{R}_\alpha\right|} \tag{3.4}$$

represents the potential energy that results from the attractive electron-nuclear Coulomb interactions. $\boldsymbol{R} = \left\{\boldsymbol{R}_1, \boldsymbol{R}_2, \ldots\right\}$ and $\boldsymbol{r} = \left\{\boldsymbol{r}_1, \boldsymbol{r}_2, \ldots\right\}$ denote the set of nuclear and electronic coordinates, respectively, M_α and m_{e} are the nuclear and

electronic masses, Z_α denotes the atomic number of nucleus α, and e is the electronic charge.

Most physical problems of interest consist of a large number of interacting electrons and nuclei, and an exact solution of the many-body Hamiltonian is prohibitive. In order to reduce the complexity to a tractable level, it is essential to introduce suitable approximations. A widely used scheme, known as the *Born-Oppenheimer approximation*, exploits the great disparity between the masses of electrons and nuclei to decouple the electronic and nuclear degrees of freedom [45]. Since electrons are much lighter than the nuclei, they move faster and can rapidly adjust to changes in nuclear position. Therefore, it is reasonable to consider the electrons to be moving in the field of *fixed nuclei*.

Within the Born-Oppenheimer approximation, the many-body wavefunction is factorised into a product of electronic and nuclear contributions, which can be treated independently:

$$\Psi\left(\boldsymbol{r},\boldsymbol{R}\right) = \Psi_{\mathrm{e}}\left(\boldsymbol{r};\boldsymbol{R}\right)\,\Psi_{\mathrm{n}}\left(\boldsymbol{R}\right). \tag{3.5}$$

The electronic wavefunction, $\Psi_{\mathrm{e}}\left(\boldsymbol{r};\boldsymbol{R}\right)$, only depends *parametrically* on the nuclear coordinates, and is an eigenfunction of the *Born-Oppenheimer Hamiltonian* [45]:

$$\hat{H}_{\mathrm{BO}}\left(\boldsymbol{r};\boldsymbol{R}\right)\,\Psi_{\mathrm{e}}\left(\boldsymbol{r};\boldsymbol{R}\right) = E_{\mathrm{e}}\left(\boldsymbol{R}\right)\,\Psi_{\mathrm{e}}\left(\boldsymbol{r};\boldsymbol{R}\right), \tag{3.6}$$

with

$$\hat{H}_{\mathrm{BO}}\left(\boldsymbol{r};\boldsymbol{R}\right) = \hat{H}_{\mathrm{e-e}}\left(\boldsymbol{r}\right) + \hat{H}_{\mathrm{e-n}}\left(\boldsymbol{r};\boldsymbol{R}\right) + \frac{1}{2}\sum_{\alpha,\beta\neq\alpha}\frac{Z_\alpha Z_\beta\, e^2}{\left|\boldsymbol{R}_\alpha - \boldsymbol{R}_\beta\right|}. \tag{3.7}$$

The corresponding eigenvalue, $E_{\mathrm{e}}\left(\boldsymbol{R}\right)$, is known as the *adiabatic potential energy surface*. In the second quantisation formalism, the Born-Oppenheimer Hamiltonian takes the form [45]

$$\hat{H}_{\mathrm{BO}} = \sum_{i,j,\sigma} T_{ij}\,\hat{c}^\dagger_{i\sigma}\,\hat{c}_{j\sigma} + \frac{1}{2}\sum_{\substack{i,j,k,l\\ \sigma,\sigma'}} V_{ijkl}\,\hat{c}^\dagger_{i\sigma}\,\hat{c}^\dagger_{j\sigma'}\,\hat{c}_{l\sigma'}\,\hat{c}_{k\sigma} + \frac{1}{2}\sum_{\alpha,\beta\neq\alpha}\frac{Z_\alpha Z_\beta\, e^2}{\left|\boldsymbol{R}_\alpha - \boldsymbol{R}_\beta\right|}, \tag{3.8}$$

where $\hat{c}^\dagger_{i\sigma}$ ($\hat{c}_{i\sigma}$) creates (annihilates) an electron with spin σ in the spin-orbital

$\chi_i(\boldsymbol{r},\sigma)$, and the one- and two-electron integrals, T_{ij} and V_{ijkl}, are defined as

$$\begin{aligned} T_{ij} &= \int \chi_i^*(\boldsymbol{r}) \left[-\frac{\hbar^2}{2m_\mathrm{e}} \boldsymbol{\nabla}^2 - \sum_\alpha \frac{Z_\alpha e^2}{|\boldsymbol{r}-\boldsymbol{R}_\alpha|} \right] \chi_j(\boldsymbol{r})\, \mathrm{d}\boldsymbol{r}, \\ V_{ijkl} &= \int \chi_i^*(\boldsymbol{r})\, \chi_j^*(\boldsymbol{r}')\, \frac{e^2}{|\boldsymbol{r}-\boldsymbol{r}'|}\, \chi_k(\boldsymbol{r})\, \chi_l(\boldsymbol{r}')\, \mathrm{d}\boldsymbol{r}\, \mathrm{d}\boldsymbol{r}'. \end{aligned} \tag{3.9}$$

3.2 The π-electron approximation

The Born-Oppenheimer Hamiltonian describes *all* the electronic degrees of freedom, and remains very difficult to solve. Further approximations leading to a *model reduction* are thus desirable. In conjugated polymers, the separation of the energy scales of σ and π electronic processes can be exploited to build such simplified models [45]. The idea is to consider *explicitly* only the π-electrons, one per CH group or *site*, while acknowledging that the σ and core electrons have the effect of *screening* the Coulomb interactions between the remaining degrees of freedom. This is accomplished through the *truncation of the basis set* and the introduction of *effective interaction potentials* [45]. The Born-Oppenheimer Hamiltonian for the π-electrons can be expressed as

$$\hat{H}^\pi_\mathrm{BO} = \sum_{i,j,\sigma} \widetilde{T}_{ij}\, \hat{c}^\dagger_{i\sigma}\, \hat{c}_{j\sigma} + \frac{1}{2} \sum_{\substack{i,j,k,l \\ \sigma,\sigma'}} \widetilde{V}_{ijkl}\, \hat{c}^\dagger_{i\sigma}\, \hat{c}^\dagger_{j\sigma'}\, \hat{c}_{l\sigma'}\, \hat{c}_{k\sigma} + V^\mathrm{eff}_\mathrm{n-n}\left(\boldsymbol{R}\right). \tag{3.10}$$

The various terms in the above equation acquire a new meaning. $V^\mathrm{eff}_\mathrm{n-n}\left(\boldsymbol{R}\right)$ is the screened nuclear-nuclear interaction potential, and $\hat{c}^\dagger_{i\sigma}$ ($\hat{c}_{i\sigma}$) now creates (annihilates) a π-electron with spin σ at site i. Equivalently, the basis functions, $\chi_i(\boldsymbol{r},\sigma)$, are restricted to the set of orthonormalised p_z atomic orbitals, centred on different sites. The one- and two-electron integrals are now given by

$$\begin{aligned} \widetilde{T}_{ij} &= \int \chi_i^*(\boldsymbol{r}) \left[-\frac{\hbar^2}{2m_\mathrm{e}} \boldsymbol{\nabla}^2 + V^\mathrm{eff}_\mathrm{e-n}\left(\boldsymbol{r};\boldsymbol{R}\right) \right] \chi_j(\boldsymbol{r})\, \mathrm{d}\boldsymbol{r}, \\ \widetilde{V}_{ijkl} &= \int \chi_i^*(\boldsymbol{r})\, \chi_j^*(\boldsymbol{r}')\, V^\mathrm{eff}_\mathrm{e-e}(\boldsymbol{r}-\boldsymbol{r}')\, \chi_k(\boldsymbol{r})\, \chi_l(\boldsymbol{r}')\, \mathrm{d}\boldsymbol{r}\, \mathrm{d}\boldsymbol{r}', \end{aligned} \tag{3.11}$$

where $V^\mathrm{eff}_\mathrm{e-n}\left(\boldsymbol{r};\boldsymbol{R}\right)$ models the effective interaction between the π-electrons and the nuclei, and $V^\mathrm{eff}_\mathrm{e-e}(\boldsymbol{r}-\boldsymbol{r}')$ denotes the effective electron-electron interaction potential.

3.3 Fixed nuclei models

In principle, the effective potentials required in equation (3.10) could be derived *ab initio*, but, in practice, *semiempirical parameters*, obtained by fitting the predictions of model Hamiltonians to known experimental data, are used instead [45]. Depending on the terms that are kept in equation (3.10), several semiempirical models can be devised. The simplest approximation is to assume that the one-electron integrals are only nonzero for electrons in neighbouring orbitals, and to neglect the electron-electron interactions and the constant $V_{\mathrm{n-n}}^{\mathrm{eff}}\left(\boldsymbol{R}\right)$ term. This leads to the *Hückel model* [69, 70]:

$$\hat{H}_{\mathrm{H}} = -\sum_{i,\sigma} t_i \left(\hat{c}_{i\sigma}^{\dagger}\, \hat{c}_{i+1,\sigma} + \hat{c}_{i+1,\sigma}^{\dagger}\, \hat{c}_{i\sigma}\right). \tag{3.12}$$

The nearest-neighbour *transfer* (or *hopping*) integral, $t_i \equiv -\widetilde{T}_{i,i+1}$, is defined as

$$t_i = t_0\,(1 - \delta_i), \tag{3.13}$$

where t_0 denotes the hopping integral for the undistorted structure, and δ_i is the relative change of the i-th bond length from its average value, or *dimerisation*. Positive and negative values of δ_i correspond to single and double bonds, respectively.

Despite its simplified assumptions, the Hückel model is sufficiently robust to predict trends in energy and spectroscopic properties of conjugated compounds [71, 72]. It is also particularly appealing, since it can be solved analytically in some simple cases. For an infinite chain of equally spaced CH groups, i.e., when $\delta_i = 0$, the expectation values of the Hamiltonian are given by [45]

$$\varepsilon_\kappa = -2\,t_0 \cos\kappa, \tag{3.14}$$

where κ is a dimensionless wavevector. Figure 3.1(a) shows this energy dispersion relation for the first Brillouin zone, which lies in the range $-\pi < \kappa < \pi$. As can be seen, a single band, of width $W = 4\,t_0$, is obtained. There is no energy gap and, in the half-filled case, the electronic band structure is that of a one-dimensional metal. However, such a configuration is unstable with respect to a lattice distortion which brings every other CH group towards one of its neighbours and further away

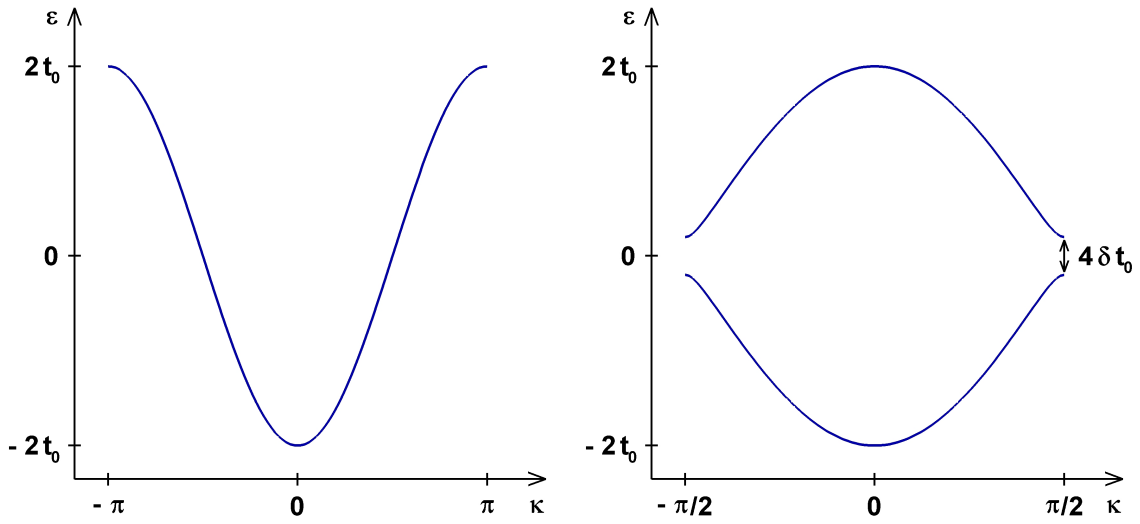

(a) *(b)*

Figure 3.1: Electronic energy dispersion curves for an infinite Hückel chain, in the undimerised (a) and perfectly dimerised (b) cases.

from the other, a result known as *Peierls theorem* [73]. Indeed, for a perfectly dimerised infinite chain, such that $\delta_i = (-1)^i \, \delta$, the expectation values of the Hückel Hamiltonian read [45]

$$\varepsilon_\kappa = \pm 2 \, t_0 \sqrt{\cos^2 \kappa + \delta^2 \sin^2 \kappa}. \tag{3.15}$$

As depicted in figure 3.1(b), two bands are formed, separated by an energy gap of magnitude $E_\mathrm{g} = 4 \, \delta \, t_0$. Notice that the first Brillouin zone is restricted to the range $-\frac{\pi}{2} < \kappa < \frac{\pi}{2}$, as a consequence of doubling the size of the unit cell. The energy of the occupied electronic states is lowered in comparison with the undimerised case, and the system is a semiconductor instead of a metal.

In order to increase the level of accuracy and predictive power of theoretical models, it is crucial to consider the effect of Coulomb interactions [45]. The most general approximation requires adding long-range potentials, which is typically accomplished by setting

$$V_{\mathrm{n-n}}^{\mathrm{eff}} \left(\boldsymbol{R} \right) = \frac{NU}{4} + \frac{1}{2} \sum_{i,j \neq i} v_{ij}, \tag{3.16}$$

$$\widetilde{T}_{ij} = -\begin{cases} U/2 + \sum_{k\neq i} v_{ik} & \text{if } i = j \\ t_i & \text{if } i = j-1 \\ t_{i-1} & \text{if } i = j+1 \\ 0 & \text{otherwise} \end{cases}, \tag{3.17}$$

and

$$\widetilde{V}_{ijkl} = \begin{cases} v_{ij} & \text{if } i = k \text{ and } j = l \\ 0 & \text{otherwise} \end{cases}. \tag{3.18}$$

This choice leads to the *Pariser-Parr-Pople* (PPP) *model* [74–76]:

$$\begin{aligned} \hat{H}_{\text{PPP}} = &- \sum_{i,\sigma} t_i \left(\hat{c}^\dagger_{i\sigma}\, \hat{c}_{i+1,\sigma} + \hat{c}^\dagger_{i+1,\sigma}\, \hat{c}_{i\sigma}\right) + U \sum_i \left(\hat{n}_{i\uparrow} - \frac{1}{2}\right)\left(\hat{n}_{i\downarrow} - \frac{1}{2}\right) + \\ &+ \frac{1}{2} \sum_{i,j\neq i} v_{ij} \left(\hat{n}_i - 1\right)\left(\hat{n}_j - 1\right), \end{aligned} \tag{3.19}$$

with

$$\hat{n}_i = \sum_\sigma \hat{n}_{i\sigma} = \sum_\sigma \hat{c}^\dagger_{i\sigma}\, \hat{c}_{i\sigma}. \tag{3.20}$$

In the above equations, N is the number of CH groups in the chain, U denotes the screened onsite Coulomb repulsion energy, and v_{ij} is a suitable semiempirical potential. Throughout this thesis, we will use the *Ohno potential*, defined as [77]

$$v_{ij} = \frac{U}{\sqrt{1 + (\beta\, r_{ij}/r_0)^2}}, \tag{3.21}$$

where r_{ij} denotes the distance between sites i and j, r_0 is the average bond length, and β, the ratio between the onsite and intersite repulsion energies, determines the length scale in which v_{ij} falls to a Coulomb potential, e^2/r_{ij}.

The PPP model has been used extensively to calculate the electronic structure and spectroscopic properties of conjugated polymers, and established the decisive role played by electronic correlations in determining the properties of these materials [78–81]. Notable results include the prediction of the reverse ordering of $2\,^1A_g$ and $1\,^1B_u$ excited states in linear polyenes [78], which explains why not all conjugated polymers luminesce, and the reproduction of multiple absorption features in the optical spectra of phenyl-based polymers [80, 81].

3.4 Dynamical nuclei models

A more realistic description of the low-energy physics of conjugated polymers requires models that go beyond the Born-Oppenheimer approximation, by considering *dynamical nuclei* explicitly coupled to the π-electrons [45]. In the simplest approximation, the effective electron-nuclear interaction potential is expanded to first order around some *reference* set of coordinates, usually taken as the undimerised configuration. This procedure yields [45]

$$\hat{H}^{\pi}_{\mathrm{e-n}} = \alpha \sum_{i,\sigma} (u_{i+1} - u_i) \left(\hat{c}^{\dagger}_{i\sigma}\, \hat{c}_{i+1,\sigma} + \hat{c}^{\dagger}_{i+1,\sigma}\, \hat{c}_{i\sigma} \right), \tag{3.22}$$

where α denotes the *electron-phonon coupling* constant, and u_i is the displacement of site i from its equidistant position, projected onto the chain axis. The lattice is modelled by a simple harmonic Hamiltonian [45]:

$$\hat{H}_{\mathrm{n-n}} = \frac{1}{2M} \sum_i p_i^2 + \frac{K}{2} \sum_i (u_{i+1} - u_i)^2. \tag{3.23}$$

The second term in the above equation represents the potential energy associated with small displacements from the undistorted structure, which is determined by the σ-bonds alone. Thus, K is the elastic constant due to the σ-bonds, while M denotes the mass of a CH unit, and p_i the nuclear momenta.

Adding the contributions (3.22) and (3.23) to the Hückel and PPP Hamiltonians, respectively leads to the *Su-Schrieffer-Heeger* (SSH) *model* [82, 83],

$$\hat{H}_{\mathrm{SSH}} = -\sum_{i,\sigma} t_i \left(\hat{c}^{\dagger}_{i\sigma}\, \hat{c}_{i+1,\sigma} + \hat{c}^{\dagger}_{i+1,\sigma}\, \hat{c}_{i\sigma} \right) + \frac{1}{2M} \sum_i p_i^2 + \frac{K}{2} \sum_i (u_{i+1} - u_i)^2, \tag{3.24}$$

and to its extension to include long-range Coulomb interactions,

$$\begin{aligned} \hat{H}_{\mathrm{SSH+PPP}} = &-\sum_{i,\sigma} t_i \left(\hat{c}^{\dagger}_{i\sigma}\, \hat{c}_{i+1,\sigma} + \hat{c}^{\dagger}_{i+1,\sigma}\, \hat{c}_{i\sigma} \right) + U \sum_i \left(\hat{n}_{i\uparrow} - \frac{1}{2} \right) \left(\hat{n}_{i\downarrow} - \frac{1}{2} \right) + \\ &+ \frac{1}{2} \sum_{i,j \neq i} v_{ij} (\hat{n}_i - 1)(\hat{n}_j - 1) + \frac{1}{2M} \sum_i p_i^2 + \frac{K}{2} \sum_i (u_{i+1} - u_i)^2, \end{aligned} \tag{3.25}$$

which we refer to as the *SSH + PPP model*. The nearest-neighbour transfer integral is now given by

$$t_i = t_0 - \alpha\, (u_{i+1} - u_i), \tag{3.26}$$

which is appropriate for the special case of *trans*-polyacetylene, since the dimerisation is caused *entirely* by the π-electron coupling to the lattice [45]. With the above definition, the static ground state energy per site of a perfectly dimerised SSH chain, for which $u_i = (-1)^i\, u$, reads [45]

$$E_0\,(u) = -\frac{4\,t_0}{\pi}\,E\left(1 - \left(\frac{2\,\alpha\,u}{t_0}\right)^2\right) + 2\,K u^2, \tag{3.27}$$

where

$$E\left(x = k^2\right) = \int_0^{\pi/2} \sqrt{1 - k^2 \sin^2\theta}\;\mathrm{d}\theta \tag{3.28}$$

is the complete elliptic integral of the second kind. As shown in figure 3.2(a), the adiabatic potential $E_0\,(u)$ exhibits two equivalent minima at $\pm\,u_0$ (corresponding to the A and B phases), separated by a local maximum at $u = 0$, which is consistent with the Peierls theorem.

In most other conjugated polymers, *extrinsic* factors, such as the σ-bonding structure (as in the case of *cis*-polyacetylene) or the presence of phenyl rings, also contribute to the dimerisation. This effect is often modelled by adding an *extrinsic transfer* term, $(-1)^{i+1}\,t_\mathrm{e}$, to the hopping integral [84, 85]:

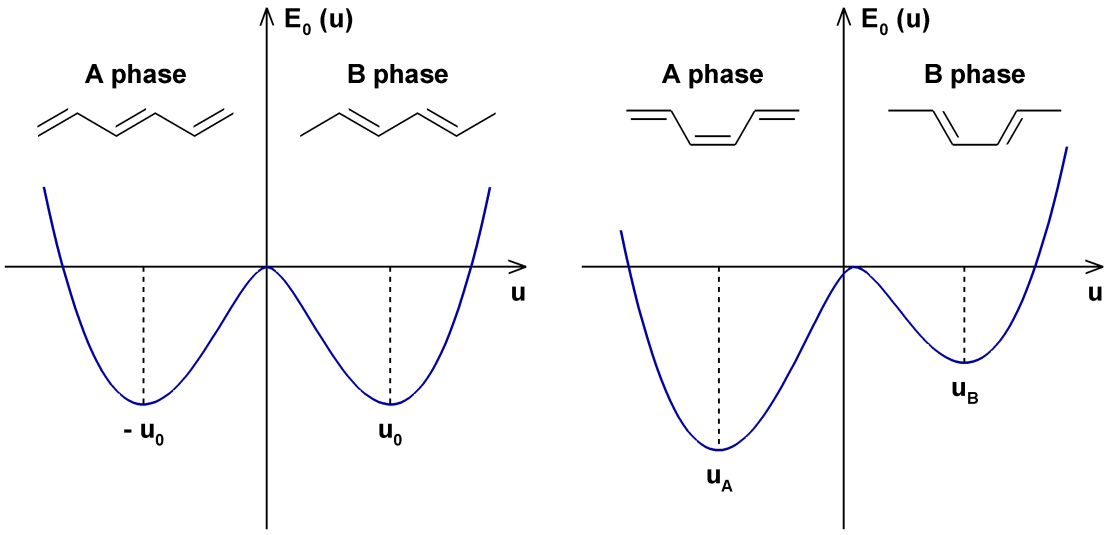

(a) *(b)*

Figure 3.2: Schematic representations of the ground state energy per site of a perfectly dimerised SSH chain, considering a nearest-neighbour transfer integral with only intrinsic (a) and with added extrinsic (b) terms.

$$t_i = t_0 - \alpha\,(u_{i+1} - u_i) + (-1)^{i+1}\,t_\mathrm{e}. \tag{3.29}$$

It is this term that causes the ground state degeneracy to be lifted. Indeed, assuming a perfectly dimerised ground state, the SSH energy per site in the static limit is changed slightly to [84, 86]

$$E_0\,(u) = -\frac{4\,t_0}{\pi}\,E\left(1 - \left(\frac{2\,\alpha\,u - t_\mathrm{e}}{t_0}\right)^2\right) + 2\,K u^2. \tag{3.30}$$

As depicted in figure 3.2(b), the minimum energy configurations are no longer equivalent, with the *cis-transoid* configuration (A phase) being the most stable one.

The SSH model has been widely used to study the formation and dynamical properties of photoexcitations [43, 47–50], and to describe charge transport and mobility [87, 88] in conjugated polymers. Despite lacking electron-electron interactions, it has contributed decisively to the current understanding of many dynamical processes inherent to these systems. In chapter 6, we will employ both the SSH and SSH + PPP models to study the dynamics of photoexcitations in *cis*-polyacetylene chains, with the goal of assessing the importance of Coulomb interactions.

3.5 Models with interchain interactions

To achieve a complete picture of the physics of conjugated polymers, especially in the dense form, it is necessary to further include *interchain interactions*. A simple way is to consider a system of two parallel chains, labelled by $q = 1, 2$, with the parameterisation

$$V_\mathrm{n-n}^\mathrm{eff}\left(\boldsymbol{R}\right) = (N_1 + N_2)\,\frac{U}{4} + \frac{1}{2}\sum_{q,q',i_q,j_{q'}}{}' v_{i_q j_{q'}}, \tag{3.31}$$

$$\widetilde{T}_{i_q j_{q'}} = -\begin{cases} U/\,2 + \sum\limits_{q'',k_{q''}}{}' v_{i_q k_{q''}} & \text{if } i_q = j_{q'} \text{ and } q = q' \\ t_{i_q} & \text{if } i_q = j_{q'} - 1 \text{ and } q = q' \\ t_{i_q - 1} & \text{if } i_q = j_{q'} + 1 \text{ and } q = q' \\ t_\perp & \text{if } i_q = j_{q'} + \frac{N_q - N_{q'}}{2} \text{ and } q \neq q' \\ 0 & \text{otherwise} \end{cases}, \tag{3.32}$$

and

$$\widetilde{V}_{i_q j_{q'} k_{q''} l_{q'''}} = \begin{cases} v_{i_q j_{q'}} & \text{if } i_q = k_{q''},\ q = q'',\ j_{q'} = l_{q'''},\ \text{and } q' = q''' \\ 0 & \text{otherwise} \end{cases}. \tag{3.33}$$

Together with equations (3.22) and (3.23) written for each chain, this choice yields the following *coupled-chain model*:

$$\begin{aligned} \hat{H}_{\mathrm{CC}} = & -\sum_{q,i_q,\sigma} t_{i_q} \left(\hat{c}^{\dagger}_{i_q\sigma}\,\hat{c}_{i_q+1,\sigma} + \hat{c}^{\dagger}_{i_q+1,\sigma}\,\hat{c}_{i_q\sigma}\right) - t_{\perp} \sum_{\langle i_1,i_2\rangle,\sigma} \left(\hat{c}^{\dagger}_{i_1\sigma}\,\hat{c}_{i_2\sigma} + \hat{c}^{\dagger}_{i_2\sigma}\,\hat{c}_{i_1\sigma}\right) + \\ & + U \sum_{q,i_q} \left(\hat{n}_{i_q\uparrow} - \frac{1}{2}\right)\left(\hat{n}_{i_q\downarrow} - \frac{1}{2}\right) + \frac{1}{2} {\sum_{q,q',i_q,j_{q'}}}' v_{i_q j_{q'}} (\hat{n}_{i_q} - 1)(\hat{n}_{j_{q'}} - 1) + \\ & + \frac{1}{2M} \sum_{q,i_q} p^2_{i_q} + \frac{K}{2} \sum_{q,i_q} (u_{i_q+1} - u_{i_q})^2. \end{aligned} \tag{3.34}$$

In the above expressions, the symbol $\sum'$ is used to indicate that the onsite terms $v_{i_q i_q}$ are excluded from the summation, $\sum_{\langle i_1,i_2\rangle}$ means that the sum is restricted to pairs of neighbouring sites in the opposite strands (i.e., sites facing each other), and $t_\perp$ denotes the *interchain* hopping integral. Throughout this thesis, we will assume that this quantity decreases exponentially with the interchain distance, d, according to

$$t_{\perp} = \frac{t_0}{10} \exp\left(1 - \frac{d}{5}\right), \tag{3.35}$$

where d is expressed in angstroms. The *intrachain* hopping integral, t_{i_q}, and the Ohno potential, $v_{i_q j_{q'}}$, are of the same form as in the previous sections. Also, notice that, within this model, the nuclei are constrained to move only along the chains.

By introducing suitable *onsite energies*, ϵ_{i_q}, and assuming *chain-dependent parameters*, a heterojunction between two different materials, or *donor/acceptor interface*, may be modelled:

$$\begin{aligned} \hat{H}_{\mathrm{D/A}} = & -\sum_{q,i_q,\sigma} t_{i_q} \left(\hat{c}^{\dagger}_{i_q\sigma}\,\hat{c}_{i_q+1,\sigma} + \hat{c}^{\dagger}_{i_q+1,\sigma}\,\hat{c}_{i_q\sigma}\right) - t_{\perp} \sum_{\langle i_1,i_2\rangle,\sigma} \left(\hat{c}^{\dagger}_{i_1\sigma}\,\hat{c}_{i_2\sigma} + \hat{c}^{\dagger}_{i_2\sigma}\,\hat{c}_{i_1\sigma}\right) + \\ & + \sum_{q,i_q} U_q \left(\hat{n}_{i_q\uparrow} - \frac{1}{2}\right)\left(\hat{n}_{i_q\downarrow} - \frac{1}{2}\right) + \frac{1}{2} {\sum_{q,q',i_q,j_{q'}}}' v_{i_q j_{q'}} (\hat{n}_{i_q} - 1)(\hat{n}_{j_{q'}} - 1) + \\ & + \sum_{q,i_q} \epsilon_{i_q}\,\hat{n}_{i_q} + \sum_{q,i_q} \frac{p^2_{i_q}}{2M_q} + \sum_{q,i_q} \frac{K_q}{2} (u_{i_q+1} - u_{i_q})^2. \end{aligned} \tag{3.36}$$

Instead of defining a new set of parameters to calculate the interchain quantities $t_\perp$ and $v_{i_q j_{q'}}$ (with $q \neq q'$), it is convenient to use arithmetic averages of the donor and acceptor parameters where appropriate. In this spirit, the interchain transfer integral is now given by

$$t_\perp = \frac{\bar{t}_0}{10} \exp\left(1 - \frac{d}{5}\right), \tag{3.37}$$

and the Ohno potential takes the generalised form

$$v_{i_q j_{q'}} = \frac{\bar{U}_{qq'}}{\sqrt{1 + \left(\bar{\beta}_{qq'}\, r_{i_q j_{q'}} / \bar{r}_{0_{qq'}}\right)^2}}, \tag{3.38}$$

with

$$\begin{aligned} \bar{U}_{qq'} &= \frac{U_q + U_{q'}}{2}, \\ \bar{\beta}_{qq'} &= \frac{\beta_q + \beta_{q'}}{2}, \\ \bar{r}_{0_{qq'}} &= \frac{r_{0_q} + r_{0_{q'}}}{2}. \end{aligned} \tag{3.39}$$

We will use the model Hamiltonians (3.34) and (3.36) in chapters 7 and 8, respectively, to study the effects of interchain interactions on the dynamics of photoexcitations in coupled *cis*-polyacetylene chains, as well as charge transfer dynamics at donor/acceptor interfaces.

Chapter 4

Approximate solution of the time-independent Schrödinger equation

4.1 Geometry optimisation

A dynamic simulation of a system of interacting electrons and nuclei requires the knowledge of its equilibrium configuration as a starting condition. To find the initial state, Ψ, along with its energy, E, it is necessary to solve the *time-independent* Schrödinger equation,

$$\hat{H}\,|\Psi\rangle = E\,|\Psi\rangle. \tag{4.1}$$

In principle, $\hat{H}$ is the many-body Hamiltonian (3.1), but often a simplified form is used instead, as discussed in the previous chapter. In any case, most physical problems of interest consist of a large number of interacting electrons and nuclei, and the resulting Schrödinger equation is very difficult to solve exactly, due to the multidimensional nature of the problem. A standard technique used to obtain an approximate solution relies on the *Rayleigh-Ritz variational principle* [89, 90], which states that the stationary points of the *energy functional*,

$$E\left[\Psi\right] = \langle\Psi|\,\hat{H}\,|\Psi\rangle, \tag{4.2}$$

correspond to the eigenstates of the Hamiltonian. The original eigenvalue problem is thus equivalent to a *variational optimisation*. In particular, when looking for the ground state, one needs to find the *global minimum* of the energy functional.

As discussed in the previous chapter, the problem is immensely simplified by using the Born-Oppenheimer approximation [89, 90]. Since the nuclei are much heavier than electrons, we can treat them as *classical* particles, and consider them as fixed for the purpose of calculating the electronic properties. The nuclear and electronic degrees of freedom are thus decoupled, and the problem is reduced to minimising the adiabatic potential energy surface [89, 90],

$$E_{\mathrm{BO}}\left(\boldsymbol{R}\right) = E_{\mathrm{e}}\left(\boldsymbol{R}\right) + V_{\mathrm{n}}\left(\boldsymbol{R}\right), \tag{4.3}$$

where $V_{\mathrm{n}}\left(\boldsymbol{R}\right)$ denotes the nuclear repulsion energy, and $E_{\mathrm{e}}\left(\boldsymbol{R}\right)$ is a solution of the electronic Schrödinger equation,

$$\hat{H}_{\mathrm{e}}\,|\Psi_{\mathrm{e}}\rangle = E_{\mathrm{e}}\,|\Psi_{\mathrm{e}}\rangle, \tag{4.4}$$

for a given arrangement of the nuclei. The electronic part of the many-body Hamiltonian, $\hat{H}_{\mathrm{e}}$, and the electronic wavefunction, Ψ_{e}, only depend parametrically on the nuclear coordinates, $\boldsymbol{R}$, and hence equation (4.4) is a *purely electronic* problem.

The process of finding the minimum of the adiabatic potential energy surface is called *geometry optimisation* [90]. For the π-electron models devised in the previous chapter, the gradient of the energy with respect to the nuclear coordinates can be written analytically and is typically well-behaved. In such cases, the *Broyden-Fletcher-Goldfarb-Shanno* (BFGS) algorithm [91] offers a robust and efficient way to perform the energy minimisation. In this method, an initial guess for the geometry (which, for conjugated polymers, may be taken as the undimerised configuration) is iteratively improved, until the energy gradient becomes zero within a specified tolerance. At each step of the iteration, it is necessary to solve the electronic subproblem (4.4). If the electronic part of the Hamiltonian only contains *one-body* operators, as in the case of the SSH model, the solution is given efficiently by the diagonalisation of the matrix representation of $\hat{H}_{\mathrm{e}}$ in a suitable basis set. However, when *two-body* operators are present, as in the case of the SSH + PPP model,

further approximations are required. In the following sections, we will show how the Rayleigh-Ritz variational principle can be used to obtain an approximate solution to the electronic Schrödinger equation in such cases. We will focus solely on the electronic subproblem, and the subscript 'e' will be omitted to simplify the notation.

4.2 The Hartree-Fock approximation

4.2.1 Spin-restricted formalism for closed-shell singlet states

Consider a system of N interacting electrons, described by the spin-independent Hamiltonian [92]

$$\hat{H} = \sum_{i,j,\sigma} T_{ij}\, \hat{c}^{\dagger}_{i\sigma}\, \hat{c}_{j\sigma} + \frac{1}{2} \sum_{\substack{i,j,k,l \\ \sigma,\sigma'}} V_{ijkl}\, \hat{c}^{\dagger}_{i\sigma}\, \hat{c}^{\dagger}_{j\sigma'}\, \hat{c}_{l\sigma'}\, \hat{c}_{k\sigma}, \tag{4.5}$$

where $\hat{c}^{\dagger}_{i\sigma}$ ($\hat{c}_{i\sigma}$) creates (annihilates) an electron with spin σ in the molecular spin-orbital $\phi_i(\boldsymbol{r}, \sigma)$, and

$$\begin{aligned} T_{ij} &= \int \phi_i^*(\boldsymbol{r})\, \hat{T}(\boldsymbol{r})\, \phi_j(\boldsymbol{r})\, \mathrm{d}\boldsymbol{r}, \\ V_{ijkl} &= \int \phi_i^*(\boldsymbol{r})\, \phi_j^*(\boldsymbol{r}')\, \hat{V}(\boldsymbol{r}, \boldsymbol{r}')\, \phi_k(\boldsymbol{r})\, \phi_l(\boldsymbol{r}')\, \mathrm{d}\boldsymbol{r}\, \mathrm{d}\boldsymbol{r}'. \end{aligned} \tag{4.6}$$

The operators $\hat{T}$ and $\hat{V}$ gather all the one-electron and two-electron interaction terms, respectively, and $\boldsymbol{r}$ denotes the set of orbital coordinates.

The Rayleigh-Ritz variational principle can be used to determine the ground state of such a system, by considering a family of *trial* wavefunctions and finding the member of that family, Ψ, which minimises the energy functional (4.2) [89, 90]. A necessary condition for the energy functional to be a minimum is that it should be *stationary*,

$$\delta E = \langle \delta\Psi | \hat{H} | \Psi \rangle + \langle \Psi | \hat{H} | \delta\Psi \rangle = 0, \tag{4.7}$$

with respect to *arbitrary variations* of the wavefunction, $\delta\Psi$. When condition (4.7) is satisfied, Ψ is said to be *variationally optimised* [89, 90]. Note that, since Ψ in general is *not* exact, this approach can only provide an *upper bound* to the ground

state energy, E_0:

$$\langle \Psi | \hat{H} | \Psi \rangle \geq E_0. \tag{4.8}$$

For a system with an even number of electrons, a good approximation to the ground state is the *closed-shell singlet state*,

$$|\Psi\rangle = |\phi_1 \, \bar{\phi}_1 \, \phi_2 \, \bar{\phi}_2 \cdots \phi_n \, \bar{\phi}_n \rangle, \tag{4.9}$$

which corresponds to a *single* Slater determinant where all the electrons are spin-paired in $n = N/2$ spin-up (ϕ_i) and spin-down ($\bar{\phi}_i$) states, possessing the same spatial parts. The energy of such a state can be written as [89, 90]

$$\begin{aligned} E &= 2 \sum_i{}' \langle \phi_i | \hat{T} | \phi_i \rangle + \sum_{i,k}{}' \Big(2 \langle \phi_i | \hat{J}_k | \phi_i \rangle - \langle \phi_i | \hat{K}_k | \phi_i \rangle \Big) \\ &= 2 \sum_i{}' T_{ii} + \sum_{i,k}{}' \big(2 J_{ik} - K_{ik} \big), \end{aligned} \tag{4.10}$$

where $\hat{J}_k$ and $\hat{K}_k$ are *Coulomb* and *exchange* operators [89, 90], defined by

$$\begin{aligned} \hat{J}_k (\boldsymbol{r}) \, \phi_i (\boldsymbol{r}) &= \left[\int \phi_k^* (\boldsymbol{r}') \, \hat{V} (\boldsymbol{r}, \boldsymbol{r}') \, \phi_k (\boldsymbol{r}') \, \mathrm{d}\boldsymbol{r}' \right] \phi_i (\boldsymbol{r}), \\ \hat{K}_k (\boldsymbol{r}) \, \phi_i (\boldsymbol{r}) &= \left[\int \phi_k^* (\boldsymbol{r}') \, \hat{V} (\boldsymbol{r}, \boldsymbol{r}') \, \phi_i (\boldsymbol{r}') \, \mathrm{d}\boldsymbol{r}' \right] \phi_k (\boldsymbol{r}), \end{aligned} \tag{4.11}$$

and the symbol $\sum'$ means that the sum runs only over occupied molecular orbitals (i.e., those included in the trial wavefunction), rather than a complete set. Note, however, that the existence of such a complete set can always be assumed [92], by further considering at least n virtual orbitals, ϕ_j, orthogonal to all the ϕ_i included in the wavefunction (4.9).

Variation of the energy with respect to the spatial parts of the molecular spin-orbitals yields

$$\delta E = 2 \sum_i{}' \Big(\langle \delta\phi_i | \hat{F} | \phi_i \rangle + \langle \phi_i | \hat{F} | \delta\phi_i \rangle \Big), \tag{4.12}$$

where we have introduced the (closed-shell) *Fock operator* [89, 90],

$$\hat{F} = \hat{T} + \sum_k{}' \big(2 \hat{J}_k - \hat{K}_k \big). \tag{4.13}$$

To enforce the stationarity condition (4.7), it is sufficient to consider a first order change in the wavefunction [92, 93], which can be made through the orbital variation $\delta\phi_i = \eta\,\phi_j$, i.e., by replacing the spatial part of one of the occupied states with $\phi_i + \eta\,\phi_j$, where ϕ_j is a virtual orbital and η an arbitrarily small complex number. It is clear that such a change preserves the orthonormality of the molecular orbitals,

$$\langle \delta\phi_i | \phi_j \rangle + \langle \phi_i | \delta\phi_j \rangle = 0, \tag{4.14}$$

and hence no further constraints are required [93]. Using the above orbital variation, we obtain

$$\eta^* \langle \phi_j | \hat{F} | \phi_i \rangle + \eta \langle \phi_i | \hat{F} | \phi_j \rangle = 0. \tag{4.15}$$

Replacing η with $\mathrm{i}\eta$, and comparing the resulting equation with the above expression, yields

$$\langle \phi_j | \hat{F} | \phi_i \rangle = \langle \phi_i | \hat{F} | \phi_j \rangle = 0, \tag{4.16}$$

which must hold for all pairs i, j of occupied and unoccupied states.

It is clear from equation (4.16) that the necessary condition to obtain a variational minimum only imposes the restriction that the matrix elements of the Fock operator connecting the occupied and virtual subspaces must vanish. In contrast, within both the occupied and unoccupied subspaces, they can be chosen *arbitrarily*. It is conventional to change to the representation in which $\hat{F}$ is diagonal [89, 90]. This can be accomplished by taking appropriate linear combinations of the occupied (unoccupied) orbitals to obtain the new occupied (unoccupied) states [92]. In this representation, we can write the *Hartree-Fock equation* in the *canonical* form [89, 90]

$$\hat{F} | \phi_i \rangle = \varepsilon_i | \phi_i \rangle, \tag{4.17}$$

where ε_i denotes an *orbital energy*, whose meaning will become clear in section 4.2.3. The original many-body problem is thus reduced to that of solving a *one-electron* Schrödinger equation, with an *effective* Hamiltonian describing an electron whose potential energy is given by its interaction with the remaining electrons in the system.

4.2.2 Spin-restricted formalism for general open-shell states

It is also instructive to consider the case of the ground state for a system with an odd number of electrons, as well as low-lying excited states for even-numbered systems. The latter are particularly important when preparing a photoexcitation dynamics simulation. Since the nuclei are much heavier than electrons, the nuclear coordinates immediately upon photoexcitation can be taken, to a good approximation, as those corresponding to the minimum of the *ground state* potential energy surface. However, the electronic wavefunction is better described by the *open-shell singlet state*,

$$|\Psi\rangle = \frac{1}{\sqrt{2}}\,|\phi_1\,\bar{\phi}_1\,\cdots\,\phi_{n-1}\,\bar{\phi}_{n-1}\,\phi_v\,\bar{\phi}_c\rangle + \frac{1}{\sqrt{2}}\,|\phi_1\,\bar{\phi}_1\,\cdots\,\phi_{n-1}\,\bar{\phi}_{n-1}\,\phi_c\,\bar{\phi}_v\rangle, \tag{4.18}$$

which corresponds to a sum of *two* Slater determinants, describing a singlet arrangement of a set of $n-1$ doubly occupied orbitals and two singly occupied orbitals, labelled 'v' and 'c' (motivated by the physical picture of an excitation from the valence band to the conduction band in periodic systems, e.g., conjugated polymers).

In this section, we apply the Rayleigh-Ritz variational principle to *general open-shell states*, which define a broad category of electronic states that includes those mentioned above, along with many others relevant for several physical processes of interest. They are characterised by an energy expression of the form [94–96]

$$E = \sum_{\mu}\sum_{i_\mu} n^\mu\, T_{i_\mu i_\mu} + \frac{1}{4}\sum_{\mu,\nu}\sum_{i_\mu,j_\nu} n^\mu\, n^\nu \big(2\, a^{\mu\nu} J_{i_\mu j_\nu} - b^{\mu\nu} K_{i_\mu j_\nu}\big), \tag{4.19}$$

where, following the notation of Kollmar [96], we have gathered groups of orbitals with the same occupancy and common sets of coefficients multiplying the two-electron terms in a *shell*, labelled by the Greek indices μ, ν. The occupation number of an orbital in shell μ is denoted by n^μ, and

$$\begin{aligned} a^{\mu\nu} &= a^{\nu\mu}, \\ b^{\mu\nu} &= b^{\nu\mu} \end{aligned} \tag{4.20}$$

are numerical coefficients (or *state parameters*) specific to the particular form of the wavefunction [94–96]. For instance, in the case of an open-shell singlet (i.e., a photoexcited state), all the doubly occupied orbitals belong to the same shell

(conventionally labelled by $\mu = 1$), whereas the singly occupied orbitals stand in separate shells (indexed by $\mu = 2, 3$). In this case, the state parameters are given by

$$\begin{aligned} \mathbf{a} &= \begin{pmatrix} 1 & 1 & 1 \\ 1 & 1 & 1 \\ 1 & 1 & 1 \end{pmatrix}, \\ \mathbf{b} &= \begin{pmatrix} 1 & 1 & 1 \\ 1 & 2 & -2 \\ 1 & -2 & 2 \end{pmatrix}. \end{aligned} \tag{4.21}$$

For high-spin multiplets, which include open-shell *doublet* (i.e., polaron) and *triplet* states, there are only two occupied shells ($\mu = 1$ gathers the doubly occupied orbitals, and $\mu = 2$ the singly occupied ones), and the state parameters read

$$\begin{aligned} \mathbf{a} &= \begin{pmatrix} 1 & 1 \\ 1 & 1 \end{pmatrix}, \\ \mathbf{b} &= \begin{pmatrix} 1 & 1 \\ 1 & 2 \end{pmatrix}. \end{aligned} \tag{4.22}$$

In principle, the sums in equation (4.19) extend only over occupied molecular orbitals. However, it is convenient to further consider the subspace of unoccupied orbitals as a proper shell, labelled by $\mu = 0$, which can be safely included in those sums since the various energy terms are always premultiplied by zero. Notice that the state parameters involving virtual orbitals are not defined, and therefore this shell is not included in the definitions of $\mathbf{a}$ and $\mathbf{b}$ given above.

Strictly speaking, in order to apply the Rayleigh-Ritz variational principle to an excited state, it is necessary to further enforce the orthogonality of the chosen wavefunction with all the lower energy many-body states [89, 90]. However, provided that the trial wavefunction is chosen wisely, and important symmetries are taken into account, such a constraint can be relaxed with good results [97]. We assume that such is the case for general open-shell states, as evidenced by the large number of different shell structures that may arise, and proceed with the usual variational method for ground states.

Variation of the energy (4.19) with respect to the spatial parts of the molecular spin-orbitals yields

$$\delta E = \sum_{\mu} \sum_{i_\mu} \Big(\langle \delta\phi_{i_\mu} | \, n^\mu \hat{F}^\mu | \phi_{i_\mu} \rangle + \langle \phi_{i_\mu} | \, n^\mu \hat{F}^\mu | \delta\phi_{i_\mu} \rangle \Big), \tag{4.23}$$

where we have introduced *generalised Fock operators* [94–96], given by (for $\mu \neq 0$)

$$\hat{F}^\mu = \hat{T} + \frac{1}{2} \sum_{\nu} \sum_{j_\nu} n^\nu \big(2\, a^{\mu\nu} \hat{J}_{j_\nu} - b^{\mu\nu} \hat{K}_{j_\nu} \big). \tag{4.24}$$

As in the work of Dahl *et al.* [93], we consider an orbital variation of the form

$$\delta\phi_{i_\mu} = \eta \, \phi_{j_\nu}. \tag{4.25}$$

In order to preserve the orthonormality of the molecular orbitals,

$$\langle \delta\phi_{i_\mu} | \phi_{j_\nu} \rangle + \langle \phi_{i_\mu} | \delta\phi_{j_\nu} \rangle = 0, \tag{4.26}$$

it is necessary to set

$$\delta\phi_{j_\nu} = -\eta^* \phi_{i_\mu}, \tag{4.27}$$

but no further constraints are required [93]. Inserting the variations (4.25) and (4.27) into equation (4.23), and applying the stationarity condition, we find

$$\eta^* \langle \phi_{j_\nu} | \, n^\mu \hat{F}^\mu - n^\nu \hat{F}^\nu | \phi_{i_\mu} \rangle + \eta \, \langle \phi_{i_\mu} | \, n^\mu \hat{F}^\mu - n^\nu \hat{F}^\nu | \phi_{j_\nu} \rangle = 0. \tag{4.28}$$

Substituting $\mathrm{i}\eta$ for η, and comparing the resulting equation with the above expression, yields

$$\langle \phi_{j_\nu} | \, n^\mu \hat{F}^\mu - n^\nu \hat{F}^\nu | \phi_{i_\mu} \rangle = 0, \tag{4.29}$$

which must be satisfied for all pairs of orbitals (including virtual states).

Equation (4.29) is the necessary condition to obtain a variational minimum for general open-shell states. Similarly to the case of a single Slater determinant, only the *intershell* inner products must vanish, while the *intrashell* terms are arbitrary. It is also possible to write an eigenvalue equation,

$$\hat{R} \, | \phi_{i_\mu} \rangle = \varepsilon_{i_\mu} | \phi_{i_\mu} \rangle, \tag{4.30}$$

by defining a single-particle operator, $\hat{R}$, whose eigenstates fulfill condition (4.29). This *unified coupling operator* [95, 96] has the general form

$$\hat{R} = \sum_{\mu} \hat{P}^{\mu} \hat{X}^{\mu} \hat{P}^{\mu} + \sum_{\mu,\nu\neq\mu} \lambda^{\mu\nu} \hat{P}^{\mu} \big(n^{\mu} \hat{F}^{\mu} - n^{\nu} \hat{F}^{\nu} \big) \hat{P}^{\nu}, \tag{4.31}$$

where $\hat{P}^{\mu}$ is a projector onto the subspace spanned by shell μ,

$$\hat{P}^{\mu} = \sum_{i_{\mu}} |\phi_{i_{\mu}}\rangle\langle\phi_{i_{\mu}}|, \tag{4.32}$$

$\lambda^{\mu\nu} = -\lambda^{\nu\mu}$ denotes a scalar *damping factor* [96, 98], and $\hat{X}^{\mu}$ is a Hermitian, but otherwise arbitrary, operator. As we shall see in the following section, the choice of the intrashell operators is of utmost importance in providing a physical meaning to the one-electron energies.

4.2.3 The physical meaning of the one-electron energies

As discussed in section 4.2.1, in its canonical form, the Hartree-Fock equation for a closed-shell singlet state provides a set of orbitals which diagonalise the (closed-shell) Fock operator. The diagonal elements, denoted ε_i, are termed *orbital energies*. Using equation (4.13) for the Fock operator, they are readily expressed as

$$\varepsilon_i = \langle\phi_i|\,\hat{F}\,|\phi_i\rangle = T_{ii} + {\sum_{k}}' \big(2\,J_{ik} - K_{ik} \big). \tag{4.33}$$

By simply summing over the N occupied states, we obtain

$${\sum_{i}}' \varepsilon_i = 2 {\sum_{i}}' T_{ii} + 2 {\sum_{i,k}}' \big(2\,J_{ik} - K_{ik} \big). \tag{4.34}$$

However, such quantity differs from the correct expectation value for a closed-shell singlet state,

$$E_N = 2 {\sum_{i}}' T_{ii} + {\sum_{i,k}}' \big(2\,J_{ik} - K_{ik} \big), \tag{4.35}$$

where a double counting of electron interaction terms is avoided [89, 90]. It is thus seen that the diagonal elements, ε_i, are not orbital energies in the traditional sense of giving the individual contributions of the orbitals to the total energy.

It is important to investigate what physical meaning may then be attached to the orbital energies. Let us start by considering the process of removing an electron from one of the doubly occupied molecular orbitals, say ϕ_d. Following this process, the closed-shell singlet state is transformed into an open-shell doublet, with state parameters given by expression (4.22). Assuming that only the shell structure is changed, but not the orbitals themselves, it is possible to compare the energies of the relevant N-electron and $(N-1)$-electron states [89, 90]. With the help of equation (4.19), we can write

$$E_{N-1} = 2\sum_{i\neq d}{}' T_{ii} + \sum_{i\neq d,k\neq d}{}' \big(2\,J_{ik} - K_{ik}\big) + T_{dd} + \sum_{k\neq d}{}' \big(2\,J_{dk} - K_{dk}\big) + J_{dd} - K_{dd}, \quad (4.36)$$

where all of the sums take the doubly occupied orbitals of the closed-shell singlet state as a reference and, hence, the symbol $\sum'$ is used. As it follows from the definitions of the Coulomb and exchange operators, we have

$$J_{dd} = K_{dd}. \quad (4.37)$$

Using this identity, and rearranging the summations in expression (4.36), yields

$$E_{N-1} = 2\sum_{i}{}' T_{ii} + \sum_{i,k}{}' \big(2\,J_{ik} - K_{ik}\big) - T_{dd} - \sum_{k}{}' \big(2\,J_{dk} - K_{dk}\big), \quad (4.38)$$

or, by comparing with equations (4.33) and (4.35),

$$E_{N-1} = E_N - \varepsilon_d. \quad (4.39)$$

The *ionisation potential* associated with the removal of an electron from a closed-shell singlet state is thus given by [89, 90]

$$I_p = E_{N-1} - E_N = -\varepsilon_d. \quad (4.40)$$

Let us now consider the process of adding an electron to one of the empty molecular orbitals, ϕ_e, to produce an $(N+1)$-electron state with a single unpaired electron. In the *frozen orbital approximation* (i.e., assuming that the orbitals do not change in the process), the energy of this open-shell doublet state can be written as

$$E_{N+1} = E_N + T_{ee} + \sum_{k}{}' \big(2\,J_{ek} - K_{ek}\big) + J_{ee} - K_{ee} = E_N + \varepsilon_e. \quad (4.41)$$

The *electron affinity* for such a process thus reads [89, 90]

$$E_a = E_N - E_{N+1} = -\varepsilon_e. \tag{4.42}$$

Equations (4.40) and (4.42) provide a clear physical significance to the canonical orbital energies: $-\varepsilon_d$ is an approximation to the ionisation energy required to create an $(N-1)$-electron doublet state, by removing an electron from the doubly occupied molecular orbital ϕ_d, whereas $-\varepsilon_e$ is approximately the electron affinity to produce an $(N+1)$-electron doublet, by adding an electron to the virtual orbital ϕ_e. This result is known as *Koopmans theorem* [89, 90].

As discussed in the previous section, in the case of general open-shell states it is also possible to write an eigenvalue equation analogous to the canonical Hartree-Fock equation for a closed-shell singlet state. Given the form of the unified coupling operator [equation (4.31)], the orbital energies can be expressed as [96]

$$\varepsilon_{i_\mu} = \langle \phi_{i_\mu} | \hat{X}^\mu | \phi_{i_\mu} \rangle, \tag{4.43}$$

and are thus entirely dependent on the choice of the intrashell operators, $\hat{X}^\mu$. It is instructive to investigate what choices may then lead to an interpretation of the orbital energies as approximate ionisation potentials and electron affinities. It is not clear whether a generalisation of Koopmans theorem is possible for all open-shell states [96, 99], and such a study must be carried out on a case-by-case basis. In the following, we will focus only on high-spin multiplets and open-shell singlet states.

Let us first consider the case of an N-electron multiplet with total spin $S > 0$, corresponding to a single Slater determinant in which a core of doubly occupied orbitals accommodates $N - 2S$ spin-paired electrons, and $2S$ orbitals are singly occupied with electrons of parallel spin. As we have seen in the previous section, for such a high-spin state the occupied orbitals fall into two different shells, and the state parameters are given by expression (4.22). According to equation (4.19), its energy can be written as

$$\begin{aligned} E_N = 2\sum_i{}' T_{ii} + \sum_{i,k}{}' \big(2\,J_{ik} - K_{ik}\big) + \sum_i{}'' T_{ii} + \frac{1}{2}\sum_{i,k}{}'' \big(J_{ik} - K_{ik}\big) + \\ + \sum_i{}' \sum_k{}'' \big(2\,J_{ik} - K_{ik}\big), \end{aligned} \tag{4.44}$$

where the symbol $\sum'$ means that the sum runs only over doubly occupied molecular orbitals (i.e., it spans the shell $\mu = 1$), and $\sum''$ is used for sums which extend over the singly occupied orbitals belonging to shell $\mu = 2$.

By removing an electron from one of the doubly occupied orbitals, ϕ_d, in such a way that the electron that is left behind is of parallel spin to the remaining unpaired electrons [99], we obtain an $(N-1)$-electron state of even higher spin. The single-determinant form of the wavefunction is maintained and, in the frozen orbital approximation, there is a mere transfer of an orbital from one shell to the other. The energy of the new state is given by

$$\begin{aligned} E^d_{N-1} = 2\sum_{i\neq d}{}' T_{ii} + \sum_{i\neq d, k\neq d}{}' \big(2\,J_{ik} - K_{ik}\big) + \sum_{i}{}'' T_{ii} + \frac{1}{2}\sum_{i,k}{}'' \big(J_{ik} - K_{ik}\big) + \\ + \sum_{i\neq d}{}' \sum_{k}{}'' \big(2\,J_{ik} - K_{ik}\big) + T_{dd} + \sum_{k\neq d}{}' \big(2\,J_{dk} - K_{dk}\big) + \\ + \sum_{k}{}'' \big(J_{dk} - K_{dk}\big). \end{aligned} \tag{4.45}$$

Rearranging the sums in the above expression, and comparing with equation (4.44), yields

$$E^d_{N-1} = E_N - T_{dd} - \sum_{k}{}' \big(2\,J_{dk} - K_{dk}\big) - \sum_{k}{}'' J_{dk}, \tag{4.46}$$

or, by using equation (4.24) for the relevant Fock operators,

$$E^d_{N-1} = E_N - \langle\phi_d|\,2\,\hat{F}^{(1)} - \hat{F}^{(2)}|\phi_d\rangle. \tag{4.47}$$

If we remove one of the unpaired electrons instead, the total spin is lowered and one of the singly occupied orbitals, say ϕ_s, is discarded from the Slater determinant. In the frozen orbital approximation, the energy of the produced $(N-1)$-electron state reads

$$E^s_{N-1} = E_N - T_{ss} - \sum_{k}{}' \big(2\,J_{sk} - K_{sk}\big) - \sum_{k}{}'' \big(J_{sk} - K_{sk}\big), \tag{4.48}$$

i.e.,

$$E^s_{N-1} = E_N - \langle\phi_s|\,\hat{F}^{(2)}|\phi_s\rangle. \tag{4.49}$$

Finally, suppose that we introduce an extra electron in the system, with spin parallel to the already existing electrons in the open-shell orbitals. A new orbital,

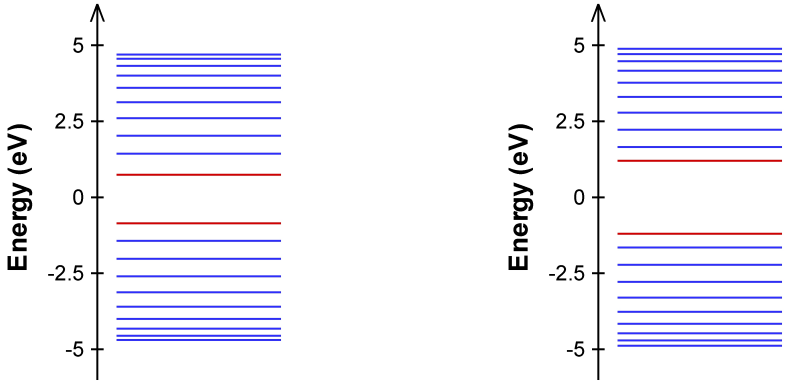

(a) (b)

Figure 4.1: Orbital energies obtained for a $1\,^1B_u$ *state in a perfectly dimerised* 20*-site PPP chain, considering intrashell operators of the forms* (4.52) *(a) and* (4.53) *(b). The model parameters were chosen as* $r_0 = 1.2$ Å, $t_0 = 2$ eV, $U = 4$ eV, $\beta = 3$, *and* $\delta = 0.1$, *typical of conjugated polymers* [44, 45]. *The energies of the singly occupied levels are shown in red.*

previously unoccupied, ϕ_e, is then added to the wavefunction, whose form remains that of a single Slater determinant. The shell structure is unchanged, as ϕ_e is simply appended to the singly occupied shell $\mu = 2$. The energy of the $(N+1)$-electron state thus created can be written as

$$\begin{aligned} E_{N+1} &= E_N + T_{ee} + {\sum_k}' \left(2\,J_{ek} - K_{ek}\right) + {\sum_k}'' \left(J_{ek} - K_{ek}\right) \\ &= E_N + \langle \phi_e | \, \hat{F}^{(2)} \, | \phi_e \rangle . \end{aligned} \tag{4.50}$$

It is clear from equations (4.47), (4.49) and (4.50) that the choice

$$\hat{X}^\mu = \begin{cases} 2\,\hat{F}^{(1)} - \hat{F}^{(2)} & \text{if } \mu = 1 \\ \hat{F}^{(2)} & \text{otherwise} \end{cases} \tag{4.51}$$

leads to an interpretation of the orbital energies for a high-spin multiplet state via a generalised Koopmans theorem [99], i.e., as approximate ionisation potentials and electron affinities.

A similar derivation shows that, in the case of an open-shell singlet state, the same can be achieved by choosing the intrashell operators

$$\hat{X}^\mu = \begin{cases} \hat{F}^{(1)} & \text{if } \mu = 0, 1 \\ \hat{F}^\mu & \text{otherwise} \end{cases} . \tag{4.52}$$

The orbital energies calculated with the above choice for a $1\,^1B_u$ state in a perfectly dimerised 20-site PPP chain are depicted in figure 4.1(a). Since the PPP Hamiltonian (as well as the other π-electron models discussed in the previous chapter) exhibits a *particle-hole symmetry* [45], one would expect the energies to be displaced symmetrically about the midgap. However, as can be seen in the figure, this is not the case, which possibly indicates a breakdown of the frozen orbital approximation. It is nevertheless convenient to neglect relaxation of the orbitals in the $(N \pm 1)$-electron states, and work with *effective* intrashell operators that strictly enforce particle-hole symmetry. For open-shell singlet states, we suggest using

$$\hat{X}^{\mu} = \begin{cases} 2\,\hat{F}^{(1)} - \frac{1}{2}\left(\hat{F}^{(2)} + \hat{F}^{(3)}\right) & \text{for the valence band } (\mu = 1, 2) \\ \frac{1}{2}\left(\hat{F}^{(2)} + \hat{F}^{(3)}\right) & \text{for the conduction band } (\mu = 0, 3) \end{cases} . \tag{4.53}$$

As shown in figure 4.1(b), this choice guarantees the expected symmetry of the orbital energies and, as such, should be preferred over expression (4.52).

4.3 Overview of self-consistent field algorithms

The numerical solution of the Hartree-Fock equations (4.17) or (4.30) requires the introduction of known spatial basis functions. Usually, these functions are chosen as a set of atomic orbitals, $\{\chi_i\}$, which we will assume orthonormal. Expanding the molecular orbitals as a *linear combination of atomic orbitals* (LCAO),

$$|\phi_{k_\mu}\rangle = \sum_i C_{ik_\mu} |\chi_i\rangle, \tag{4.54}$$

then leads to a set of equations which can be solved for the expansion coefficients, C_{ik_μ}, through standard matrix techniques [90]. For general open-shell states, we obtain

$$\sum_j R_{ij}\, C_{jk_\mu} = \varepsilon_{k_\mu}\, C_{ik_\mu}. \tag{4.55}$$

The matrix representation of the unified coupling operator can be written explicitly in the atomic orbitals basis set as

$$R_{ij} = \sum_\mu \sum_{k,l} P^\mu_{ik}\, X^\mu_{kl}\, P^\mu_{lj} + \sum_{\mu,\nu\neq\mu} \sum_{k,l} \lambda^{\mu\nu} P^\mu_{ik} \left(n^\mu F^\mu_{kl} - n^\nu F^\nu_{kl}\right) P^\nu_{lj}, \tag{4.56}$$

with

$$\begin{aligned} P_{ij}^{\mu} &= \sum_{k_\mu} C_{ik_\mu} C_{jk_\mu}^{*}, \\ F_{ij}^{\mu} &= \widetilde{T}_{ij} + \frac{1}{2} \sum_{\nu} \sum_{k,l} n^{\nu} P_{lk}^{\nu} \left(2\, a^{\mu\nu} \widetilde{V}_{ikjl} - b^{\mu\nu} \widetilde{V}_{iklj} \right), \end{aligned} \tag{4.57}$$

and

$$\begin{aligned} \widetilde{T}_{ij} &= \int \chi_i^{*}(\boldsymbol{r})\, \hat{T}(\boldsymbol{r})\, \chi_j(\boldsymbol{r})\, \mathrm{d}\boldsymbol{r}, \\ \widetilde{V}_{ijkl} &= \int \chi_i^{*}(\boldsymbol{r})\, \chi_j^{*}(\boldsymbol{r}')\, \hat{V}(\boldsymbol{r}, \boldsymbol{r}')\, \chi_k(\boldsymbol{r})\, \chi_l(\boldsymbol{r}')\, \mathrm{d}\boldsymbol{r}\, \mathrm{d}\boldsymbol{r}'. \end{aligned} \tag{4.58}$$

It is clear that the unified coupling matrix, $\mathbf{R}$, depends on the LCAO coefficients, via the projector and Fock matrices. Hence, equation (4.55) poses a nonlinear eigenvalue problem, which must be solved iteratively through a procedure called a *self-consistent field* algorithm [90].

The simplest approach is a *fixed-point iteration* scheme, introduced by Roothaan [100] and Hall [101]. Within this method, an initial guess for the expansion coefficients (which may be taken as the solution for the case without electron-electron interactions) is used to build a starting matrix $\mathbf{R}$, which is diagonalised to yield a new set of LCAO coefficients. A new unified coupling matrix can then be constructed and diagonalised, and this process is repeated until *self-consistency* is reached [100, 101]. Since consecutive sets of coefficients may be subject to trivial phase differences, it is convenient to introduce the *density matrix* [90],

$$\rho_{ij} = \sum_{\mu} n^{\mu} P_{ij}^{\mu} = \sum_{\mu} \sum_{k_\mu} n^{\mu} C_{ik_\mu} C_{jk_\mu}^{*}, \tag{4.59}$$

to define the stopping criterion. A self-consistent solution is thus said to be obtained when two successive densities are the same within a specified tolerance.

The Roothaan-Hall method has very slow and unstable convergence properties [102, 103], and typically works well only for simple cases. Several modifications to the original iterative procedure have been suggested [98, 104–106] to stabilise and improve its performance. A simple strategy is to combine consecutive densities, $\boldsymbol{\rho}_k$ and $\boldsymbol{\rho}_{k+1}$, according to the *damping* scheme [104]

$$\widetilde{\boldsymbol{\rho}}_{k+1} = \boldsymbol{\rho}_k + \lambda\, (\boldsymbol{\rho}_{k+1} - \boldsymbol{\rho}_k), \tag{4.60}$$

rather than taking the full fixed-point step, which uses the latest build of the density matrix. The idea is that if the *damping factor*, $0 < \lambda < 1$, is sufficiently small, the iterative sequence can be generated in a more controlled way, thus forcing convergence in some problematic cases [104]. A more general approach in the same spirit is to introduce *intershell damping factors* [98], $\lambda^{\mu\nu} = -\lambda^{\nu\mu}$, directly in the definition of the unified coupling matrix, which justifies the form of expression (4.56). A related strategy is to exploit the arbitrariness of the intrashell blocks, $\mathbf{X}^{\mu}$, to make sure that orbitals in different shells are well separated in energy, which can be accomplished by introducing *level-shift parameters* [98, 105]. When combined, the damping and level-shifting techniques can tackle even the most difficult convergence issues, provided that the damping factors and level-shifters are carefully chosen [98]. On the downside, such method lacks a systematic way to optimise these parameters, which can only be found on a trial-and-error basis.

The simple damping scheme of equation (4.60) can be thought of as performing a sort of extrapolation between two consecutive densities. A natural extension is to use the information gathered over multiple iteration steps to accelerate the convergence through a general extrapolation method. The most successful procedure designed to achieve this is known as *direct inversion in the iterative subspace* (DIIS) [106]. Central to this approach is the definition of a suitable *error vector*, $\mathbf{e}_k$, for every iteration k, whose vanishing is a necessary and sufficient convergence condition [106, 107]. A popular choice is the commutator between the unified coupling and density matrices [106, 107],

$$\mathbf{e}_k = \big[\mathbf{R}_k, \boldsymbol{\rho}_k\big] = \mathbf{R}_k\,\boldsymbol{\rho}_k - \boldsymbol{\rho}_k\,\mathbf{R}_k, \tag{4.61}$$

which is appropriate for systems where each shell has a unique occupation number. If this is not the case (e.g., for an open-shell singlet state), a possible choice can be formed from the intershell blocks of the unified coupling matrix alone [107]. The DIIS method attempts to find the linear combination of the latest m error vectors that provides the least-squares approximation to the zero vector [106]. This can be accomplished through the minimisation of the squared norm

$$S_m = \left| \sum_{k=1}^{m} \zeta_k\,\mathbf{e}_k \right|^2 \tag{4.62}$$

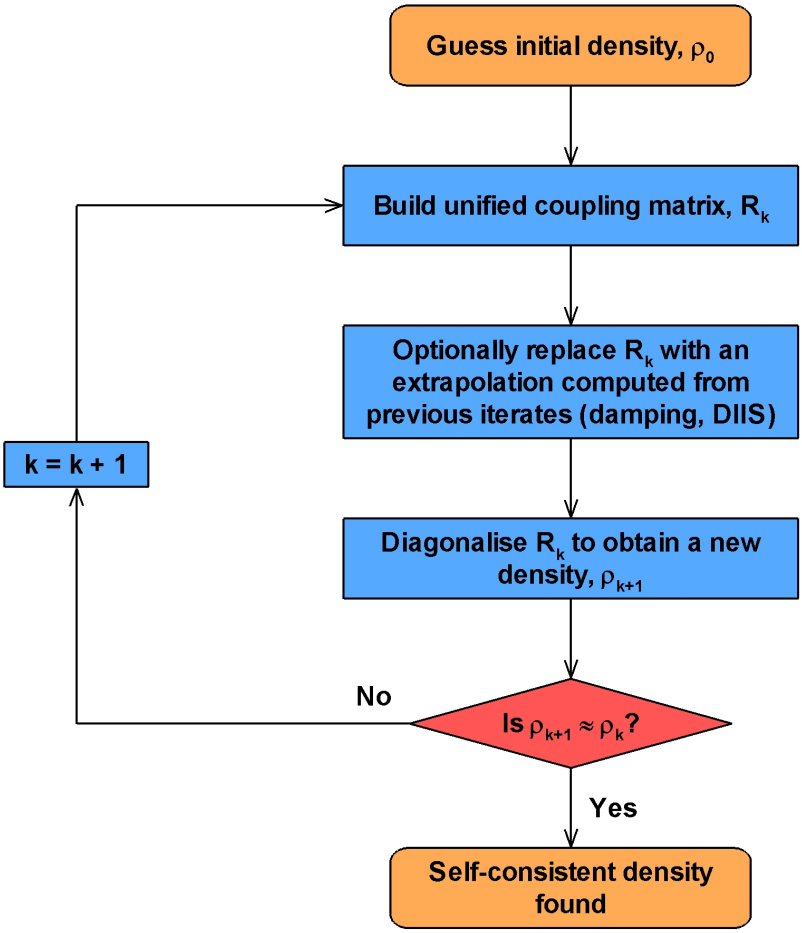

Figure 4.2: Flow diagram of the diagonalisation-based self-consistent field algorithms.

with respect to the coefficients ζ_k, subject to the constraint that they add up to one [106]:

$$\sum_{k=1}^{m} \zeta_k = 1. \tag{4.63}$$

An extrapolation of the previous m unified coupling matrices,

$$\widetilde{\mathbf{R}} = \sum_{k=1}^{m} \zeta_k \, \mathbf{R}_k, \tag{4.64}$$

can then be constructed and diagonalised to yield a new set of orbital coefficients, thus reestablishing the iterative procedure.

The flow diagram of figure 4.2 summarises the methods discussed so far. Despite having specific sets of building rules and parameters, they all share a common structure, which relies on the construction and diagonalisation of the unified coupling

matrix. An important limitation of such *diagonalisation-based* techniques is that, in general, there is no guarantee that the energy will decrease at each iteration. Such a desirable property can be met through the use of alternative approaches, which seek to minimise the Hartree-Fock energy (4.19) directly [96, 108, 109]. The *direct* (or *diagonalisation-free*) methods are built on the basis of an *exponential parameterisation* of the molecular orbitals, whereby the transformation of a set of LCAO coefficients into another one is expressed in terms of the exponential of an anti-Hermitian matrix of *orbital rotation* (or *mixing*) parameters, $\mathbf{q}$ [96, 108]:

$$\widetilde{\mathbf{C}} = \mathbf{C}\,\mathrm{e}^{\mathbf{q}}, \tag{4.65}$$

with

$$\mathbf{q} = -\,\mathbf{q}^{\dagger}. \tag{4.66}$$

The above parameterisation offers a convenient way to work with an independent set of *relevant* parameters. As discussed in previous sections, the variational minimisation of the energy only requires mixing orbitals that belong to different shells. In contrast, the mixing parameters associated with rotations between orbitals of the same shell may be disregarded, since those rotations do not change the electronic energy. The number of mixing parameters may be further reduced by exploiting additional symmetries of the molecular orbitals [96, 108, 109]. Such a description also allows for an easier handling of the orthonormality constraints, since the independent parameters are all contained in the upper-right (or lower-left) triangle of the matrix $\mathbf{q}$.

If the exponential is expanded into a suitably truncated power series, the open-shell electronic energy (4.19) can be approximated locally by a quadratic surface [96, 108], whose minimum is then given by the *Newton-Raphson equation* [91]

$$\mathbf{q} = -\,\mathbf{B}^{-1}\,\mathbf{g}, \tag{4.67}$$

where $\mathbf{g}$ is the energy *gradient* in the space of orbital rotation parameters, with elements given by [96, 108]

$$g_{i_\mu j_\nu} = 2\,\langle \phi_{i_\mu} | \, n^\nu \hat{F}^\nu - n^\mu \hat{F}^\mu \, | \phi_{j_\nu} \rangle, \tag{4.68}$$

and $\mathbf{B}$ denotes the matrix of second derivatives of the energy with respect to the mixing parameters, or *Hessian*. For general open-shell states, the Hessian is also known analytically [96, 108]. The successive application of equations (4.67) and (4.65) thus establishes a viable iterative procedure to perform the energy minimisation, which benefits from a quadratic convergence rate [96, 108]. However, such a method is impractical for large systems, since the dimension of the Hessian increases with the size of the basis set, N_{basis}, as N_{basis}^4. It is, therefore, convenient to avoid the explicit inversion of the Hessian, which can be a costly numerical operation, and use an approximate inverse matrix instead [96, 109].

The simplest approximation is to set the inverse Hessian to the identity matrix for every iteration k,

$$\mathbf{B}_k^{-1} = \mathbf{I}, \tag{4.69}$$

which forms the basis of the method of *steepest descent* [91]. A more sophisticated approach is to use the orbital rotation and gradient information accumulated from previous iterations to gradually build up an approximation to the inverse Hessian. The most successful algorithm devised in this spirit relies on the *BFGS update* formula [91, 109, 110]

$$\mathbf{B}_{k+1}^{-1} = \left(\mathbf{I} - \frac{\mathbf{q}_k \boldsymbol{\Delta}\mathbf{g}_k^T}{\boldsymbol{\Delta}\mathbf{g}_k^T \mathbf{q}_k}\right) \mathbf{B}_k^{-1} \left(\mathbf{I} - \frac{\boldsymbol{\Delta}\mathbf{g}_k \mathbf{q}_k^T}{\boldsymbol{\Delta}\mathbf{g}_k^T \mathbf{q}_k}\right) + \frac{\mathbf{q}_k \mathbf{q}_k^T}{\boldsymbol{\Delta}\mathbf{g}_k^T \mathbf{q}_k}, \tag{4.70}$$

where

$$\boldsymbol{\Delta}\mathbf{g}_k = \mathbf{g}_{k+1} - \mathbf{g}_k, \tag{4.71}$$

and we have taken all matrix elements as real. For large systems, with associated storage constraints, a good strategy is to consider only the orbital rotations and gradients obtained in the last m iteration steps. Together with the recursive evaluation of the product of the inverse Hessian and the gradient, this defines a *limited-memory* variant [110] of the BFGS method (LBFGS).

Another difficulty with the Newton-Raphson technique is encountered when the energy is not particularly well approximated by a quadratic function. This is the typical scenario in electronic structure calculations, especially when dealing with

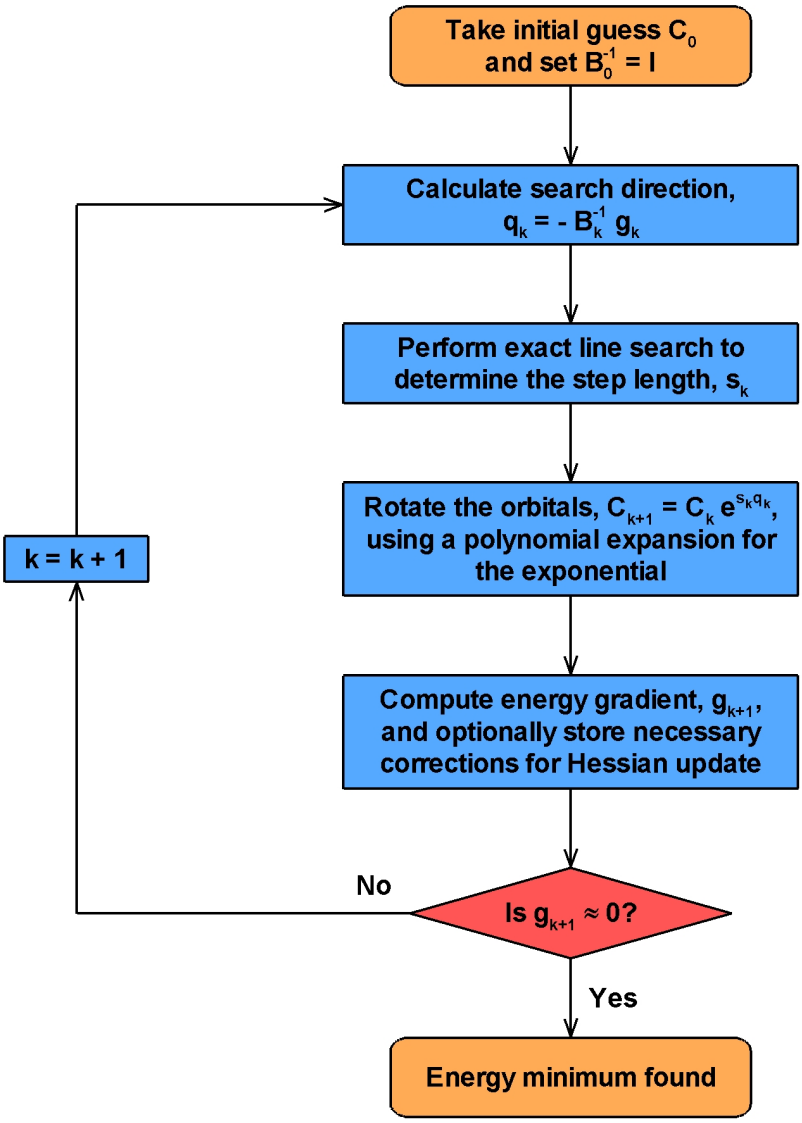

Figure 4.3: Flow diagram of the diagonalisation-free self-consistent field algorithms.

excited states [96]. The full *Newton step* (or *quasi-Newton*, as it is referred to if an approximate inverse Hessian is used) often leads outside of the quadratic region, and divergent behaviour is observed. A simple solution is to take a *restricted step* instead [91, 96],

$$\widetilde{\mathbf{q}}_k = s_k \, \mathbf{q}_k, \tag{4.72}$$

where the *step length*, s_k, is determined by minimising the energy along the direction $\mathbf{q}_k$, a procedure known as a *line search* [91]. For best results, an *exact* line search should be performed, but other possibilities exist [91]. In this sense, each iteration

is broken down into two parts. Equation (4.67) first defines a *search direction*, and then a step length is computed which decides how far the orbital rotation parameters should move in that direction. The iteration is completed by using equation (4.65) to obtain a new set of LCAO coefficients, and the process is repeated until the energy gradient becomes zero within a specified tolerance. Such is the basic structure of the diagonalisation-free methods devised to perform the energy minimisation, which are summarised in the flow diagram of figure 4.3.

The performance of some of the methods discussed in this section is illustrated in table 4.1, which lists the number of iterations they require to minimise the energy of several electronic states of relevance in a perfectly dimerised 60-site PPP chain. As can be seen, all of the techniques are able to successfully reach convergence for the ground state ($1\,^1A_g$), with DIIS proving to be the most efficient algorithm. It is clear from the table that the diagonalisation-based methods under scrutiny

Table 4.1: Convergence characteristics of different self-consistent field algorithms applied to a number of electronic states in a perfectly dimerised 60*-site PPP chain. The model parameters were chosen as* $r_0 = 1.2$ Å, $t_0 = 2$ eV, $U = 4$ eV, $\beta = 3$, *and* $\delta = 0.1$, *typical of conjugated polymers* [44, 45]. *For every method used, a calculation was considered to be converged when the Frobenius norm of the difference between consecutive densities was less than* 10^{-8}, *and was aborted if convergence was not reached in* 5000 *iterations (this is indicated by 'Failed'). Listed are the number of iterations required to achieve convergence for successful calculations, as well as the energy, in* eV, *of the converged state (given in brackets).*

State	Roothaan-Hall	Damping ($\lambda = 0.1$)	DIIS ($m = 5$)	Steepest descent	LBFGS ($m = 10$)
$1\,^1A_g$	14 (−522.88)	225 (−522.88)	10 (−522.88)	40 (−522.88)	38 (−522.88)
$1\,^2A_u$	Failed	Failed	23 (−522.01)	382 (−522.02)	61 (−522.02)
$1\,^1B_u$	Failed	Failed	36 (−521.35)	393 (−521.35)	66 (−521.35)
$1\,^3B_u$	Failed	Failed	Failed	400 (−521.56)	69 (−521.56)

typically fail to converge when dealing with excited states, with the scenario being most extreme for the first excited triplet, $1\,^3B_u$. The DIIS scheme provides the only exceptions to this rule, as it manages to successfully achieve convergence when applied to the electron-polaron doublet $1\,^2A_u$, and to the first excited singlet $1\,^1B_u$ (and does so efficiently), even though it does not necessarily lead to the best overall solutions. The diagonalisation-free techniques, on the other hand, prove to be very robust, as they converge for all the states considered. Additionally, they consistently provide the lowest energy solutions. The BFGS strategy is clearly more efficient than steepest descent and, as such, should be the preferred method to perform the energy minimisation.

Chapter 5

Approximate solution of the time-dependent Schrödinger equation

5.1 Ehrenfest molecular dynamics

The solution of the *time-dependent* Schrödinger equation for a system of interacting electrons and nuclei,

$$\mathrm{i}\hbar\,\frac{\partial}{\partial t}\,\Psi\left(\boldsymbol{r},\boldsymbol{R},t\right)=\hat{H}\;\Psi\left(\boldsymbol{r},\boldsymbol{R},t\right), \tag{5.1}$$

is generally a prohibitive task, for which *approximate methods* are necessary. A widely used approach is to consider the nuclei as *classical* particles, governed by Newton's laws, while treating the electrons *quantum-mechanically* [111, 112]. This section provides a derivation of the working equations of this method, known as *Ehrenfest molecular dynamics*.

In principle, $\hat{H}$ is the many-body Hamiltonian (3.1), but, in practice, a simplified form is used instead, as discussed in chapter 3. For the purpose of the following discussion, we will write

$$\begin{aligned}\hat{H}&=-\sum_{\alpha}\frac{\hbar^2}{2M_\alpha}\boldsymbol{\nabla}_\alpha^2+\hat{H}_\mathrm{e}\left(\boldsymbol{r},\boldsymbol{R}\right)\\&=-\sum_{\alpha}\frac{\hbar^2}{2M_\alpha}\boldsymbol{\nabla}_\alpha^2-\sum_{i}\frac{\hbar^2}{2m_\mathrm{e}}\boldsymbol{\nabla}_i^2+\hat{V}_\mathrm{e}\left(\boldsymbol{r},\boldsymbol{R}\right),\end{aligned} \tag{5.2}$$

where $\hat{V}_{\mathrm{e}}\left(\boldsymbol{r},\boldsymbol{R}\right)$ gathers all the potential energy terms. The starting point in the derivation is to decouple the electronic and nuclear degrees of freedom, through the product ansatz [111, 112]

$$\Psi\left(\boldsymbol{r},\boldsymbol{R},t\right)=\Psi_{\mathrm{e}}\left(\boldsymbol{r},t\right)\,\Psi_{\mathrm{n}}\left(\boldsymbol{R},t\right)\,\exp\left[\frac{\mathrm{i}}{\hbar}\int_{t_0}^{t}\widetilde{E}_{\mathrm{e}}\left(t'\right)\,\mathrm{d}t'\right], \tag{5.3}$$

where a suitable phase factor,

$$\widetilde{E}_{\mathrm{e}}\left(t\right)=\int\Psi_{\mathrm{e}}^{*}\left(\boldsymbol{r},t\right)\,\Psi_{\mathrm{n}}^{*}\left(\boldsymbol{R},t\right)\,\hat{H}_{\mathrm{e}}\left(\boldsymbol{r},\boldsymbol{R}\right)\,\Psi_{\mathrm{e}}\left(\boldsymbol{r},t\right)\,\Psi_{\mathrm{n}}\left(\boldsymbol{R},t\right)\,\mathrm{d}\boldsymbol{r}\,\mathrm{d}\boldsymbol{R}, \tag{5.4}$$

has been included. Although similar in spirit to the Born-Oppenheimer separation (3.5), this ansatz differs from the former in that the electronic wavefunction, $\Psi_{\mathrm{e}}\left(\boldsymbol{r},t\right)$, is *not*, in general, an eigenfunction of $\hat{H}_{\mathrm{e}}\left(\boldsymbol{r},\boldsymbol{R}\right)$ (i.e., the Born-Oppenheimer Hamiltonian).

Inserting (5.3) into the time-dependent Schrödinger equation, multiplying from the left with $\Psi_{\mathrm{e}}^{*}\left(\boldsymbol{r},t\right)$ and $\Psi_{\mathrm{n}}^{*}\left(\boldsymbol{R},t\right)$, integrating over $\boldsymbol{r}$ and $\boldsymbol{R}$, and imposing energy conservation, yields [111, 112]

$$\begin{aligned}
\mathrm{i}\hbar\,\frac{\partial\Psi_{\mathrm{e}}}{\partial t}&=-\sum_{i}\frac{\hbar^{2}}{2m_{\mathrm{e}}}\,\boldsymbol{\nabla}_{i}^{2}\Psi_{\mathrm{e}}+\left[\int\Psi_{\mathrm{n}}^{*}\left(\boldsymbol{R},t\right)\,\hat{V}_{\mathrm{e}}\left(\boldsymbol{r},\boldsymbol{R}\right)\,\Psi_{\mathrm{n}}\left(\boldsymbol{R},t\right)\,\mathrm{d}\boldsymbol{R}\right]\Psi_{\mathrm{e}},\\
\mathrm{i}\hbar\,\frac{\partial\Psi_{\mathrm{n}}}{\partial t}&=-\sum_{\alpha}\frac{\hbar^{2}}{2M_{\alpha}}\,\boldsymbol{\nabla}_{\alpha}^{2}\Psi_{\mathrm{n}}+\left[\int\Psi_{\mathrm{e}}^{*}\left(\boldsymbol{r},t\right)\,\hat{H}_{\mathrm{e}}\left(\boldsymbol{r},\boldsymbol{R}\right)\,\Psi_{\mathrm{e}}\left(\boldsymbol{r},t\right)\,\mathrm{d}\boldsymbol{r}\right]\Psi_{\mathrm{n}}.
\end{aligned} \tag{5.5}$$

This set of coupled equations forms the basis of the *time-dependent self-consistent field* method [111, 112]. Both electrons and nuclei evolve according to the laws of quantum mechanics, in *time-dependent effective potentials* which are obtained by *averaging* over the other type of particles. Hence, the product ansatz (5.3) leads to a *mean-field* description of the coupled electron-nuclear dynamics.

To proceed with the derivation, it is necessary to approximate the nuclei as classical point particles. To this end, we write the nuclear wavefunction, $\Psi_{\mathrm{n}}\left(\boldsymbol{R},t\right)$, as [111, 112]

$$\Psi_{\mathrm{n}}\left(\boldsymbol{R},t\right)=A\left(\boldsymbol{R},t\right)\,\exp\left[\frac{\mathrm{i}}{\hbar}\,S\left(\boldsymbol{R},t\right)\right], \tag{5.6}$$

where the amplitude, $A\left(\boldsymbol{R},t\right)>0$, and the phase factor, $S\left(\boldsymbol{R},t\right)$, can be taken as real. Substitution into the equation for the nuclear degrees of freedom in the coupled

system (5.5), leads to a new set of equations in terms of these variables [111, 112]:

$$\begin{aligned}
&\frac{\partial A}{\partial t} + \sum_{\alpha} \frac{1}{M_\alpha} \boldsymbol{\nabla}_\alpha A \, \boldsymbol{\nabla}_\alpha S + \sum_{\alpha} \frac{1}{2M_\alpha} A \, \boldsymbol{\nabla}_\alpha^2 S = 0, \\
&\frac{\partial S}{\partial t} + \sum_{\alpha} \frac{1}{2M_\alpha} \left(\boldsymbol{\nabla}_\alpha S\right)^2 + \int \Psi_{\mathrm{e}}^* \, \hat{H}_{\mathrm{e}} \, \Psi_{\mathrm{e}} \, \mathrm{d}\boldsymbol{r} = \hbar^2 \sum_{\alpha} \frac{1}{2M_\alpha} \frac{\boldsymbol{\nabla}_\alpha^2 A}{A}.
\end{aligned} \tag{5.7}$$

The first equation simply guarantees that the probability density of the nuclei, $\left|\Psi_{\mathrm{n}}\left(\boldsymbol{R}, t\right)\right|^2 \equiv A^2\left(\boldsymbol{R}, t\right)$, is locally invariant under a flow. However, we are mostly interested in the equation of motion for $S\left(\boldsymbol{R}, t\right)$. The right-hand side of this second equation is proportional to $\hbar^2$, and thus becomes negligible in the classical limit, $\hbar \to 0$:

$$\frac{\partial S}{\partial t} + \sum_{\alpha} \frac{1}{2M_\alpha} \left(\boldsymbol{\nabla}_\alpha S\right)^2 + \int \Psi_{\mathrm{e}}^* \, \hat{H}_{\mathrm{e}} \, \Psi_{\mathrm{e}} \, \mathrm{d}\boldsymbol{r} = 0. \tag{5.8}$$

The expression that emerges has the form of the *Hamilton-Jacobi equation* of classical mechanics [113],

$$\frac{\partial S}{\partial t} + H\left(\boldsymbol{R}, \boldsymbol{\nabla} S\right) = 0, \tag{5.9}$$

where the classical Hamiltonian,

$$H\left(\boldsymbol{R}, \boldsymbol{P}\right) = T\left(\boldsymbol{P}\right) + V\left(\boldsymbol{R}\right), \tag{5.10}$$

is a function of the nuclear coordinates, $\boldsymbol{R}$, and their conjugated momenta, defined as $\boldsymbol{P} \equiv \boldsymbol{\nabla} S$. The associated Newtonian equations of motion thus read [111–113]

$$\begin{aligned}
M_\alpha \, \ddot{\boldsymbol{R}}_\alpha(t) &= \boldsymbol{F}_\alpha\left(\boldsymbol{R}(t)\right) \\
&= -\boldsymbol{\nabla}_\alpha \int \Psi_{\mathrm{e}}^*(\boldsymbol{r}, t) \, \hat{H}_{\mathrm{e}}\left(\boldsymbol{r}, \boldsymbol{R}\right) \, \Psi_{\mathrm{e}}(\boldsymbol{r}, t) \, \mathrm{d}\boldsymbol{r}.
\end{aligned} \tag{5.11}$$

The nuclear motion now follows the laws of classical mechanics, with an effective potential produced by the electrons.

For consistency, the nuclear wavefunction appearing in the equation for the electronic degrees of freedom in the coupled system (5.5) must be replaced by the nuclear positions. In this classical limit, a time-dependent wave equation is obtained for the electrons [111, 112]:

$$\mathrm{i}\hbar \, \frac{\partial}{\partial t} \Psi_{\mathrm{e}}(\boldsymbol{r}, t) = \hat{H}_{\mathrm{e}}\left(\boldsymbol{r}, \boldsymbol{R}\right) \, \Psi_{\mathrm{e}}(\boldsymbol{r}, t). \tag{5.12}$$

The above expression, together with (5.11) for the nuclei, describes the self-consistent evolution of the entire system. The nuclei are considered as classical particles, obeying Newton's laws, while the electrons are still treated quantum-mechanically.

The set of coupled equations (5.11) and (5.12) forms the basis of the *Ehrenfest molecular dynamics* method. Although at the foundation of Ehrenfest molecular dynamics lies a mean-field approach, transitions between different electronic states are possible in this formalism [111, 112], which is therefore *nonadiabatic*. However, at this level of approximation, not all transitions are properly reproduced; the quantum electron-ion correlation is partially missed, leading to an inadequate description of nonadiabatic processes governed by spontaneous phonon emission, such as *Joule heating* [114]. A more accurate description of the electron-nuclear interaction can be obtained through a number of alternative approaches, which have been successfully applied to conjugated polymers [115–117]. These include *surface hopping* [115] and quantum dynamical methods, such as *correlated electron-ion dynamics* [116] and the *hierarchical electron-phonon model* of Tamura *et al.* [117]. Nevertheless, whenever the quantum nature of the nuclear motion can be safely neglected (as for the object of this thesis), Ehrenfest molecular dynamics is the method of choice in condensed phase dynamics because of its efficiency, which enables the study of large systems over several hundreds (and even thousands) of femtoseconds.

5.2 The multiconfigurational time-dependent Hartree-Fock approximation

5.2.1 General formalism

If the electronic part of the Hamiltonian only contains *one-body* operators, as in the case of the SSH model, the solution of equation (5.12) is trivial (the individual single-electron wavefunctions evolve independently according to the time-dependent Schrödinger equation). However, when *two-body* operators are present, such as the electron-electron interaction terms in the SSH + PPP model, further approximations are required. This section provides a derivation of the *multiconfigurational*

time-dependent Hartree-Fock method, which allows for an approximate solution of the time-dependent Schrödinger equation for the electronic degrees of freedom, by restricting the wavefunction to a specified form. We will focus on the case of general open-shell states, which are relevant for many physical processes of interest, such as the dynamics of photoexcitations in molecules.

We start by writing the Hamiltonian describing a system of N interacting electrons in the generalised form [92]

$$\hat{H} = \sum_{i,j} T_{ij}\, \hat{c}_i^\dagger\, \hat{c}_j + \frac{1}{2} \sum_{i,j,k,l} V_{ijkl}\, \hat{c}_i^\dagger\, \hat{c}_j^\dagger\, \hat{c}_l\, \hat{c}_k, \tag{5.13}$$

where $\hat{c}_i^\dagger$ ($\hat{c}_i$) creates (annihilates) an electron in the molecular spin-orbital ϕ_i, and

$$\begin{aligned} T_{ij} &= \int \phi_i^* \left(\boldsymbol{\xi}\right) \hat{T} \left(\boldsymbol{\xi}\right) \phi_j \left(\boldsymbol{\xi}\right) \mathrm{d}\boldsymbol{\xi}, \\ V_{ijkl} &= \int \phi_i^* \left(\boldsymbol{\xi}\right) \phi_j^* \left(\boldsymbol{\xi}'\right) \hat{V} \left(\boldsymbol{\xi}, \boldsymbol{\xi}'\right) \phi_k \left(\boldsymbol{\xi}\right) \phi_l \left(\boldsymbol{\xi}'\right) \mathrm{d}\boldsymbol{\xi}\, \mathrm{d}\boldsymbol{\xi}'. \end{aligned} \tag{5.14}$$

The operators $\hat{T}$ and $\hat{V}$ gather all the one-electron and electron-electron interactions, respectively, and $\boldsymbol{\xi} = \{\boldsymbol{r}, \sigma\}$ denotes collectively the orbital and spin coordinates of an electron.

The task of finding an approximate solution to the time-dependent Schrödinger equation (5.12) requires that we specify an ansatz for the electronic wavefunction. We will assume that this has the form of a *superposition of Slater determinants*,

$$|\Psi\rangle = \sum_{\boldsymbol{\alpha}} C_{\boldsymbol{\alpha}}\, |\phi_{\alpha_1} \cdots \phi_{\alpha_N}\rangle \equiv \sum_{\boldsymbol{\alpha}} C_{\boldsymbol{\alpha}}\, |\Phi_{\boldsymbol{\alpha}}\rangle, \tag{5.15}$$

with *fixed* expansion coefficients, $C_{\boldsymbol{\alpha}}$. Although this multiconfigurational form is quite general, we have in mind a *minimal* description of the electronic wavefunction, which retains the smallest possible number of Slater determinants required to generate an eigenfunction of the spin operator. In this case, the expansion coefficients are uniquely defined (up to an overall phase factor) and can be regarded as time-independent. For instance, in a photoexcitation process, absorption of a photon creates an open-shell singlet state, which can be written as a sum of two Slater determinants, provided that electron correlation is not too important. The time evolution of such a state, under a spin-independent Hamiltonian, clearly does not

introduce a phase difference between the two configurations, in order to preserve the proper spin symmetry. For this reason, in a minimal model to study the dynamics of such an excited state, the expansion coefficients can be considered time-independent.

Each *configuration* in equation (5.15), $\Phi_{\boldsymbol{\alpha}}$, is built using N molecular spin-orbitals, indexed by α_i, from the complete set $\{\phi_j\}$. Although some orbitals may not be included in the expansion, the existence of such a complete set can always be assumed [92]. Our goal is then to derive a set of *optimal* equations of motion for the (single-particle) molecular spin-orbitals. Stated in an equivalent way, we wish to find a single-particle, Hermitian operator, $\hat{R}$, that provides the *best self-consistent approximation* to the true evolution of the many-body wavefunction, Ψ:

$$\mathrm{i}\hbar\,|\dot{\Psi}\rangle \approx \hat{R}\,|\Psi\rangle = \sum_{i,j} R_{ij}\,\hat{c}_i^{\dagger}\,\hat{c}_j\,|\Psi\rangle, \tag{5.16}$$

where

$$R_{ij} = \int \phi_i^*\left(\boldsymbol{\xi}\right)\,\hat{R}\left(\boldsymbol{\xi}\right)\,\phi_j\left(\boldsymbol{\xi}\right)\,\mathrm{d}\boldsymbol{\xi} = \mathrm{i}\hbar\int \phi_i^*\left(\boldsymbol{\xi}\right)\,\dot{\phi}_j\left(\boldsymbol{\xi}\right)\,\mathrm{d}\boldsymbol{\xi}. \tag{5.17}$$

Note that $\hat{R}\,|\Psi\rangle$ is equivalent to a sum over the time derivatives of the single-particle orbitals. It is clear that this can only provide an approximation to the true evolution of the many-body wavefunction, since $\hat{R}$ is a single-particle operator, unlike the Hamiltonian (5.13). This is a fundamental consequence of keeping the coefficients fixed in the wavefunction expansion, which is meant to be highlighted through the use of the approximation sign in equation (5.16).

The evolution operator $\hat{R}$ (and, hence, the optimal equations of motion for the molecular orbitals) may be found using the *Dirac-Frenkel time-dependent variational principle* [89, 90, 118]. In this formalism, the *action integral* [118]

$$I\left[\Psi\right] = \int_{t_1}^{t_2} \langle\Psi|\,\hat{H} - \mathrm{i}\hbar\frac{\partial}{\partial t}\,|\Psi\rangle\;\mathrm{d}t \tag{5.18}$$

is varied with fixed end points. This procedure yields the variational equation

$$\langle\delta\Psi|\left(\hat{H} - \mathrm{i}\hbar\frac{\partial}{\partial t}\right)\Psi\rangle + \langle\left(\hat{H} - \mathrm{i}\hbar\frac{\partial}{\partial t}\right)\Psi|\delta\Psi\rangle = 0, \tag{5.19}$$

which must be satisfied for *arbitrary variations*, $\delta\Psi$, of the approximate many-body wavefunction, Ψ. Although equation (5.19) is usually stated directly as the

Dirac-Frenkel variational principle [89, 90], it should be stressed that the integral formulation is the more fundamental one, and is required to explain the presence of the time derivative acting on the bra (in the second term) by partial integration.

To write the variation, let us consider the effect of a small rotation of the orthonormal set of molecular orbitals:

$$|\phi_i'\rangle = \sum_j \mathrm{e}^{\Delta_{ji}} |\phi_j\rangle. \tag{5.20}$$

Notice that, since the new orbitals also form an orthonormal set, the matrix of *orbital rotation* (or *mixing*) parameters, $\mathbf{\Delta}$, must be anti-Hermitian:

$$\Delta_{ij} = -\Delta_{ji}^*. \tag{5.21}$$

The transformed wavefunction can be written as

$$|\Psi'\rangle = \sum_{\boldsymbol{\alpha}} C_{\boldsymbol{\alpha}} \prod_i{}' \hat{c}_i'^{\dagger} \hat{c}_i |\Phi_{\boldsymbol{\alpha}}\rangle, \tag{5.22}$$

where the symbol $\prod'$ means that the product runs over the subset of spin-orbitals included in $\Phi_{\boldsymbol{\alpha}}$, and $\hat{c}_i'^{\dagger}$ creates an electron in the rotated orbital ϕ_i'. This operator can be expressed in the basis of the original orbitals as [92]

$$\hat{c}_i'^{\dagger} = \sum_j \langle \phi_j | \phi_i' \rangle \, \hat{c}_j^{\dagger}, \tag{5.23}$$

or, since we are considering small rotations,

$$\hat{c}_i'^{\dagger} \approx \sum_j \left(\delta_{ji} + \Delta_{ji} \right) \hat{c}_j^{\dagger}. \tag{5.24}$$

Inserting equation (5.24) into (5.22), we obtain, to first order in $\mathbf{\Delta}$,

$$\begin{aligned} |\Psi'\rangle &\approx \sum_{\boldsymbol{\alpha}} C_{\boldsymbol{\alpha}} \left[\prod_i{}' \hat{c}_i^{\dagger} \hat{c}_i |\Phi_{\boldsymbol{\alpha}}\rangle + \sum_i{}' \sum_j \Delta_{ji} \hat{c}_j^{\dagger} \hat{c}_i |\Phi_{\boldsymbol{\alpha}}\rangle \right] \\ &= |\Psi\rangle + \sum_{i,j} \Delta_{ji} \hat{c}_j^{\dagger} \hat{c}_i |\Psi\rangle, \end{aligned} \tag{5.25}$$

from which we identify

$$|\delta\Psi\rangle = \sum_{i,j} \Delta_{ji} \hat{c}_j^{\dagger} \hat{c}_i |\Psi\rangle. \tag{5.26}$$

This methodology has the obvious advantage of incorporating the orthonormality constraints by construction. Furthermore, it provides physical insight into the structure of the variation, thus facilitating the elimination of redundant parameters, which is of key importance.

Combining expressions (5.16), (5.19), (5.21) and (5.26), the variational equation can be recast in the form

$$\sum_{i,j} \Delta_{ij} \, \langle \Psi | \big[\hat{H} - \hat{R}, \hat{c}_i^\dagger \, \hat{c}_j \big] | \Psi \rangle = 0, \tag{5.27}$$

or, after inserting the Hamiltonian (5.13) and doing some operator algebra,

$$\begin{aligned} \sum_{i,j} \Delta_{ij} \Bigg\{ \sum_k \Big[\big(T_{ki} - R_{ki} \big) \, \rho_{kj}^{(1)} - \big(T_{jk} - R_{jk} \big) \, \rho_{ik}^{(1)} \Big] + \\ + \sum_{k,l,m} \Big[V_{klim} \, \rho_{klmj}^{(2)} - V_{jkml} \, \rho_{iklm}^{(2)} \Big] \Bigg\} = 0, \end{aligned} \tag{5.28}$$

where

$$\begin{aligned} \rho_{ij}^{(1)} &= \langle \Psi | \, \hat{c}_i^\dagger \, \hat{c}_j \, | \Psi \rangle, \\ \rho_{ijkl}^{(2)} &= \langle \Psi | \, \hat{c}_i^\dagger \, \hat{c}_j^\dagger \, \hat{c}_k \, \hat{c}_l \, | \Psi \rangle \end{aligned} \tag{5.29}$$

denote the *one-* and *two-body reduced density matrices* [92, 119], respectively. Equation (5.28) constitutes the basic working equation of the *multiconfigurational time-dependent Hartree-Fock* method. To carry on the derivation of the equations of motion for the single-particle orbitals, it is necessary to further specify the form of the one- and two-body reduced density matrices. After discussing the conservation properties of the method, we will do so for general open-shell states, with the special cases of closed-shell and open-shell singlet states being treated explicitly.

5.2.2 Conservation properties

In order to obtain proper dynamics, it is crucial that the equations of motion conserve energy (for time-independent Hamiltonians) and preserve the orthonormality of the molecular spin-orbitals. To establish energy conservation, we can resort to the Dirac-Frenkel variational principle directly. In general, we can write [89]

$$| \delta \Psi \rangle = | \dot{\Psi} \rangle \, \delta t. \tag{5.30}$$

Substitution into equation (5.19), yields

$$\langle \dot{\Psi} | \hat{H} | \Psi \rangle + \langle \Psi | \hat{H} | \dot{\Psi} \rangle = 0, \tag{5.31}$$

which shows that energy is conserved throughout the dynamics if the Hamiltonian is time-independent. The conservation of orthonormality,

$$\frac{\mathrm{d}}{\mathrm{d}t} \langle \phi_i | \phi_j \rangle = \langle \dot{\phi}_i | \phi_j \rangle + \langle \phi_i | \dot{\phi}_j \rangle = 0, \tag{5.32}$$

follows trivially from the requirement that the effective single-particle operator $\hat{R}$ is Hermitian, on view of equation (5.17).

5.2.3 Application to a closed-shell singlet state

We now specialise the variational approach of section 5.2.1 to the case of a *closed-shell singlet* state and a *spin-independent* Hamiltonian. The wavefunction takes the form of a *single* Slater determinant:

$$|\Psi\rangle = |\phi_1 \, \bar{\phi}_1 \, \phi_2 \, \bar{\phi}_2 \, \cdots \, \phi_n \, \bar{\phi}_n \rangle. \tag{5.33}$$

In the above expression, ϕ_i ($\bar{\phi}_i$) denotes a spin-up (spin-down) state and $n = N/2$. Spin symmetry suggests the use of a *restricted* formalism, for which the spin-up and spin-down states possess the same orbital part. It also suggests that we set

$$\Delta_{i\sigma_i, j\sigma_j} = \widetilde{\Delta}_{ij} \, \delta_{\sigma_i \sigma_j}, \tag{5.34}$$

thus considering only the mixing between the spatial parts of the molecular spin-orbitals. The relevant operators are all spin-independent, with matrix elements satisfying

$$\begin{aligned} T_{i\sigma_i, j\sigma_j} &= \widetilde{T}_{ij} \, \delta_{\sigma_i \sigma_j}, \\ V_{i\sigma_i j\sigma_j, k\sigma_k l\sigma_l} &= \widetilde{V}_{ijkl} \, \delta_{\sigma_i \sigma_k} \, \delta_{\sigma_j \sigma_l}, \\ R_{i\sigma_i, j\sigma_j} &= \widetilde{R}_{ij} \, \delta_{\sigma_i \sigma_j}, \end{aligned} \tag{5.35}$$

where

$$\begin{aligned} \widetilde{T}_{ij} &= \int \phi_i^* (\boldsymbol{r}) \, \hat{T} (\boldsymbol{r}) \, \phi_j (\boldsymbol{r}) \, \mathrm{d}\boldsymbol{r}, \\ \widetilde{V}_{ijkl} &= \int \phi_i^* (\boldsymbol{r}) \, \phi_j^* (\boldsymbol{r}') \, \hat{V} (\boldsymbol{r}, \boldsymbol{r}') \, \phi_k (\boldsymbol{r}) \, \phi_l (\boldsymbol{r}') \, \mathrm{d}\boldsymbol{r} \, \mathrm{d}\boldsymbol{r}', \\ \widetilde{R}_{ij} &= \int \phi_i^* (\boldsymbol{r}) \, \hat{R} (\boldsymbol{r}) \, \phi_j (\boldsymbol{r}) \, \mathrm{d}\boldsymbol{r} = \mathrm{i}\hbar \int \phi_i^* (\boldsymbol{r}) \, \dot{\phi}_j (\boldsymbol{r}) \, \mathrm{d}\boldsymbol{r}, \end{aligned} \tag{5.36}$$

and ϕ_i now denotes the spatial part of the molecular spin-orbitals alone.

Using the standard rules for the behaviour of creation and annihilation operators [92], the elements of the one- and two-body reduced density matrices can be easily computed. The result is

$$\begin{aligned}
&\rho^{(1)}_{i\sigma_i,j\sigma_j} = \delta_{ij}\,\delta_{\sigma_i\sigma_j},\\
&\rho^{(2)}_{i\sigma_i j\sigma_j,k\sigma_k l\sigma_l} = \delta_{il}\,\delta_{jk}\,\delta_{\sigma_i\sigma_l}\,\delta_{\sigma_j\sigma_k} - \delta_{ik}\,\delta_{jl}\,\delta_{\sigma_i\sigma_k}\,\delta_{\sigma_j\sigma_l},
\end{aligned} \tag{5.37}$$

when all the indices refer to occupied orbitals, and zero otherwise. Inserting (5.37) into (5.28), we can write the variational condition as

$$\begin{aligned}
&\sum_{i,\sigma_i}\sum_{j,\sigma_j}{}' \Delta_{i\sigma_i,j\sigma_j}\left[\left(T_{j\sigma_j,i\sigma_i} - R_{j\sigma_j,i\sigma_i}\right) + \sum_{k,\sigma_k}{}'\left(V_{j\sigma_j k\sigma_k,i\sigma_i k\sigma_k} - V_{j\sigma_j k\sigma_k,k\sigma_k i\sigma_i}\right)\right] -\\
&-\sum_{i,\sigma_i}{}'\sum_{j,\sigma_j}\Delta_{i\sigma_i,j\sigma_j}\left[\left(T_{j\sigma_j,i\sigma_i} - R_{j\sigma_j,i\sigma_i}\right) + \sum_{k,\sigma_k}{}'\left(V_{j\sigma_j k\sigma_k,i\sigma_i k\sigma_k} - V_{j\sigma_j k\sigma_k,k\sigma_k i\sigma_i}\right)\right] = 0,
\end{aligned} \tag{5.38}$$

where the symbol $\sum'$ means that the sum extends only over occupied molecular orbitals. Performing the summations over spin, with the help of relations (5.34) and (5.35), yields

$$\begin{aligned}
&\sum_{i}\sum_{j}{}' 2\,\widetilde{\Delta}_{ij}\left[\left(\widetilde{T}_{ji} - \widetilde{R}_{ji}\right) + \sum_{k}{}'\left(2\,\widetilde{V}_{jkik} - \widetilde{V}_{jkki}\right)\right] -\\
&-\sum_{i}{}'\sum_{j} 2\,\widetilde{\Delta}_{ij}\left[\left(\widetilde{T}_{ji} - \widetilde{R}_{ji}\right) + \sum_{k}{}'\left(2\,\widetilde{V}_{jkik} - \widetilde{V}_{jkki}\right)\right] = 0.
\end{aligned} \tag{5.39}$$

Let us now introduce the (closed-shell) *Fock operator* [89, 90],

$$\hat{F} = \hat{T} + \sum_{k}{}'\left(2\,\hat{J}_k - \hat{K}_k\right), \tag{5.40}$$

where $\hat{J}_k$ and $\hat{K}_k$ are *Coulomb* and *exchange* operators [89, 90], already encountered in the previous chapter. Clearly, we have

$$\widetilde{F}_{ji} = \langle\phi_j|\,\hat{F}\,|\phi_i\rangle = \widetilde{T}_{ji} + \sum_{k}{}'\left(2\,\widetilde{V}_{jkik} - \widetilde{V}_{jkki}\right), \tag{5.41}$$

and thus the variational equation can be rewritten as

$$\sum_{i}\sum_{j}{}' 2\,\widetilde{\Delta}_{ij}\left(\widetilde{F}_{ji} - \widetilde{R}_{ji}\right) - \sum_{i}{}'\sum_{j} 2\,\widetilde{\Delta}_{ij}\left(\widetilde{F}_{ji} - \widetilde{R}_{ji}\right) = 0. \tag{5.42}$$

Introducing the occupation numbers,

$$n_i = \begin{cases} 2 & \text{if } \phi_i \text{ is doubly occupied} \\ 0 & \text{otherwise} \end{cases}, \tag{5.43}$$

it is possible to gather the two terms in equation (5.42):

$$\sum_{i,j} \widetilde{\Delta}_{ij} \left[n_j \left(\widetilde{F}_{ji} - \widetilde{R}_{ji} \right) - n_i \left(\widetilde{F}_{ji} - \widetilde{R}_{ji} \right) \right] = 0, \tag{5.44}$$

i.e.,

$$\sum_{i,j} \widetilde{\Delta}_{ij} \left(n_j - n_i \right) \langle \phi_j | \hat{F} - \hat{R} | \phi_i \rangle = 0. \tag{5.45}$$

Hence, the choice $\hat{R} = \hat{F}$ satisfies the Dirac-Frenkel variational principle, and the optimal equations of motion for the spatial part of the single-particle orbitals read

$$\mathrm{i}\hbar \, |\dot{\phi}_i\rangle = \hat{F} \, |\phi_i\rangle, \tag{5.46}$$

as expected (this is the usual *time-dependent Hartree-Fock* result [90]). Notice that, in analogy with the time-independent case, there is a certain degree of arbitrariness in this choice of the effective single-particle operator $\hat{R}$, since equation (5.45) is automatically satisfied when $n_i = n_j$. Thus, the relevant matrix elements are those connecting the occupied and virtual subspaces, for which the choice of $\hat{R}$ is unique.

5.2.4 Application to an open-shell singlet state

Let us now consider the case of an *open-shell singlet* state and a *spin-independent* Hamiltonian. The spin symmetry arguments of the single-configurational case can still be invoked, and thus relations (5.34) through (5.36) remain valid. In this case, the wavefunction is the sum of *two* Slater determinants,

$$\begin{aligned} |\Psi\rangle &= \frac{1}{\sqrt{2}} \, |\phi_1 \, \bar{\phi}_1 \, \cdots \, \phi_{n-1} \, \bar{\phi}_{n-1} \, \phi_v \, \bar{\phi}_c\rangle + \frac{1}{\sqrt{2}} \, |\phi_1 \, \bar{\phi}_1 \, \cdots \, \phi_{n-1} \, \bar{\phi}_{n-1} \, \phi_c \, \bar{\phi}_v\rangle \\ &\equiv \frac{1}{\sqrt{2}} \left(|\Phi_1\rangle + |\Phi_2\rangle \right), \end{aligned} \tag{5.47}$$

corresponding to a singlet arrangement of a set of $n-1$ doubly occupied orbitals and two singly occupied orbitals, labelled 'v' and 'c'. As before, the elements of the

one-body reduced density matrix are trivial:

$$\rho^{(1)}_{i\sigma_i,j\sigma_j} = \frac{n_i}{2}\,\delta_{ij}\,\delta_{\sigma_i\sigma_j}, \tag{5.48}$$

with the populations

$$n_i = \begin{cases} 2 & \text{if } \phi_i \text{ is doubly occupied} \\ 1 & \text{if } \phi_i \text{ is singly occupied} \\ 0 & \text{otherwise} \end{cases} . \tag{5.49}$$

However, the two-body reduced density matrix possesses a more involved structure, which we will describe briefly. When all the indices refer to occupied orbitals, its elements can be written as the sum of two terms (we recall that they are zero otherwise):

$$\rho^{(2)}_{i\sigma_i j\sigma_j,k\sigma_k l\sigma_l} = \frac{1}{2}\left(\gamma_{i\sigma_i j\sigma_j,k\sigma_k l\sigma_l} + \zeta_{i\sigma_i j\sigma_j,k\sigma_k l\sigma_l}\right). \tag{5.50}$$

The first one, given by

$$\begin{aligned} \gamma_{i\sigma_i j\sigma_j,k\sigma_k l\sigma_l} = {} & \left(\delta_{il}\,\delta_{jk}\,\delta_{\sigma_i\sigma_l}\,\delta_{\sigma_j\sigma_k} - \delta_{ik}\,\delta_{jl}\,\delta_{\sigma_i\sigma_k}\,\delta_{\sigma_j\sigma_l}\right) \times \\ & \times\Big[\left(1-\delta_{iv}\,\delta_{\sigma_i\downarrow}-\delta_{jv}\,\delta_{\sigma_j\downarrow}\right)\left(1-\delta_{ic}\,\delta_{\sigma_i\uparrow}-\delta_{jc}\,\delta_{\sigma_j\uparrow}\right) + \\ & \quad + \left(1-\delta_{iv}\,\delta_{\sigma_i\uparrow}-\delta_{jv}\,\delta_{\sigma_j\uparrow}\right)\left(1-\delta_{ic}\,\delta_{\sigma_i\downarrow}-\delta_{jc}\,\delta_{\sigma_j\downarrow}\right)\Big], \end{aligned} \tag{5.51}$$

arises from contributions, such as $\langle\Phi_1|\,\hat{c}^\dagger_{i\sigma_i}\,\hat{c}^\dagger_{j\sigma_j}\,\hat{c}_{k\sigma_k}\,\hat{c}_{l\sigma_l}|\Phi_1\rangle$, which are only nonzero when we annihilate and create the same pair of orbitals. Since each configuration is "missing" two states ($\bar{\phi}_v$, ϕ_c are not included in Φ_1, and ϕ_v, $\bar{\phi}_c$ are not included in Φ_2), some combinations of indices referring to occupied orbitals only give a partial contribution to the total matrix element, via $\langle\Phi_1|\,\hat{c}^\dagger_{i\sigma_i}\,\hat{c}^\dagger_{j\sigma_j}\,\hat{c}_{k\sigma_k}\,\hat{c}_{l\sigma_l}|\Phi_1\rangle$ or $\langle\Phi_2|\,\hat{c}^\dagger_{i\sigma_i}\,\hat{c}^\dagger_{j\sigma_j}\,\hat{c}_{k\sigma_k}\,\hat{c}_{l\sigma_l}|\Phi_2\rangle$ (but not both). In equation (5.51), this is accounted for by the term in square brackets. The second contribution is given by

$$\begin{aligned} \zeta_{i\sigma_i j\sigma_j,k\sigma_k l\sigma_l} = {} & \delta_{iv}\,\delta_{jc}\,\delta_{\sigma_i\uparrow}\,\delta_{\sigma_j\downarrow}\left(\delta_{kv}\,\delta_{lc}\,\delta_{\sigma_k\downarrow}\,\delta_{\sigma_l\uparrow} - \delta_{kc}\,\delta_{lv}\,\delta_{\sigma_k\uparrow}\,\delta_{\sigma_l\downarrow}\right) + \\ & + \delta_{ic}\,\delta_{jv}\,\delta_{\sigma_i\downarrow}\,\delta_{\sigma_j\uparrow}\left(\delta_{kc}\,\delta_{lv}\,\delta_{\sigma_k\uparrow}\,\delta_{\sigma_l\downarrow} - \delta_{kv}\,\delta_{lc}\,\delta_{\sigma_k\downarrow}\,\delta_{\sigma_l\uparrow}\right) + \\ & + \delta_{ic}\,\delta_{jv}\,\delta_{\sigma_i\uparrow}\,\delta_{\sigma_j\downarrow}\left(\delta_{kc}\,\delta_{lv}\,\delta_{\sigma_k\downarrow}\,\delta_{\sigma_l\uparrow} - \delta_{kv}\,\delta_{lc}\,\delta_{\sigma_k\uparrow}\,\delta_{\sigma_l\downarrow}\right) + \\ & + \delta_{iv}\,\delta_{jc}\,\delta_{\sigma_i\downarrow}\,\delta_{\sigma_j\uparrow}\left(\delta_{kv}\,\delta_{lc}\,\delta_{\sigma_k\uparrow}\,\delta_{\sigma_l\downarrow} - \delta_{kc}\,\delta_{lv}\,\delta_{\sigma_k\downarrow}\,\delta_{\sigma_l\uparrow}\right), \end{aligned} \tag{5.52}$$

and arises from the cross terms $\langle\Phi_1|\,\hat{c}^\dagger_{i\sigma_i}\,\hat{c}^\dagger_{j\sigma_j}\,\hat{c}_{k\sigma_k}\,\hat{c}_{l\sigma_l}\,|\Phi_2\rangle$ and $\langle\Phi_2|\,\hat{c}^\dagger_{i\sigma_i}\,\hat{c}^\dagger_{j\sigma_j}\,\hat{c}_{k\sigma_k}\,\hat{c}_{l\sigma_l}\,|\Phi_1\rangle$. Since the configurations included in the wavefunction differ in two orbitals, namely the singly occupied ones, these terms are only nonzero when we annihilate the singly occupied states that appear in one configuration and create the respective states included in the other. Equation (5.52) expresses all the allowed ways in which we can accomplish this.

With these results, the variational equation (5.28) reads

$$
\begin{aligned}
&\sum_{i,j,\sigma_i,\sigma_j} \Delta_{i\sigma_i,j\sigma_j}\left[\frac{n_j}{2}\left(T_{j\sigma_j,i\sigma_i}-R_{j\sigma_j,i\sigma_i}\right)-\frac{n_i}{2}\left(T_{j\sigma_j,i\sigma_i}-R_{j\sigma_j,i\sigma_i}\right)\right]+\\
&+\sum_{i,\sigma_i}\sum_{j,\sigma_j}{}''' \Delta_{i\sigma_i,j\sigma_j}\left[\sum_{k,\sigma_k}\frac{n_k}{2}\left(V_{j\sigma_j k\sigma_k,i\sigma_i k\sigma_k}-V_{j\sigma_j k\sigma_k,k\sigma_k i\sigma_i}\right)\right]-\\
&-\sum_{i,\sigma_i}{}'''\sum_{j,\sigma_j}\Delta_{i\sigma_i,j\sigma_j}\left[\sum_{k,\sigma_k}\frac{n_k}{2}\left(V_{j\sigma_j k\sigma_k,i\sigma_i k\sigma_k}-V_{j\sigma_j k\sigma_k,k\sigma_k i\sigma_i}\right)\right]-\\
&-\frac{1}{2}\sum_{i,\sigma_i}\sum_{j,\sigma_j}{}' \Delta_{i\sigma_i,j\sigma_j}\left[\sum_{k,\sigma_k}{}'''\left(V_{j\sigma_j k\sigma_k,i\sigma_i k\sigma_k}-V_{j\sigma_j k\sigma_k,k\sigma_k i\sigma_i}\right)\right]+\\
&+\frac{1}{2}\sum_{i,\sigma_i}{}'\sum_{j,\sigma_j}\Delta_{i\sigma_i,j\sigma_j}\left[\sum_{k,\sigma_k}{}'''\left(V_{j\sigma_j k\sigma_k,i\sigma_i k\sigma_k}-V_{j\sigma_j k\sigma_k,k\sigma_k i\sigma_i}\right)\right]+\\
&+\frac{1}{2}\sum_{i,\sigma_i}\Big[\Delta_{i\sigma_i,v\uparrow}\left(V_{v\uparrow c\downarrow,i\sigma_i c\downarrow}-V_{c\downarrow v\uparrow,i\sigma_i c\downarrow}+V_{c\uparrow v\downarrow,i\sigma_i c\downarrow}-V_{v\downarrow c\uparrow,i\sigma_i c\downarrow}\right)+\\
&\qquad+\Delta_{i\sigma_i,v\downarrow}\left(V_{v\downarrow c\uparrow,i\sigma_i c\uparrow}-V_{c\uparrow v\downarrow,i\sigma_i c\uparrow}+V_{c\downarrow v\uparrow,i\sigma_i c\uparrow}-V_{v\uparrow c\downarrow,i\sigma_i c\uparrow}\right)+\\
&\qquad+\Delta_{i\sigma_i,c\uparrow}\left(V_{c\uparrow v\downarrow,i\sigma_i v\downarrow}-V_{v\downarrow c\uparrow,i\sigma_i v\downarrow}+V_{v\uparrow c\downarrow,i\sigma_i v\downarrow}-V_{c\downarrow v\uparrow,i\sigma_i v\downarrow}\right)+\\
&\qquad+\Delta_{i\sigma_i,c\downarrow}\left(V_{c\downarrow v\uparrow,i\sigma_i v\uparrow}-V_{v\uparrow c\downarrow,i\sigma_i v\uparrow}+V_{v\downarrow c\uparrow,i\sigma_i v\uparrow}-V_{c\uparrow v\downarrow,i\sigma_i v\uparrow}\right)\Big]-\\
&-\frac{1}{2}\sum_{j,\sigma_j}\Big[\Delta_{v\uparrow,j\sigma_j}\left(V_{j\sigma_j c\downarrow,v\uparrow c\downarrow}-V_{j\sigma_j c\downarrow,c\downarrow v\uparrow}+V_{j\sigma_j c\downarrow,c\uparrow v\downarrow}-V_{j\sigma_j c\downarrow,v\downarrow c\uparrow}\right)+\\
&\qquad+\Delta_{v\downarrow,j\sigma_j}\left(V_{j\sigma_j c\uparrow,v\downarrow c\uparrow}-V_{j\sigma_j c\uparrow,c\uparrow v\downarrow}+V_{j\sigma_j c\uparrow,c\downarrow v\uparrow}-V_{j\sigma_j c\uparrow,v\uparrow c\downarrow}\right)+\\
&\qquad+\Delta_{c\uparrow,j\sigma_j}\left(V_{j\sigma_j v\downarrow,c\uparrow v\downarrow}-V_{j\sigma_j v\downarrow,v\downarrow c\uparrow}+V_{j\sigma_j v\downarrow,v\uparrow c\downarrow}-V_{j\sigma_j v\downarrow,c\downarrow v\uparrow}\right)+\\
&\qquad+\Delta_{c\downarrow,j\sigma_j}\left(V_{j\sigma_j v\uparrow,c\downarrow v\uparrow}-V_{j\sigma_j v\uparrow,v\uparrow c\downarrow}+V_{j\sigma_j v\uparrow,v\downarrow c\uparrow}-V_{j\sigma_j v\uparrow,c\uparrow v\downarrow}\right)\Big]=0,
\end{aligned}
\tag{5.53}
$$

where the symbol $\sum'''$ means that the sum runs over both doubly and singly occupied molecular orbitals (but not empty ones), and $\sum'$ is used for sums which extend only over singly occupied orbitals. Using the identities (5.34) and (5.35) to

perform the summations over spin, yields

$$
\begin{aligned}
&\sum_{i,j} \widetilde{\Delta}_{ij} \left[n_j \left(\widetilde{T}_{ji} - \widetilde{R}_{ji} \right) - n_i \left(\widetilde{T}_{ji} - \widetilde{R}_{ji} \right) \right] + \\
&+ \sum_i \sum_j{}''' \widetilde{\Delta}_{ij} \sum_k n_k \left(2\, \widetilde{V}_{jkik} - \widetilde{V}_{jkki} \right) - \\
&- \sum_i{}''' \sum_j \widetilde{\Delta}_{ij} \sum_k n_k \left(2\, \widetilde{V}_{jkik} - \widetilde{V}_{jkki} \right) - \\
&- \sum_i \sum_j{}' \widetilde{\Delta}_{ij} \sum_k{}''' \left(2\, \widetilde{V}_{jkik} - \widetilde{V}_{jkki} \right) + \\
&+ \sum_i{}' \sum_j \widetilde{\Delta}_{ij} \sum_k{}''' \left(2\, \widetilde{V}_{jkik} - \widetilde{V}_{jkki} \right) + \\
&+ \sum_i \left[\widetilde{\Delta}_{iv} \left(\widetilde{V}_{vcic} + \widetilde{V}_{vcci} \right) + \widetilde{\Delta}_{ic} \left(\widetilde{V}_{cviv} + \widetilde{V}_{cvvi} \right) \right] - \\
&- \sum_j \left[\widetilde{\Delta}_{vj} \left(\widetilde{V}_{jcvc} + \widetilde{V}_{jccv} \right) + \widetilde{\Delta}_{cj} \left(\widetilde{V}_{jvcv} + \widetilde{V}_{jvvc} \right) \right] = 0.
\end{aligned}
\tag{5.54}
$$

Explicitly separating the sums that run over all occupied states into contributions from orbitals with double and single occupancies, and collecting similar terms, we obtain

$$
\begin{aligned}
&\sum_{i,j} \widetilde{\Delta}_{ij} \left[n_j \left(\widetilde{T}_{ji} - \widetilde{R}_{ji} \right) - n_i \left(\widetilde{T}_{ji} - \widetilde{R}_{ji} \right) \right] + \\
&+ \sum_i \Bigg\{ \sum_j{}'' \widetilde{\Delta}_{ij} \sum_k n_k \left(2\, \widetilde{V}_{jkik} - \widetilde{V}_{jkki} \right) + \\
&\qquad + \sum_j{}' \widetilde{\Delta}_{ij} \Bigg[\sum_k{}'' \left(2\, \widetilde{V}_{jkik} - \widetilde{V}_{jkki} \right) + \\
&\qquad + \sum_k{}' \left(\widetilde{V}_{jkik} + \widetilde{V}_{jkki} \right) \left(1 - \delta_{jk} \right) \Bigg] \Bigg\} - \\
&- \sum_j \Bigg\{ \sum_i{}'' \widetilde{\Delta}_{ij} \sum_k n_k \left(2\, \widetilde{V}_{jkik} - \widetilde{V}_{jkki} \right) + \\
&\qquad + \sum_i{}' \widetilde{\Delta}_{ij} \Bigg[\sum_k{}'' \left(2\, \widetilde{V}_{jkik} - \widetilde{V}_{jkki} \right) + \\
&\qquad + \sum_k{}' \left(\widetilde{V}_{jkik} + \widetilde{V}_{jkki} \right) \left(1 - \delta_{ik} \right) \Bigg] \Bigg\} = 0,
\end{aligned}
\tag{5.55}
$$

where the symbol $\sum''$ means that the sum extends only over doubly occupied

molecular orbitals. Equivalently,

$$
\begin{aligned}
&\sum_{i,j} \widetilde{\Delta}_{ij} \left[n_j \left(\widetilde{T}_{ji} - \widetilde{R}_{ji} \right) - n_i \left(\widetilde{T}_{ji} - \widetilde{R}_{ji} \right) \right] + \\
&+ \sum_i \Bigg\{ \sum_j{}'' \, \widetilde{\Delta}_{ij} \, n_j \left[\frac{1}{2} \sum_k n_k \left(2\, \widetilde{V}_{jkik} - \widetilde{V}_{jkki} \right) \right] + \\
&\qquad + \sum_j{}' \, \widetilde{\Delta}_{ij} \, n_j \left[\frac{1}{2} \sum_k{}'' \, n_k \left(2\, \widetilde{V}_{jkik} - \widetilde{V}_{jkki} \right) + \right. \\
&\qquad \left. + \frac{1}{2} \sum_k{}' \, n_k \left(2\, \widetilde{V}_{jkik} + 2\, \widetilde{V}_{jkki} \right) \left(1 - \delta_{jk} \right) \right] \Bigg\} - \\
&- \sum_j \Bigg\{ \sum_i{}'' \, \widetilde{\Delta}_{ij} \, n_i \left[\frac{1}{2} \sum_k n_k \left(2\, \widetilde{V}_{jkik} - \widetilde{V}_{jkki} \right) \right] + \\
&\qquad + \sum_i{}' \, \widetilde{\Delta}_{ij} \, n_i \left[\frac{1}{2} \sum_k{}'' \, n_k \left(2\, \widetilde{V}_{jkik} - \widetilde{V}_{jkki} \right) + \right. \\
&\qquad \left. + \frac{1}{2} \sum_k{}' \, n_k \left(2\, \widetilde{V}_{jkik} + 2\, \widetilde{V}_{jkki} \right) \left(1 - \delta_{ik} \right) \right] \Bigg\} = 0,
\end{aligned}
\tag{5.56}
$$

where we have conveniently introduced some occupation numbers.

It is clear from the form of equation (5.56) the emergence of *Fock-like operators* which depend on the orbital occupation, in contrast with the case of a single Slater determinant. Specifically, all the doubly occupied orbitals possess the same Fock operator, whereas each singly occupied orbital has its own. Gathering groups of orbitals with the same Fock operator in a *shell*, labelled by μ, ν, ..., we can rewrite equation (5.56) as

$$
\sum_{\mu,\nu} \sum_{i_\mu, j_\nu} \widetilde{\Delta}_{i_\mu j_\nu} \left\langle \phi_{j_\nu} \right| n^\nu \hat{F}^\nu - n^\mu \hat{F}^\mu - \left(n^\nu - n^\mu \right) \hat{R} \left| \phi_{i_\mu} \right\rangle = 0, \tag{5.57}
$$

where i_μ runs over orbitals of shell μ, $n^\mu = 0, 1, 2$ denotes the occupation number of an orbital in shell μ, and the Fock operator for shell μ ($\mu \neq 0$) is given by

$$
\hat{F}^\mu = \hat{T} + \frac{1}{2} \sum_\nu \sum_{j_\nu} n^\nu \left(2\, \hat{J}_{j_\nu} - b^{\mu\nu} \hat{K}_{j_\nu} \right), \tag{5.58}
$$

with

$$
\mathbf{b} = \begin{pmatrix} 1 & 1 & 1 \\ 1 & 2 & -2 \\ 1 & -2 & 2 \end{pmatrix}, \tag{5.59}
$$

where we adopted the conventional ordering [94–96], in which $\mu = 1$ labels the doubly occupied shell, and $\mu = 2, 3$ refer to the singly occupied ones. Notice that we also consider the subspace of unoccupied orbitals as a proper shell (labelled by $\mu = 0$), even though its Fock operator is undefined (this is, however, irrelevant since it is always premultiplied by zero), and therefore this shell is not included in the definition of $\mathbf{b}$ given above.

From (5.57), we can see that mixing orbitals that belong to the same shell does not lead to any change in the variational quantity, and thus the terms with $\mu = \nu$ can be safely disregarded. Equivalently, as already encountered in the single-configurational case, there is a *gauge freedom* to choose the matrix elements of $\hat{R}$ within the subspaces spanned by each shell. For simplicity, these will be set to zero. Additionally, the contributions which arise from mixing orbitals of different shells, but with the same occupation number, in general differ from zero regardless of the choice of the operator $\hat{R}$. Hence, the corresponding orbital rotation parameters must be set to zero in order to satisfy the variational principle. This is consistent with neglecting two-electron processes which change the shell structure, and can only be described using a formalism with time-dependent expansion coefficients.

With the above considerations, the variational equation reduces to

$$\sum_{\substack{\mu,\nu \\ (n^\mu \neq n^\nu)}} \sum_{i_\mu, j_\nu} \widetilde{\Delta}_{i_\mu j_\nu} \langle \phi_{j_\nu} | \, n^\nu \hat{F}^\nu - n^\mu \hat{F}^\mu - (n^\nu - n^\mu) \, \hat{R} \, | \phi_{i_\mu} \rangle = 0, \tag{5.60}$$

which suggests that we set

$$\hat{R} = \sum_{\substack{\mu,\nu \\ (n^\mu \neq n^\nu)}} \hat{P}^\nu \, \frac{n^\nu \hat{F}^\nu - n^\mu \hat{F}^\mu}{n^\nu - n^\mu} \, \hat{P}^\mu, \tag{5.61}$$

where $\hat{P}^\mu$ is a projector onto the subspace spanned by shell μ:

$$\hat{P}^\mu = \sum_{i_\mu} |\phi_{i_\mu}\rangle\langle\phi_{i_\mu}|. \tag{5.62}$$

Clearly, this choice satisfies the Dirac-Frenkel variational principle. The optimal equations of motion for the spatial part of the single-particle orbitals thus read

$$\mathrm{i}\hbar \, |\dot{\phi}_{i_\mu}\rangle = \sum_{\substack{\nu,\lambda \\ (n^\nu \neq n^\lambda)}} \hat{P}^\lambda \, \frac{n^\lambda \hat{F}^\lambda - n^\nu \hat{F}^\nu}{n^\lambda - n^\nu} \, \hat{P}^\nu \, |\phi_{i_\mu}\rangle. \tag{5.63}$$

5.2.5 Application to general open-shell states

We now turn to *general open-shell states*, within a spin-restricted formalism. These are characterised by the one- and two-body reduced density matrices

$$\begin{aligned}
\rho^{(1)}_{i_\mu\sigma_{i_\mu},j_\nu\sigma_{j_\nu}} &= \frac{n^\mu}{2}\,\delta_{i_\mu j_\nu}\,\delta_{\sigma_{i_\mu}\sigma_{j_\nu}}, \\
\rho^{(2)}_{i_\mu\sigma_{i_\mu}j_\nu\sigma_{j_\nu},k_\lambda\sigma_{k_\lambda}l_\kappa\sigma_{l_\kappa}} &= \frac{n^\mu\,n^\nu}{12}\Big[\big(4\,a^{\mu\nu}-b^{\mu\nu}\big)\big(\delta_{i_\mu l_\kappa}\,\delta_{j_\nu k_\lambda}\,\delta_{\sigma_{i_\mu}\sigma_{l_\kappa}}\delta_{\sigma_{j_\nu}\sigma_{k_\lambda}} - \\
&\qquad - \delta_{i_\mu k_\lambda}\,\delta_{j_\nu l_\kappa}\,\delta_{\sigma_{i_\mu}\sigma_{k_\lambda}}\delta_{\sigma_{j_\nu}\sigma_{l_\kappa}}\big) + \\
&\qquad + 2\,\big(a^{\mu\nu}-b^{\mu\nu}\big)\big(\delta_{i_\mu k_\lambda}\,\delta_{j_\nu l_\kappa}\,\delta_{\sigma_{i_\mu}\sigma_{l_\kappa}}\delta_{\sigma_{j_\nu}\sigma_{k_\lambda}} - \\
&\qquad - \delta_{i_\mu l_\kappa}\,\delta_{j_\nu k_\lambda}\,\delta_{\sigma_{i_\mu}\sigma_{k_\lambda}}\delta_{\sigma_{j_\nu}\sigma_{l_\kappa}}\big)\Big],
\end{aligned} \tag{5.64}$$

where, as discussed in the previous chapter, the *state parameters*

$$\begin{aligned}
a^{\mu\nu} &= a^{\nu\mu}, \\
b^{\mu\nu} &= b^{\nu\mu}
\end{aligned} \tag{5.65}$$

depend on the particular form of the wavefunction [94–96], which in general is a sum of many Slater determinants. Equation (5.64) leads to the energy expression

$$E = \sum_\mu \sum_{i_\mu} n^\mu\,\widetilde{T}_{i_\mu i_\mu} + \frac{1}{4}\sum_{\mu,\nu}\sum_{i_\mu,j_\nu} n^\mu\,n^\nu\big(2\,a^{\mu\nu}\,\widetilde{J}_{i_\mu j_\nu} - b^{\mu\nu}\,\widetilde{K}_{i_\mu j_\nu}\big), \tag{5.66}$$

which is the more familiar way to define a general open-shell state [94–96]. Notice that the closed-shell and open-shell singlet states of the previous sections are special cases of this broad definition. For a closed-shell singlet state there is only one occupied shell, and the state parameters read $a = b = 1$. As we have already seen, in the case of an open-shell singlet state there are three shells, $\mathbf{b}$ is given by (5.59), and

$$\mathbf{a} = \begin{pmatrix} 1 & 1 & 1 \\ 1 & 1 & 1 \\ 1 & 1 & 1 \end{pmatrix}. \tag{5.67}$$

As discussed in the previous chapter, many other important electronic states of atoms and molecules fall into this category. Most notably, it includes all possible spin-adapted states that can be obtained from a specific electronic configuration [94–96].

To derive the optimal equations of motion for the single-particle orbitals, we now proceed as in the previous sections. Inserting (5.64) into the variational equation (5.28), yields

$$\begin{aligned}
&\sum_{\mu,\nu}\sum_{i_\mu,j_\nu}\sum_{\sigma_{i_\mu},\sigma_{j_\nu}}\Delta_{i_\mu\sigma_{i_\mu},j_\nu\sigma_{j_\nu}}\Bigg\{\frac{n^\nu-n^\mu}{2}\left(T_{j_\nu\sigma_{j_\nu},i_\mu\sigma_{i_\mu}}-R_{j_\nu\sigma_{j_\nu},i_\mu\sigma_{i_\mu}}\right)+\\
&+n^\nu\sum_{\lambda,k_\lambda,\sigma_{k_\lambda}}\frac{n^\lambda}{12}\Big[\left(4\,a^{\nu\lambda}-b^{\nu\lambda}\right)\left(V_{j_\nu\sigma_{j_\nu}k_\lambda\sigma_{k_\lambda},i_\mu\sigma_{i_\mu}k_\lambda\sigma_{k_\lambda}}-V_{j_\nu\sigma_{j_\nu}k_\lambda\sigma_{k_\lambda},k_\lambda\sigma_{k_\lambda}i_\mu\sigma_{i_\mu}}\right)+\\
&\qquad+2\left(a^{\nu\lambda}-b^{\nu\lambda}\right)\left(V_{j_\nu\sigma_{k_\lambda}k_\lambda\sigma_{j_\nu},k_\lambda\sigma_{k_\lambda}i_\mu\sigma_{i_\mu}}-V_{j_\nu\sigma_{k_\lambda}k_\lambda\sigma_{j_\nu},i_\mu\sigma_{i_\mu}k_\lambda\sigma_{k_\lambda}}\right)\Big]-\\
&-n^\mu\sum_{\lambda,k_\lambda,\sigma_{k_\lambda}}\frac{n^\lambda}{12}\Big[\left(4\,a^{\mu\lambda}-b^{\mu\lambda}\right)\left(V_{j_\nu\sigma_{j_\nu}k_\lambda\sigma_{k_\lambda},i_\mu\sigma_{i_\mu}k_\lambda\sigma_{k_\lambda}}-V_{j_\nu\sigma_{j_\nu}k_\lambda\sigma_{k_\lambda},k_\lambda\sigma_{k_\lambda}i_\mu\sigma_{i_\mu}}\right)+\\
&\qquad+2\left(a^{\mu\lambda}-b^{\mu\lambda}\right)\left(V_{j_\nu\sigma_{j_\nu}k_\lambda\sigma_{k_\lambda},k_\lambda\sigma_{i_\mu}i_\mu\sigma_{k_\lambda}}-V_{j_\nu\sigma_{j_\nu}k_\lambda\sigma_{k_\lambda},i_\mu\sigma_{k_\lambda}k_\lambda\sigma_{i_\mu}}\right)\Big]\Bigg\}=0.
\end{aligned}\tag{5.68}$$

Summing over spin, with the help of relations (5.34) and (5.35), we obtain

$$\begin{aligned}
&\sum_{\mu,\nu}\sum_{i_\mu,j_\nu}\widetilde{\Delta}_{i_\mu j_\nu}\Bigg\{n^\nu\big(\widetilde{T}_{j_\nu i_\mu}-\widetilde{R}_{j_\nu i_\mu}\big)-n^\mu\big(\widetilde{T}_{j_\nu i_\mu}-\widetilde{R}_{j_\nu i_\mu}\big)+\\
&\qquad+n^\nu\left[\frac{1}{2}\sum_\lambda\sum_{k_\lambda}n^\lambda\big(2\,a^{\nu\lambda}\widetilde{V}_{j_\nu k_\lambda i_\mu k_\lambda}-b^{\nu\lambda}\widetilde{V}_{j_\nu k_\lambda k_\lambda i_\mu}\big)\right]-\\
&\qquad-n^\mu\left[\frac{1}{2}\sum_\lambda\sum_{k_\lambda}n^\lambda\big(2\,a^{\mu\lambda}\widetilde{V}_{j_\nu k_\lambda i_\mu k_\lambda}-b^{\mu\lambda}\widetilde{V}_{j_\nu k_\lambda k_\lambda i_\mu}\big)\right]\Bigg\}=0,
\end{aligned}\tag{5.69}$$

i.e.,

$$\sum_{\mu,\nu}\sum_{i_\mu,j_\nu}\widetilde{\Delta}_{i_\mu j_\nu}\left\langle\phi_{j_\nu}\right|n^\nu\hat{F}^\nu-n^\mu\hat{F}^\mu-\left(n^\nu-n^\mu\right)\hat{R}\left|\phi_{i_\mu}\right\rangle=0,\tag{5.70}$$

where the Fock operator for shell μ ($\mu\neq 0$) takes the generalised form

$$\hat{F}^\mu=\hat{T}+\frac{1}{2}\sum_\nu\sum_{j_\nu}n^\nu\big(2\,a^{\mu\nu}\hat{J}_{j_\nu}-b^{\mu\nu}\hat{K}_{j_\nu}\big).\tag{5.71}$$

As before, in order to satisfy the Dirac-Frenkel variational principle it is necessary to zero the mixing parameters between orbitals of different shells, but with the same occupation number. Also, the terms with $\mu=\nu$ may be ignored, as they do not change the variational quantity (again, we will use this gauge freedom to set the matrix elements of $\hat{R}$ within each shell subspace to zero). We are, thus, lead to the

choice

$$\hat{R} = \sum_{\substack{\mu,\nu \\ (n^\mu \neq n^\nu)}} \hat{P}^\nu \, \frac{n^\nu \hat{F}^\nu - n^\mu \hat{F}^\mu}{n^\nu - n^\mu} \, \hat{P}^\mu, \tag{5.72}$$

and the optimal equations of motion for the spatial part of the single-particle orbitals have the form of equation (5.63), with the Fock operators given by (5.71).

5.2.6 Computational cost

We conclude this chapter with a discussion of the cost of the numerical implementation of the proposed scheme. In all the applications we envisage, the number of occupied shells, N_{shells}, will be fixed by the spin symmetry, independent of system size, and in addition will be much lower than the size of the basis set, N_{basis}. This is typically the case when only a few configurations are included in the wavefunction expansion, e.g., for an open-shell singlet state. In such a case, the computational bottleneck lies in the calculation of the two-electron Coulomb and exchange terms required to build the matrix form of the Fock operators, exactly as in the time-dependent Hartree-Fock method. The formal scaling is $N_{\text{shells}} N_{\text{basis}}^4$, since the total number of two-electron integrals increases as N_{basis}^4 and N_{shells} different Fock operators must be constructed. If semiempirical parameters are used instead, the numerical effort can be more favourable, of the order of N_{basis}^3. In the limit of $N_{\text{shells}} \ll N_{\text{basis}}$, the proposed method requires only a few more matrix multiplications than the time-dependent Hartree-Fock method, and thus exhibits a comparable computational cost.

This has to be contrasted to the case of a *complete active space* expansion with *time-dependent* coefficients [120–124], for which the computational cost is exponential in the number of electrons, and thus quite rapidly becomes prohibitive as the number of degrees of freedom increases. In many processes of interest, the description of electron correlation effects does not require the level of accuracy inherent to a multiconfigurational method for a large wavefunction expansion with time-dependent coefficients, and the essential physics is well described in terms of simple spin-adapted states, for which the expansion coefficients can be regarded as time-

independent. In such cases, the method devised in the previous section for general open-shell states offers an attractive alternative. Strictly speaking, the description of several important two-electron processes, such as those governing exciton transfer between molecules [66], requires a formalism with time-dependent coefficients (although not necessarily a large number of configurations). Within the proposed scheme, this is only accounted for in a *mean-field* way. The advantage is, of course, that it is designed to treat the dynamics of excited electronic states at a computational cost comparable to that of the time-dependent Hartree-Fock method, thus allowing for the study of large systems of interacting electrons.

Part III

Applications

Chapter 6

Dynamics of photoexcitations in single *cis*-polyacetylene chains

6.1 Equations of motion

In this chapter, we investigate the effect of electron-electron interactions on the dynamics of low-lying excitations in single *cis*-polyacetylene chains. The formalism discussed in the previous chapter is applied to a linear chain with N sites and *fixed ends*, described by model Hamiltonians with and without Coulomb interactions. In general, we write

$$\begin{aligned}\hat{H} = &-\sum_{i,\sigma} t_i \left(\hat{c}^{\dagger}_{i\sigma}\,\hat{c}_{i+1,\sigma} + \hat{c}^{\dagger}_{i+1,\sigma}\,\hat{c}_{i\sigma}\right) + U\sum_i \left(\hat{n}_{i\uparrow} - \frac{1}{2}\right)\left(\hat{n}_{i\downarrow} - \frac{1}{2}\right) + \\ &+ \frac{1}{2}\sum_{i,j\neq i} v_{ij}\left(\hat{n}_i - 1\right)\left(\hat{n}_j - 1\right) + \frac{1}{2M}\sum_i p_i^2 + \frac{K}{2}\sum_i \left(u_{i+1} - u_i\right)^2,\end{aligned} \tag{6.1}$$

with

$$\begin{aligned}t_i &= t_0 - \alpha\left(u_{i+1} - u_i\right) + (-1)^{i+1}\, t_{\mathrm{e}}, \\ v_{ij} &= \frac{U}{\sqrt{1 + \left(\beta\, r_{ij}/r_0\right)^2}},\end{aligned} \tag{6.2}$$

which is just the SSH + PPP model, as defined by equation (3.25). If we set $U = 0$, this reduces to the SSH model (3.24).

The force on atom k, $k = 2, \ldots, N-1$ (we recall that atoms 1 and N are kept

fixed), is a sum of electronic and nuclear contributions:

$$F_k \equiv F_k^{(\mathrm{e})} + F_k^{(\mathrm{n})} = -\frac{\partial}{\partial u_k} V_\mathrm{e} - \frac{\partial}{\partial u_k} V_\mathrm{n}, \tag{6.3}$$

where V_e is the open-shell electronic energy, of the form (5.66), and

$$V_\mathrm{n} = \frac{K}{2} \sum_i (u_{i+1} - u_i)^2 + \frac{1}{2} \sum_{i,j \neq i} v_{ij}. \tag{6.4}$$

Let us consider the nuclear contribution first. We have

$$F_k^{(\mathrm{n})} = -K \sum_i (u_{i+1} - u_i) \frac{\partial}{\partial u_k} (u_{i+1} - u_i) - \frac{1}{2} \sum_{i,j \neq i} \frac{\partial v_{ij}}{\partial r_{ij}} \frac{\partial r_{ij}}{\partial u_k}. \tag{6.5}$$

The distance between sites i and j is given by

$$r_{ij} = |r_i - r_j| = \begin{cases} r_i - r_j & \text{if } i > j \\ r_j - r_i & \text{otherwise} \end{cases}, \tag{6.6}$$

where

$$r_i = (i-1)\, r_0 + u_i. \tag{6.7}$$

Hence, we find

$$\frac{\partial r_{ij}}{\partial u_k} = \begin{cases} \delta_{ik} - \delta_{jk} & \text{if } i > j \\ \delta_{jk} - \delta_{ik} & \text{otherwise} \end{cases}, \tag{6.8}$$

and the nuclear contribution to the force reads

$$\begin{aligned} F_k^{(\mathrm{n})} = & -K \sum_i (u_{i+1} - u_i) \left(\delta_{i+1,k} - \delta_{ik}\right) - \\ & - \frac{1}{2} \sum_i \left[\sum_{j<i} \frac{\partial v_{ij}}{\partial r_{ij}} \left(\delta_{ik} - \delta_{jk}\right) + \sum_{j>i} \frac{\partial v_{ij}}{\partial r_{ij}} \left(\delta_{jk} - \delta_{ik}\right) \right]. \end{aligned} \tag{6.9}$$

From (6.2), we obtain

$$\frac{\partial v_{ij}}{\partial r_{ij}} = -\frac{(\beta/r_0)^2\, r_{ij}}{1 + (\beta\, r_{ij}/r_0)^2}\, v_{ij}, \tag{6.10}$$

which leads to the final result

$$F_k^{(\mathrm{n})} = K\,(u_{k+1} + u_{k-1} - 2\,u_k) - \sum_i d_{ik}, \tag{6.11}$$

with

$$d_{ik} = \frac{(\beta/r_0)^2\,(r_i - r_k)}{1 + (\beta\, r_{ik}/r_0)^2}\, v_{ik}. \tag{6.12}$$

Let us now turn to the electronic contribution to the force. Writing the molecular orbitals, ϕ_{k_μ}, as a *superposition of atomic orbitals*, χ_i,

$$|\phi_{k_\mu}\rangle = \sum_i C_{ik_\mu} |\chi_i\rangle, \tag{6.13}$$

and making use of (3.17) and (3.18), we can recast the electronic energy for a general open-shell state in the form

$$\begin{aligned} V_{\rm e} = &- \sum_\mu \sum_i n^\mu \left[P^\mu_{ii} \left(\frac{U}{2} + \sum_{j\neq i} v_{ij} \right) + P^\mu_{i+1,i}\, t_i + P^\mu_{i-1,i}\, t_{i-1} \right] + \\ &+ \frac{1}{4} \sum_{\mu,\nu} \sum_{i,j} n^\mu\, n^\nu \left(2\, a^{\mu\nu} P^\mu_{ii}\, P^\nu_{jj} - b^{\mu\nu} P^\mu_{ji}\, P^\nu_{ij} \right) v_{ij}, \end{aligned} \tag{6.14}$$

where

$$P^\mu_{ij} = \sum_{k_\mu} C_{ik_\mu}\, C^*_{jk_\mu} \tag{6.15}$$

denotes an element of the projector onto shell μ, in the atomic orbitals basis set. In principle, the implicit dependence of the expansion coefficients on the lattice displacements should be taken into account when computing the gradient of (6.14). However, this may be safely disregarded, since for any real parameter, $x\,(t)$,

$$\langle \frac{\partial \Psi}{\partial x} |\, \hat{H}_{\rm e}\, | \Psi \rangle + \langle \Psi |\, \hat{H}_{\rm e}\, | \frac{\partial \Psi}{\partial x} \rangle = \frac{1}{\dot{x}} \left(\langle \dot{\Psi} |\, \hat{H}_{\rm e}\, | \Psi \rangle + \langle \Psi |\, \hat{H}_{\rm e}\, | \dot{\Psi} \rangle \right) = 0, \tag{6.16}$$

as it follows from the Dirac-Frenkel time-dependent variational principle (see section 5.2.2). Thus, we have

$$\boldsymbol{\nabla}_{\rm n} \langle \Psi |\, \hat{H}_{\rm e}\, | \Psi \rangle = \langle \Psi |\, \boldsymbol{\nabla}_{\rm n} \hat{H}_{\rm e}\, | \Psi \rangle, \tag{6.17}$$

which is analogous to the *Hellmann-Feynman theorem* [90]. Using the above expression, the electronic contribution to the force reads

$$\begin{aligned} F^{(\rm e)}_k = &\sum_\mu \sum_i n^\mu \left[P^\mu_{ii} \sum_{j\neq i} \frac{\partial v_{ij}}{\partial r_{ij}} \frac{\partial r_{ij}}{\partial u_k} + P^\mu_{i+1,i} \frac{\partial t_i}{\partial u_k} + P^\mu_{i-1,i} \frac{\partial t_{i-1}}{\partial u_k} \right] - \\ &- \frac{1}{4} \sum_{\mu,\nu} \sum_{i,j} n^\mu\, n^\nu \left(2\, a^{\mu\nu} P^\mu_{ii}\, P^\nu_{jj} - b^{\mu\nu} P^\mu_{ji}\, P^\nu_{ij} \right) \frac{\partial v_{ij}}{\partial r_{ij}} \frac{\partial r_{ij}}{\partial u_k}. \end{aligned} \tag{6.18}$$

From (6.2), we find

$$\frac{\partial t_i}{\partial u_k} = \alpha \left(\delta_{ik} - \delta_{i+1,k}\right), \tag{6.19}$$

which, together with the identities (6.8) and (6.10), leads to

$$\begin{aligned} F_k^{(\mathrm{e})} = & \sum_\mu n^\mu \left[\sum_i \left(P_{ii}^\mu + P_{kk}^\mu\right) d_{ik} + 2\,\alpha \left(\mathrm{Re}\, P_{k,k+1}^\mu - \mathrm{Re}\, P_{k,k-1}^\mu\right)\right] - \\ & - \frac{1}{2} \sum_{\mu,\nu} n^\mu\, n^\nu \sum_i \left[a^{\mu\nu} \left(P_{ii}^\mu\, P_{kk}^\nu + P_{kk}^\mu\, P_{ii}^\nu\right) - b^{\mu\nu}\, \mathrm{Re}\left(P_{ki}^\mu\, P_{ik}^\nu\right)\right] d_{ik}. \end{aligned} \tag{6.20}$$

Adding the contributions (6.11) and (6.20), we obtain for the total force:

$$\begin{aligned} F_k = & \sum_\mu n^\mu \left[\sum_i \left(P_{ii}^\mu + P_{kk}^\mu\right) d_{ik} + 2\,\alpha \left(\mathrm{Re}\, P_{k,k+1}^\mu - \mathrm{Re}\, P_{k,k-1}^\mu\right)\right] - \\ & - \frac{1}{2} \sum_{\mu,\nu} n^\mu\, n^\nu \sum_i \left[a^{\mu\nu} \left(P_{ii}^\mu\, P_{kk}^\nu + P_{kk}^\mu\, P_{ii}^\nu\right) - b^{\mu\nu}\, \mathrm{Re}\left(P_{ki}^\mu\, P_{ik}^\nu\right)\right] d_{ik} + \\ & + K\left(u_{k+1} + u_{k-1} - 2\,u_k\right) - \sum_i d_{ik}. \end{aligned} \tag{6.21}$$

Setting $U = 0$, yields the expression for the special case of the SSH model:

$$F_k = 2\,\alpha \left(\mathrm{Re}\, \rho_{k,k+1} - \mathrm{Re}\, \rho_{k,k-1}\right) + K\left(u_{k+1} + u_{k-1} - 2\,u_k\right), \tag{6.22}$$

where we have introduced the *density matrix* [90],

$$\rho_{ij} = \sum_\mu n^\mu P_{ij}^\mu = \sum_\mu \sum_{k_\mu} n^\mu\, C_{ik_\mu}\, C_{jk_\mu}^*. \tag{6.23}$$

In either case, the lattice displacements obey the equations of motion

$$M\,\ddot{u}_k = F_k, \tag{6.24}$$

for $k = 2, \ldots, N-1$.

As discussed in the previous chapter, the solution of the time-dependent wave equation for the electronic degrees of freedom, in the case of the SSH + PPP model, is provided by the multiconfigurational time-dependent Hartree-Fock approximation. Using (6.13), the optimal equations of motion (5.63) can be written in terms of the LCAO coefficients, C_{ik_μ}:

$$\mathrm{i}\,\hbar\,\dot{C}_{ik_\mu} = \sum_j R_{ij}\, C_{jk_\mu}, \tag{6.25}$$

with

$$R_{ij} = \sum_{\substack{\mu,\nu \\ (n^\mu \neq n^\nu)}} \sum_{k,l} P^\nu_{ik} \, \frac{n^\nu F^\nu_{kl} - n^\mu F^\mu_{kl}}{n^\nu - n^\mu} \, P^\mu_{lj}. \tag{6.26}$$

The *Fock matrix* for shell μ is expressed in the atomic orbitals basis set as

$$\begin{aligned} F^\mu_{ij} = &- \left[\frac{U}{2} + \sum_{k \neq i} v_{ik} \right] \delta_{ij} - t_i \, \delta_{i+1,j} - t_{i-1} \, \delta_{i-1,j} + \\ &+ \left[\sum_\nu \sum_k n^\nu \, a^{\mu\nu} P^\nu_{kk} \, v_{ik} \right] \delta_{ij} - \frac{1}{2} \sum_\nu n^\nu \, b^{\mu\nu} P^\nu_{ij} \, v_{ij}, \end{aligned} \tag{6.27}$$

where we have used (3.17) and (3.18).

In contrast, for the SSH model, equation (5.12) can be solved *exactly*, since the Hamiltonian only involves one-body operators. In this case, the equations of motion for the LCAO coefficients read [43]

$$\mathrm{i}\hbar \, \dot{C}_{ij_\mu} = -t_i \, C_{i+1,j_\mu} - t_{i-1} \, C_{i-1,j_\mu}. \tag{6.28}$$

In both cases, the resulting coupled sets of differential equations can be efficiently integrated numerically using, e.g., an *eighth-order Runge-Kutta* method with *adaptive step-size* control, due to Dormand and Prince [125].

It is also instructive to consider the presence of an *external electric field*, $f(t)$, which, in the *dipole approximation*, is assumed to be constant over the entire chain, thus coupling to the total dipole moment [50]:

$$\hat{H}'(t) = \hat{H} + \hat{H}_{\mathrm{ext}}(t), \tag{6.29}$$

with

$$\hat{H}_{\mathrm{ext}}(t) = e \, f(t) \sum_i r_i \, (\hat{n}_i - 1). \tag{6.30}$$

From (6.30), it is straightforward to include the field contribution on the force on atom k:

$$F'_k = F_k + e \, f(t) \, (1 - \rho_{kk}). \tag{6.31}$$

Moreover, since $\hat{H}_{\mathrm{ext}}(t)$ only contains one-body operators, the modifications to the equations of motion for the electronic degrees of freedom are also trivial. For the

SSH + PPP model, the Fock matrices are simply augmented with a diagonal term,

$$F_{ij}^{\mu\prime} = F_{ij}^{\mu} + e\, f\,(t)\, r_i\, \delta_{ij}, \tag{6.32}$$

while, for the SSH model, equation (6.28) is replaced by

$$\mathrm{i}\hbar\, \dot{C}_{ij_\mu} = -t_i\, C_{i+1,j_\mu} - t_{i-1}\, C_{i-1,j_\mu} + e\, f\,(t)\, r_i\, C_{ij_\mu}. \tag{6.33}$$

6.2 Model parameterisation

The various parameters used in the calculations are chosen so as to model *cis*-polyacetylene. This is typically accomplished through a *fitting procedure* aimed at reproducing certain experimentally observed quantities, such as the *optical gap*, $E_\mathrm{g} = 1.8$ eV, *band width*, $W = 10$ eV, and *ground state dimerisation*, $\delta = 0.05$ Å [44, 45]. For the special case of the SSH model, the best choice has been widely reported in the literature [43–45] (see table 6.1). However, when Coulomb interactions are included, the choice is less consensual [45, 126–128], which led us to perform our own parameterisation of the SSH + PPP model.

To this end, we first restricted the parameter space to the set $\{t_0, \alpha, U, \beta\}$, by keeping the remaining parameters fixed at their SSH values. The motivation behind this methodology is twofold. First, since the SSH and SSH + PPP models only

Table 6.1: Model parameters appropriate for cis*-polyacetylene.*

Parameter	SSH model	SSH + PPP model
r_0, Å	1.22	1.22
K, eV Å^{-2}	21	21
M, eV fs^2 Å^{-2}	1349.14	1349.14
α, eV Å^{-1}	4.1	3.2
t_0, eV	2.5	2.1
t_e, eV	0.05	0.05
U, eV	–	4.1
β	–	3.4

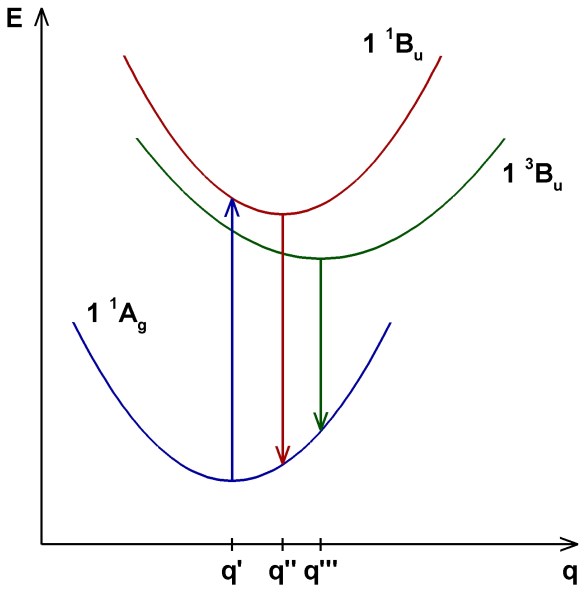

Figure 6.1: Schematic representation of the potential energy surfaces involved at each step of the iterative procedure developed for the parameterisation of the SSH + PPP model. The band width and dimerisation are computed at the ground state minimum, $E_{1^1A_g}(q')$, the optical gap is given by $E_g = E_{1^1B_u}(q') - E_{1^1A_g}(q')$, and the exciton singlet-triplet splitting is calculated as $\Delta = \left[E_{1^1B_u}(q'') - E_{1^1A_g}(q'')\right] - \left[E_{1^3B_u}(q''') - E_{1^1A_g}(q''')\right]$. Note that the coordinate sets q', q'', and q''' are found by geometry optimisation.

differ in their electronic parts, it is logical to take the same values for K and M in both cases. Second, we found that the effect of t_e on the investigated quantities is similar in both models, and thus it is reasonable to keep this parameter fixed. An initial guess for the varying parameters was then iteratively improved, using *Powell's direction set* method [91], until a good agreement between the predictions of both models for the optical gap, band width, and ground state dimerisation (for a given chain length) was reached. To avoid falling in the SSH minimum (i.e., $U = 0$), we also fitted the experimentally observed value for the *exciton singlet-triplet splitting*, $\Delta = 0.7$ eV [129], a quantity that is only nonzero when Coulomb interactions are included. As depicted in figure 6.1, each step of the iteration process requires the calculation of six points in some fairly complicated potential energy surfaces, which renders this approach computationally demanding. For this reason, we were only able to consider rather small chains, with $N = 40$ and 60. We found that the parameters listed in table 6.1 bring all the investigated quantities to within 10% of the

expected values. Although the parameters used throughout the calculations only apply to *cis*-polyacetylene, the results of the following sections should be qualitatively valid for other conjugated polymers with nondegenerate ground states.

6.3 Dynamics of the $1\,^1B_u$ photoexcited state

We now specialise to the case of a $1\,^1B_u$ photoexcited state. Initially, the ionic momenta are set to zero, and the displacements are chosen so as to minimise the *ground state* potential energy. This is achieved using the BFGS method [91]. Notice that the electronic subproblem requires a self-consistent field calculation to be performed at each iteration (for the SSH model, this is replaced by the diagonalisation of the Hamiltonian matrix). As discussed in chapter 4, we found that a *limited-memory* variant of the BFGS strategy [110] with *exact line searches*, based on an *exponential parameterisation* of the wavefunction [96], is appropriate for general open-shell states. A HOMO $\rightarrow$ LUMO excitation (or simply $1 \rightarrow 1$, in the notation in which the energy levels are counted downwards from the top of the valence band, and upwards from the bottom of the conduction band) is then set up, which requires an additional self-consistent field run in order to obtain the LCAO orbital coefficients at $t = 0$. In the special case of the SSH model, this only involves changing the orbital occupation numbers accordingly, since the single-particle wavefunctions take the same form as in the ground state. The initial conditions thus obtained are then propagated by numerical integration of the equations of motion, as discussed in section 6.1.

Figure 6.2 shows the time evolutions of the *staggered bond order parameter*, or *dimerisation* [43, 44],

$$\delta_i = \frac{(-1)^{i+1}}{4}\,(u_{i+1} + u_{i-1} - 2\,u_i), \tag{6.34}$$

calculated for a 200-site *cis*-polyacetylene chain, considering both the SSH and SSH + PPP models. As can be seen, the results are qualitatively similar, with the lattice relaxing to form a single local deformation in both cases. There is an almost periodic behaviour, with alternating peaks and troughs, which corresponds to a continuous

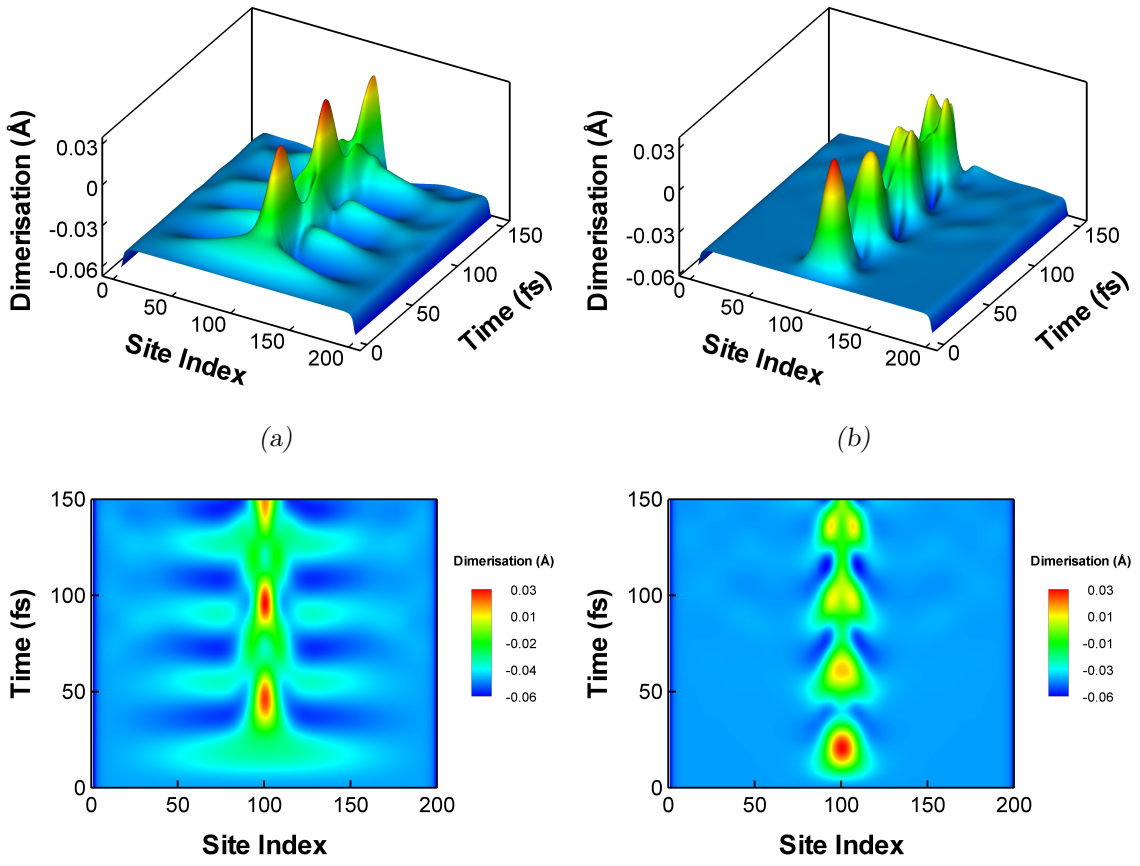

Figure 6.2: Side [(a) and (b)] and top [(c) and (d)] views of the time evolutions of the dimerisation pattern, obtained for a $1\,^1B_u$ photoexcited state in a 200-site cis-polyacetylene chain, considering the SSH [(a) and (c)] and SSH + PPP [(b) and (d)] models.

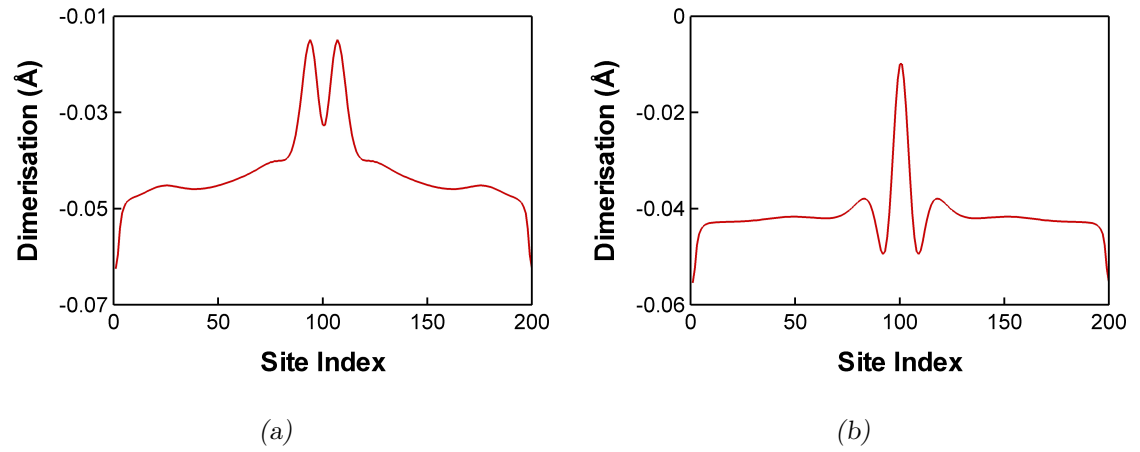

Figure 6.3: Snapshots of the dimerisation pattern at t = 120 fs (a valley region in figure 6.2), obtained for a $1\,^1B_u$ photoexcited state in a 200-site cis-polyacetylene chain, considering the SSH (a) and SSH + PPP (b) models.

interchange of the positions of the single and double bonds at the middle of the chain (i.e., an oscillation between the A and B phases). This is most extreme in the SSH case, for which the dimerisation pattern in the valley regions exhibits two small split peaks rather than a single one. In contrast, by including Coulomb interactions this dynamical process is somewhat suppressed, particularly at later times. Indeed, as shown more clearly in figure 6.3, the single peak profile is preserved, and the dimerisation at the centre of the chain is not as low. It is also clear from figure 6.2 that the elapsed time between peaks is shorter for the SSH + PPP model, suggesting that Coulomb interactions have the effect of promoting the creation of the local deformation. Moreover, while the peaks are of comparable width (at half maximum) for both models, they are accompanied by "tails" which extend over many more lattice sites in the SSH case. Hence, adding Coulomb interactions results in the formation of a more localised region of lattice distortion.

In order to gain further insight into the nature of the $1\,^1B_u$ photoexcited state, it is instructive to investigate the time evolution of the energies and occupation numbers for the instantaneous *adiabatic* single-particle orbitals, φ_i. Notice that the occupation numbers can vary, in contrast to the *time-evolving* orbitals, ϕ_{i_μ}. For the SSH model, this amounts to diagonalising the electronic part of the Hamiltonian at selected times, whereas, for the SSH + PPP model, it is necessary to minimise the electronic energy (6.14) through the self-consistent field procedure. In this case, we define the "orbital energies" as the matrix elements

$$\varepsilon_i = \begin{cases} \langle\varphi_i|\, 2\,\hat{F}^{(1)} - \frac{1}{2}\left(\hat{F}^{(2)} + \hat{F}^{(3)}\right)|\varphi_i\rangle & \text{for the valence band} \\ \langle\varphi_i|\, \frac{1}{2}\left(\hat{F}^{(2)} + \hat{F}^{(3)}\right)|\varphi_i\rangle & \text{for the conduction band} \end{cases}, \tag{6.35}$$

which are conveniently distributed symmetrically about the midgap, as discussed in chapter 4. Having found the instantaneous eigenstates, their occupation numbers can be calculated as [50]

$$p_i = \sum_\mu \sum_{j_\mu} n^\mu \left|\langle\varphi_i|\phi_{j_\mu}\rangle\right|^2. \tag{6.36}$$

Figure 6.4 shows the time evolutions of the energies of the instantaneous eigenfunctions near the band edges, calculated for a 200-site *cis*-polyacetylene chain, both

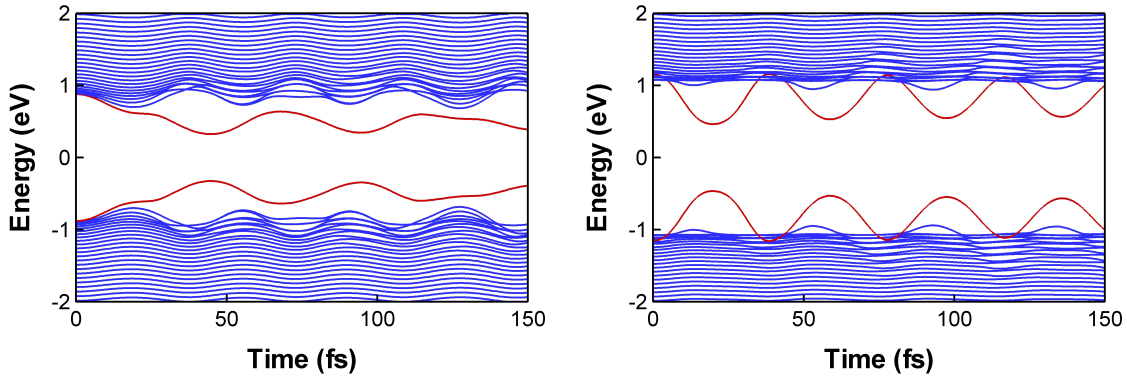

(a) (b)

Figure 6.4: Time evolutions of the energies of the instantaneous adiabatic orbitals (close to the band edges), obtained for a $1\,^1B_u$ photoexcited state in a 200-site cis*-polyacetylene chain, considering the SSH (a) and SSH + PPP (b) models. The energies of the gap states are shown in red.*

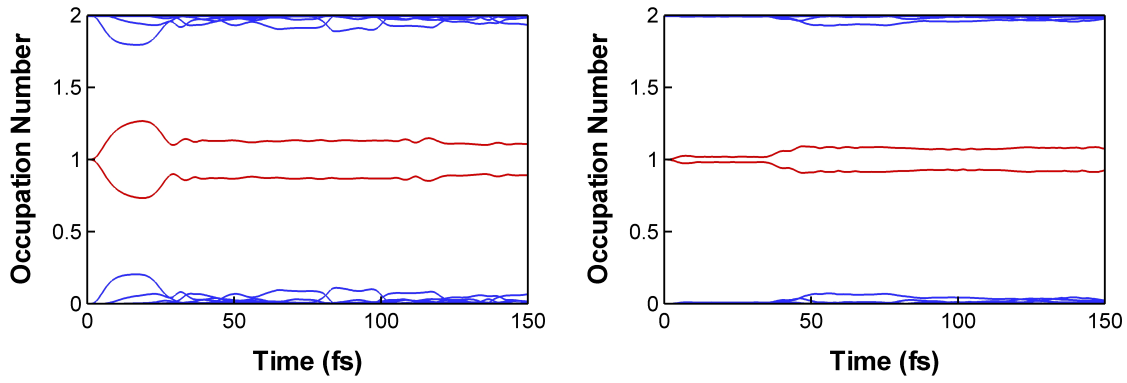

(a) (b)

Figure 6.5: Time evolutions of the occupation numbers of the instantaneous adiabatic orbitals, obtained for a $1\,^1B_u$ photoexcited state in a 200-site cis*-polyacetylene chain, considering the SSH (a) and SSH + PPP (b) models. The occupancies of the gap states are shown in red.*

with and without Coulomb interactions. As for the dimerisation patterns, the results are qualitatively similar, exhibiting two states which oscillate back and forth, splitting from the bands and entering the gap, where they become localised. It is noteworthy that there is a direct correspondence between the time instants at which those two states are deep within the gap in figure 6.4, and the instants at which the peaks in the dimerisation patterns reach their maximum amplitude in figure 6.2. It is clear from figure 6.4 that the period between oscillations is much shorter in the SSH + PPP case, corroborating the important role of Coulomb interactions in promoting localisation. As shown in figure 6.5, the occupancies of the gap states are always close to one. All these results constitute a signature of an electron-hole pair, trapped in the region of lattice distortion. Therefore, within both the SSH and SSH + PPP models, the $1\,^1B_u$ photoexcited state corresponds to a *polaron-exciton*.

6.4 Dynamics of the $2\,^1B_u$ photoexcited state

Let us now consider the case of a $2\,^1B_u$ photoexcited state. The initial conditions are prepared as described in the previous section, with the difference that in this case a HOMO $-$ 1 $\rightarrow$ LUMO + 1 (or 2 $\rightarrow$ 2) excitation is created instead. The dimerisation patterns obtained for a 200-site *cis*-polyacetylene chain, through the numerical integration of the equations of motion for the SSH and SSH + PPP models, are shown in figure 6.6. As can be seen, in this case the lattice relaxes to form two separated local deformations rather than a single one. Similarly to what was observed for the $1\,^1B_u$ photoexcited state, there is a dynamical oscillation between the A and B phases at the centre of the regions of lattice distortion, leading to alternating peaks and troughs. Again, the "period" between peaks is shorter for the SSH + PPP model, which suggests that Coulomb interactions promote the creation of the local deformations in this case as well. Additionally, it is clear from the figure that the widths of the peaks are somewhat smaller in the SSH + PPP case, and thus adding Coulomb interactions results in the formation of more localised regions of distortion.

To properly understand the nature of the $2\,^1B_u$ photoexcited state, we now pro-

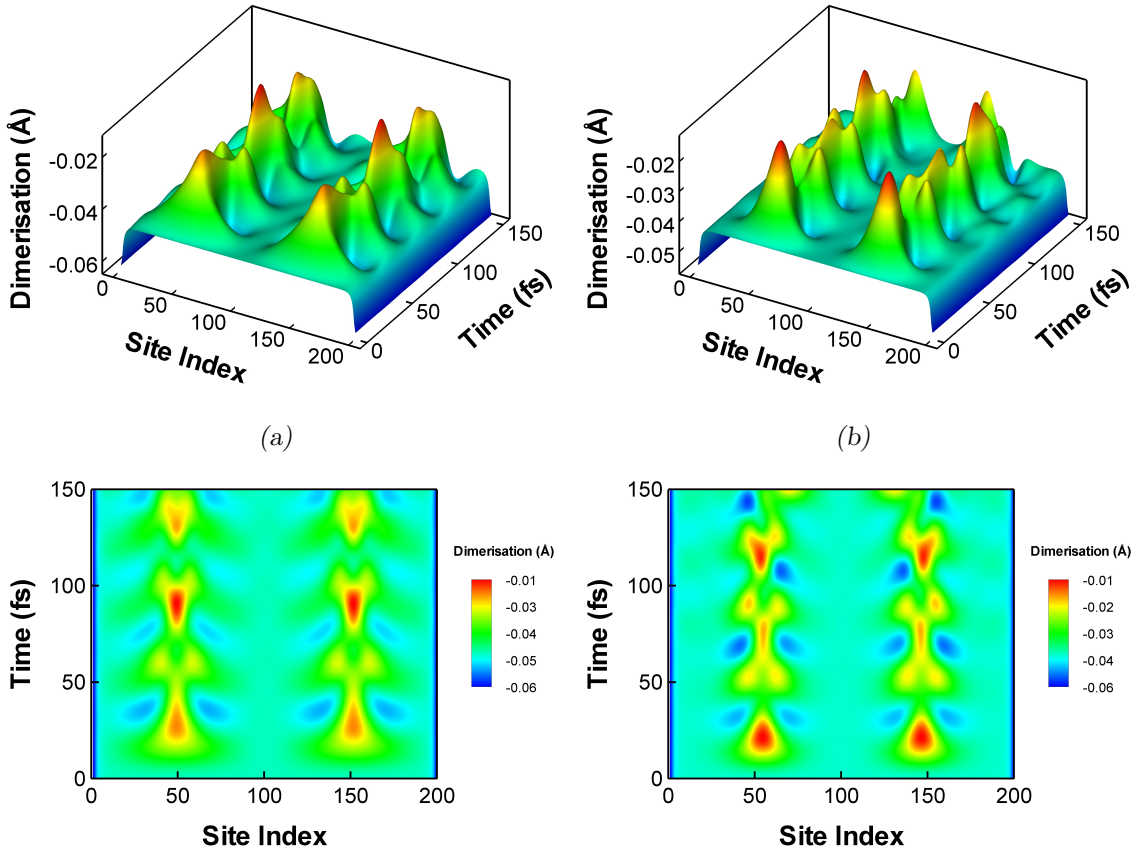

Figure 6.6: Side [(a) and (b)] and top [(c) and (d)] views of the time evolutions of the dimerisation pattern, obtained for a $2\,^1B_u$ photoexcited state in a 200-site cis-polyacetylene chain, considering the SSH [(a) and (c)] and SSH + PPP [(b) and (d)] models.

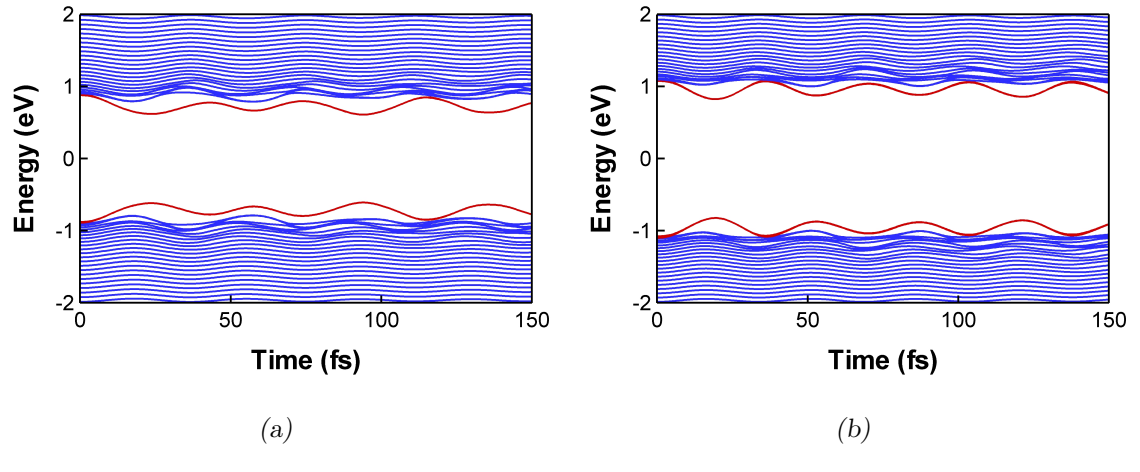

Figure 6.7: Time evolutions of the energies of the instantaneous adiabatic orbitals (close to the band edges), obtained for a $2\,^1B_u$ photoexcited state in a 200-site cis-polyacetylene chain, considering the SSH (a) and SSH + PPP (b) models. The energies of the gap states are shown in red (note that these constitute sets of two pairs of nearly-degenerate states).

ceed to investigate the instantaneous adiabatic single-particle orbitals, which are obtained as described in the previous section. Figure 6.7 shows the time evolutions of the energies of these orbitals near the band edges, calculated for the same 200-site chain, considering both the SSH and SSH + PPP models. In this case, there are two pairs of nearly-degenerate states oscillating back and forth between the bands and the gap. Similarly to what was observed for the $1\,^1B_u$ photoexcited state, there is a correspondence between the time instants at which those four states lie deepest in the gap, and the instants at which the peaks in the dimerisation patterns reach their maximum values. It is also clear from the figure that the period between oscillations is shorter in the SSH + PPP case, supporting the decisive role played by Coulomb interactions in promoting localisation.

Since the gap states, denoted by $\varphi_1^{(v)}$, $\varphi_2^{(v)}$ and $\varphi_1^{(c)}$, $\varphi_2^{(c)}$, form nearly-degenerate pairs, the symmetric and antisymmetric combinations

$$\begin{aligned} |\chi_{L,R}^{(v)}\rangle &= \frac{1}{\sqrt{2}}\left(|\varphi_1^{(v)}\rangle \pm |\varphi_2^{(v)}\rangle\right), \\ |\chi_{L,R}^{(c)}\rangle &= \frac{1}{\sqrt{2}}\left(|\varphi_1^{(c)}\rangle \pm |\varphi_2^{(c)}\rangle\right) \end{aligned} \tag{6.37}$$

are approximate eigenfunctions of the electronic part of the Hamiltonian (or, in the SSH + PPP case, they still bring the electronic energy to a minimum). As shown in figure 6.8, these new orbitals are localised either on the left or on the right side of the chain. Moreover, if we calculate their occupation numbers using expression (6.36), we find that there is a total of three electrons in the states that split from the valence band, and only one in those which originated from the conduction band (see figure 6.9). Thus, we may interpret the observed dimerisation patterns, with two separated local deformations, as corresponding to four possible configurations, depicted in figure 6.10. Depending on how the gap states are populated, species with different character emerge, namely, an exciton localised on one side of the chain, and two oppositely charged polarons localised on different sides (see figure 6.10). The probability of each case can be calculated by building an appropriate many-body wavefunction, Φ, using the valence band states $\varphi_i^{(v)}$, $i = 3, \ldots, N/2$, and the necessary orbitals from the set $\left\{\chi_L^{(v)}, \chi_R^{(v)}, \chi_L^{(c)}, \chi_R^{(c)}\right\}$, and projecting it onto the time-evolving many-body wavefunction, Ψ:

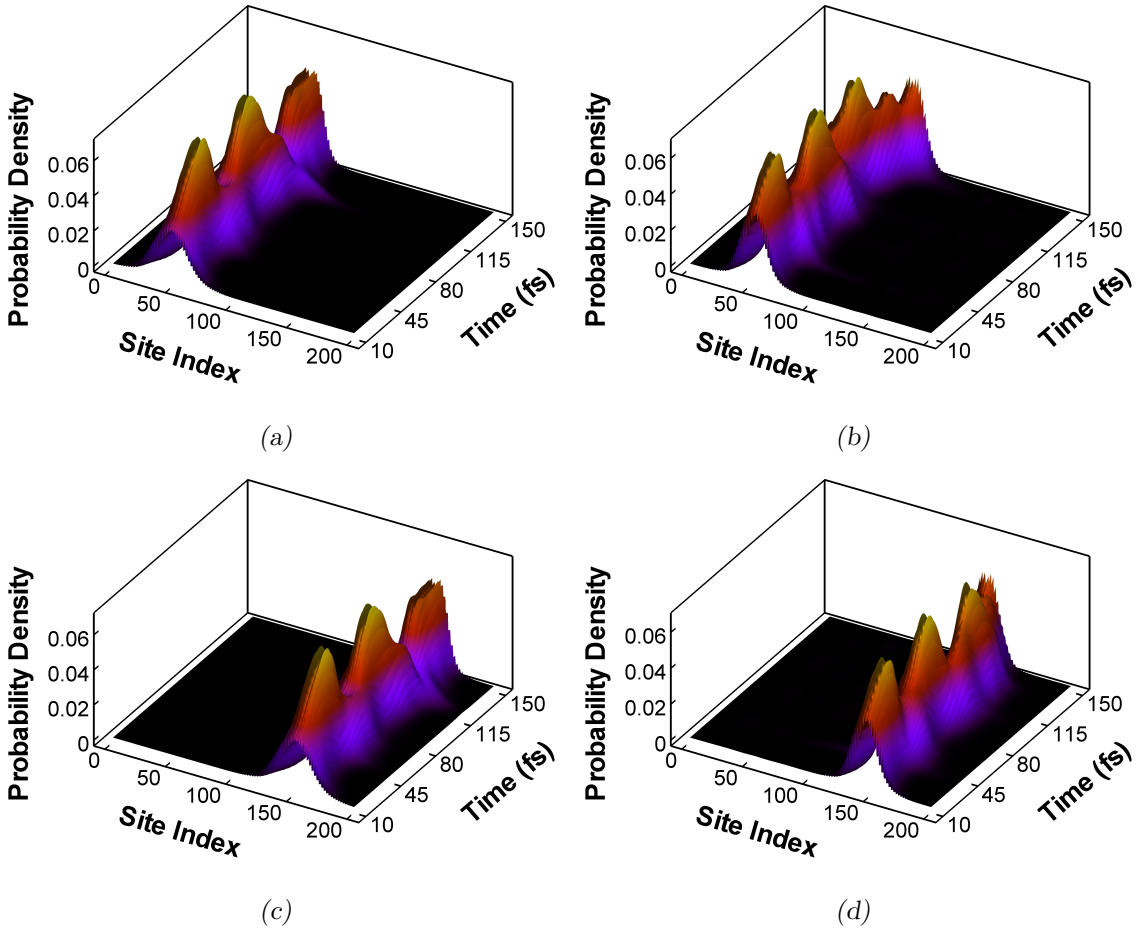

Figure 6.8: Probability densities associated with the symmetric and antisymmetric combinations of the gap states, obtained for a $2\,^1B_u$ photoexcited state in a 200-site cis-polyacetylene chain, considering the SSH [(a) and (c)] and SSH + PPP [(b) and (d)] models. Such linear superpositions lead to states localised on the left [(a) and (b)] or right [(c) and (d)] sides of the chain.

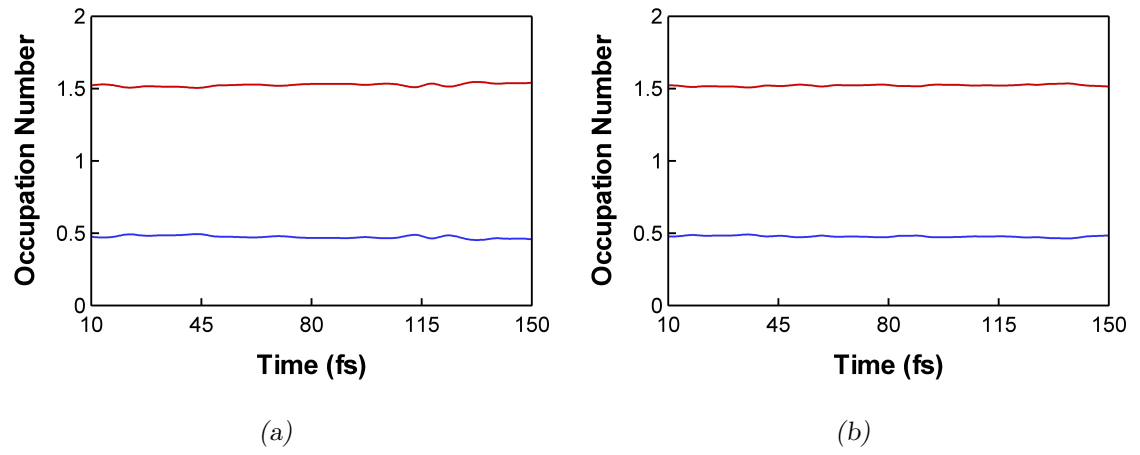

Figure 6.9: Time evolutions of the occupancies of the gap states, obtained for a $2\,^1B_u$ photoexcited state in a 200-site cis-polyacetylene chain, considering the SSH (a) and SSH + PPP (b) models. The red (blue) line corresponds to the states that split from the valence (conduction) band.

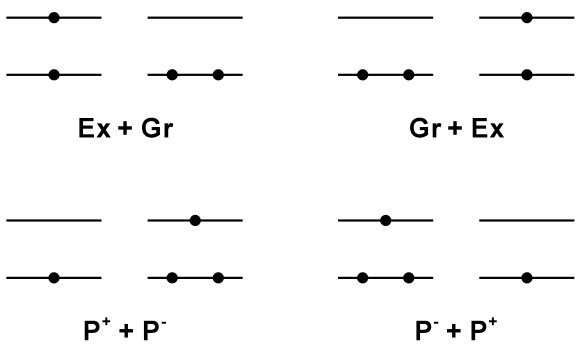

Figure 6.10: Possible configurations corresponding to a dimerisation profile with two separated local deformations [43]*, as obtained for a* $2\,^1B_u$ *photoexcited state in a* 200*-site* cis*-polyacetylene chain. These involve combinations of a few species localised on the left and right sides of the chain: exciton (*Ex*), ground state (*Gr*), hole- or positive polaron (*P^+*) and electron- or negative polaron (*P^-*).*

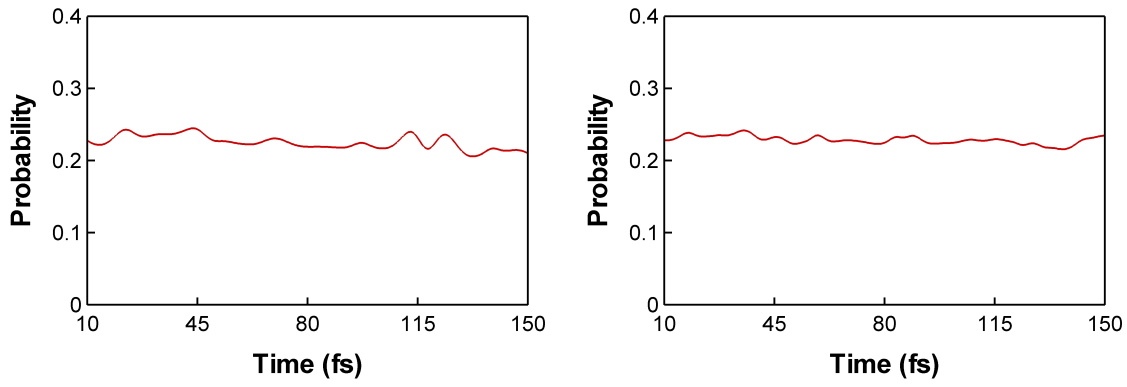

(a) *(b)*

Figure 6.11: Probability of each of the configurations corresponding to a dimerisation profile with two separated local deformations, obtained considering the SSH (a) and SSH + PPP (b) models. Note that, in both panels, all the curves overlap.

$$
\begin{aligned}
p\,(\mathrm{Ex}+\mathrm{Gr}) &= \left|\langle\Phi_{\mathrm{Ex+Gr}}|\Psi\rangle\right|^2, \\
p\,(\mathrm{Gr}+\mathrm{Ex}) &= \left|\langle\Phi_{\mathrm{Gr+Ex}}|\Psi\rangle\right|^2, \\
p\,(\mathrm{P}^+ + \mathrm{P}^-) &= \left|\langle\Phi_{\mathrm{P^+ + P^-}}|\Psi\rangle\right|^2, \\
p\,(\mathrm{P}^- + \mathrm{P}^+) &= \left|\langle\Phi_{\mathrm{P^- + P^+}}|\Psi\rangle\right|^2.
\end{aligned}
\tag{6.38}
$$

Using the general relation for the inner product of two Slater determinants [119],

$$\langle\Phi|\Psi\rangle = \det \mathbf{M}, \tag{6.39}$$

where $\mathbf{M}$ denotes the matrix of elements $M_{ij} = \langle\phi_i|\psi_j\rangle$, the projections may be easily computed. As shown in figure 6.11, we find that the probability of each configuration is about 25%. Therefore, within both the SSH and SSH + PPP models, the $2\,^1B_u$ photoexcited state corresponds to a *superposition with equal weights of exciton and oppositely charged polarons*, as previously suggested by An *et al.* [43].

6.5 The $2\,^1B_u$ photoexcited state under external field

In order to address the issue of charge photogeneration in conjugated polymers in dilute solution, it is instructive to investigate how the photoexcited states respond to an electric field. The case of a $2\,^1B_u$ state is particularly relevant, since, as we have shown, this state is partly polaronic in nature.

To set the stage, let us first examine what happens to *free charges* under an applied field. We consider a 200-site *cis*-polyacetylene chain with an *added electron* (i.e., with a total of 201 electrons), and depart from the minimum of the potential energy surface of this *polaron state* (which is found using the BFGS strategy, as in previous sections). The initial conditions are completed by setting the ionic momenta and the external applied electric field to zero. The field then increases linearly with time, up to a strength of 5 mV/Å over a time window of 1 ps, as the system is propagated via numerical integration of the equations of motion. In figure 6.12 we show the time evolutions of the dimerisation and *electronic charge distribution*,

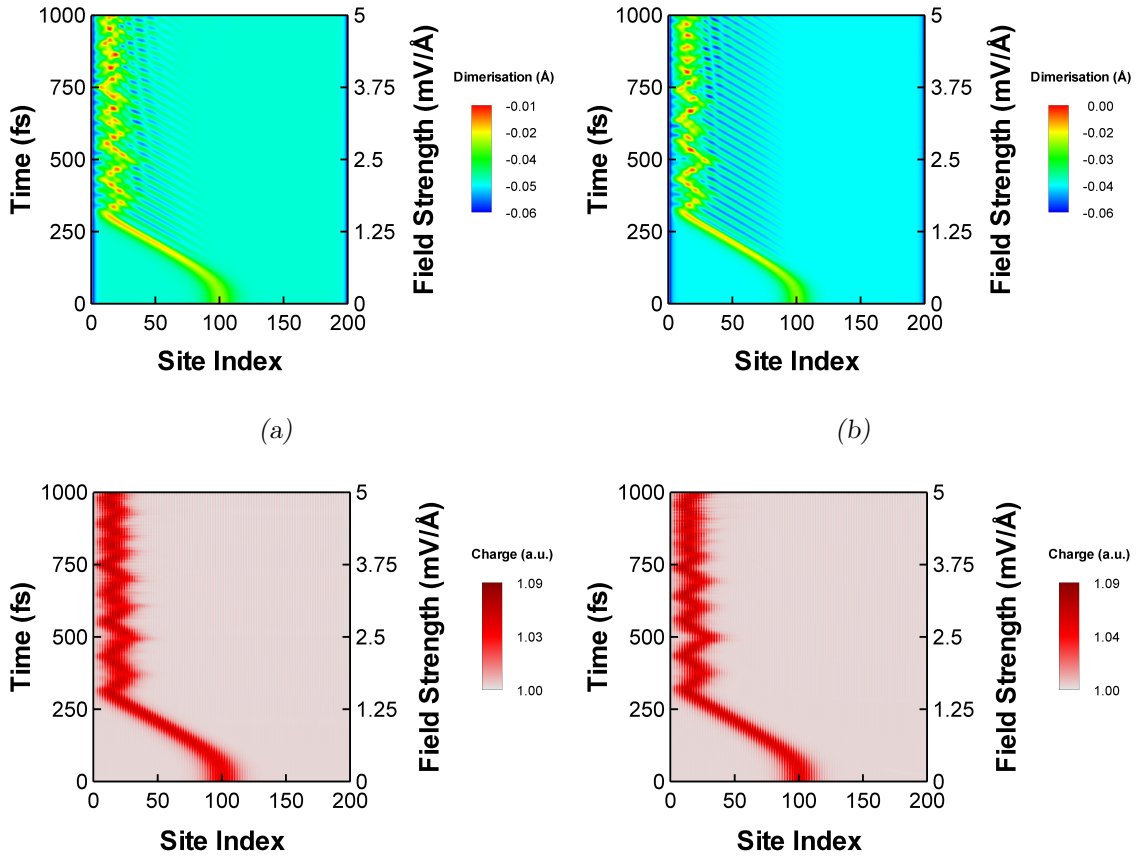

Figure 6.12: Time evolutions of the dimerisation pattern [(a) and (b)] and electronic charge distribution [(c) and (d)], obtained for a polaron state in a 200-site cis-polyacetylene chain, considering the SSH [(a) and (c)] and SSH + PPP [(b) and (d)] models with applied field.

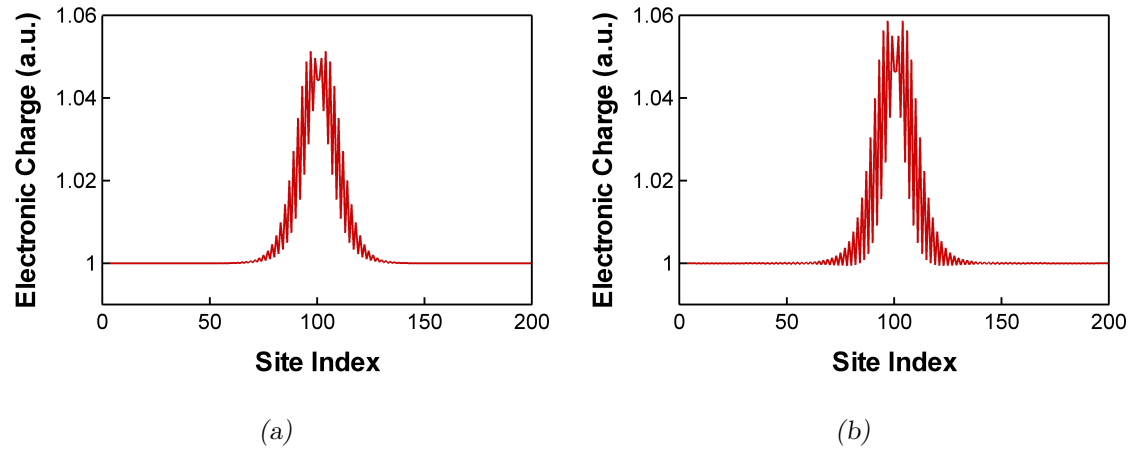

Figure 6.13: Electronic charge distributions at $t = 0$, obtained for a polaron state in a 200-site cis-polyacetylene chain, considering the SSH (a) and SSH + PPP (b) models.

$$q_i = -e\,\rho_{ii}, \tag{6.40}$$

calculated both with and without Coulomb interactions. As can be seen, the added electron leads to a compact region of charge and lattice distortion, initially located at the centre of the chain. After a critical value of the field is reached, which is relatively low and not significantly different for both models, this *polaron structure* starts moving until it reaches the chain end, after which a series of oscillations take place. These correspond to the polaron being successively reflected at the boundary, and pushed back to the chain end by the field. It is clear from the figure that the polaron width is somewhat smaller for the SSH + PPP model, and thus, as already established for photoexcited states, adding Coulomb interactions gives rise to a more localised excitation. It is also noteworthy that the charge distributions exhibit oscillations in the region of distortion, a characteristic feature of soliton and polaron excitations [45]. As shown more clearly in figure 6.13, the charge oscillations are more pronounced when Coulomb interactions are included.

Let us now turn to the case of a $2\,^1B_u$ photoexcited state. We consider a 200-site chain and an external electric field applied at $t = 50$ fs, increasing linearly up to a strength of 5 mV/Å over a time window of 1 ps. The charge distributions obtained through the numerical integration of the equations of motion for the SSH

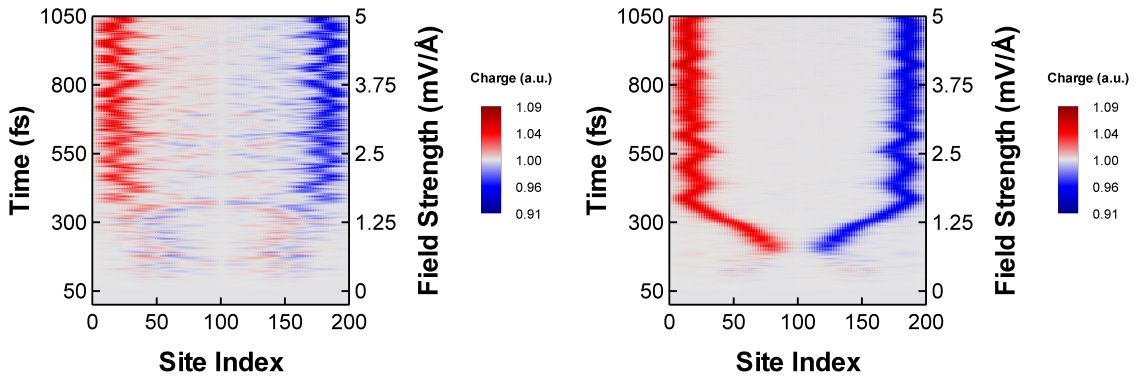

(a) *(b)*

Figure 6.14: Time evolutions of the electronic charge distribution, obtained for a $2\,^1B_u$ photoexcited state in a 200-site cis-polyacetylene chain, considering the SSH (a) and SSH + PPP (b) models with applied field.

and SSH + PPP models (with added field term), are shown in figure 6.14. The first thing to notice is that including Coulomb interactions leads to a substantially higher degree of charge confinement, which renders the picture obtained in the SSH + PPP case much more clear. In this case, it is seen that initially as the field increases there is a slight lattice polarisation, as one would expect for excitons. When the field strength reaches a value about 2–3 times higher than that required to trigger polaron motion, there are two regions of opposite charge which split at the centre of the chain, and start moving towards the chain ends. From this point on, the results may be interpreted as two oppositely charged polarons moving under an applied field. Although the picture obtained in the SSH case is less clear, since the charge is spread over many more lattice sites, there does not seem to be any evidence of polaron motion at the early stages, when the field strength is relatively low. These results suggest that, although the $2\,^1B_u$ photoexcited state corresponds to a superposition of exciton and oppositely charged polarons, the polarons *do not behave as free charges*, and the charge carriers are the result of the *field-induced exciton dissociation*.

6.6 Singlet *vs* triplet excitons

This section presents a comparison between the dynamics of the lowest singlet and triplet excited states, $1\,^1B_u$ and $1\,^3B_u$. The lack of Coulomb interactions in the SSH model means that this model is "blind" to the spin symmetry of these two states, and thus unable to reproduce any difference between them. Indeed, in this case, the dynamics of the $1\,^3B_u$ state is exactly the same as for the $1\,^1B_u$ state, already studied in section 6.3. In contrast, for the SSH + PPP model, within the multiconfigurational time-dependent Hartree-Fock formalism, the difference in the spin symmetries is captured by the different shell structures associated with each of those states, which may have important consequences for the dynamics. Hence, in the following we will only consider this latter model.

The initial conditions are prepared as described in section 6.3, with the appropriate shell structures being set up. The time evolutions of the dimerisation obtained

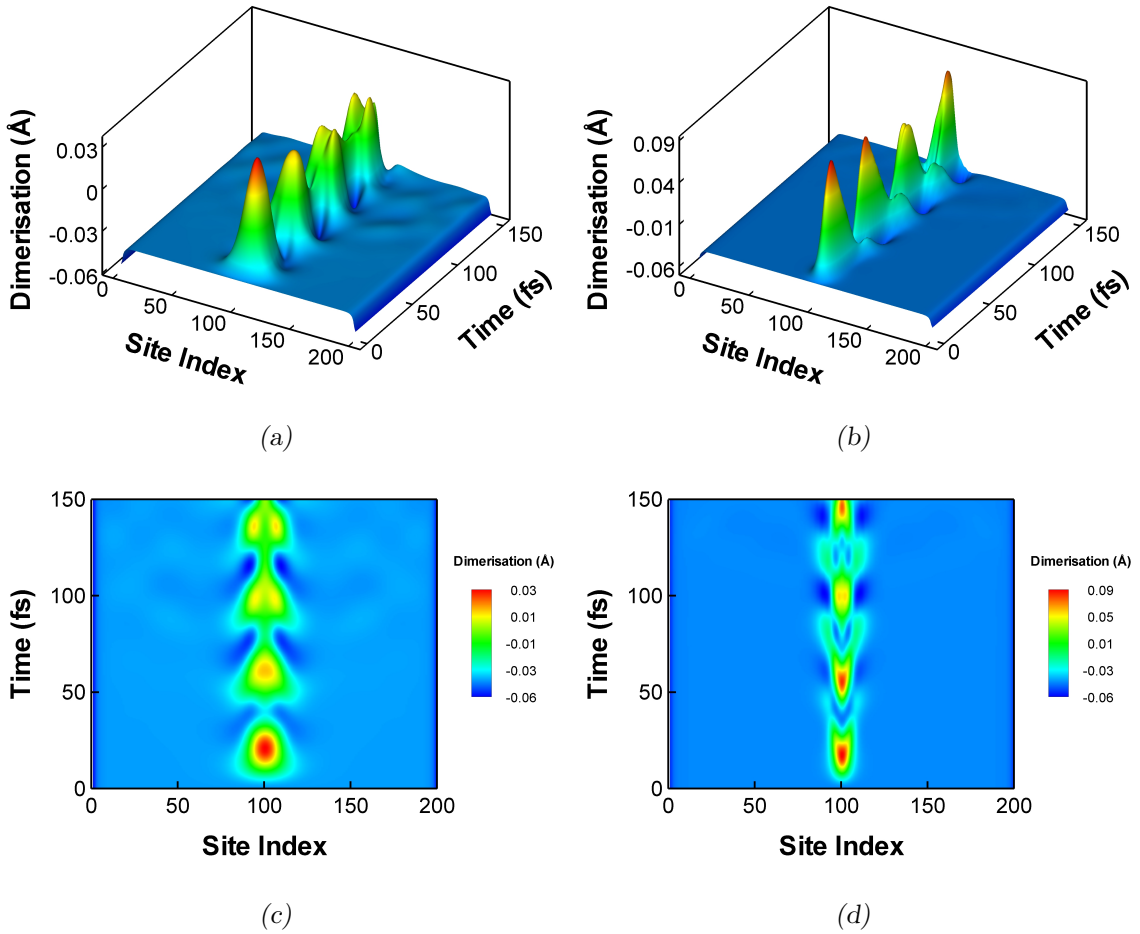

Figure 6.15: Side [(a) and (b)] and top [(c) and (d)] views of the time evolutions of the dimerisation pattern, obtained for $1\,^1B_u$ [(a) and (c)] and $1\,^3B_u$ [(b) and (d)] excited states in a 200-site cis-polyacetylene chain, considering the SSH + PPP model.

for the lowest singlet and triplet excited states in a 200-site *cis*-polyacetylene chain are shown in figure 6.15. As can be seen, in both cases the lattice relaxes to form a single local deformation, which corresponds to a polaron-exciton. There is a dynamical oscillation between the A and B phases at the centre of the chain, leading to alternating peaks and troughs, with a periodicity not significantly different in both cases. It is clear from the figure that the width of the peaks is much smaller for the $1\,^3B_u$ state. Additionally, the dimerisation in the region of distortion reaches values substantially higher in this case as well. Thus, triplet excitons are much more localised than singlet excitons, and they are accompanied by an enhanced lattice distortion. This is in agreement with other theoretical predictions and experimental observations [130–134].

6.7 Conclusions

We have studied the effect of electron-electron interactions on the dynamics of low-lying excitations in a prototypical conjugated polymer, described by simple semiempirical models, both with and without Coulomb interactions. Our findings suggest that adding Coulomb interactions promotes the localisation of photoexcitations, leading to the formation of more confined regions of lattice distortion, which are created more rapidly. At the same time, it also suppresses certain dynamical processes, such as the continuous phase oscillation exhibited in the dynamics of photoexcitations. Polarons are also more localised when Coulomb interactions are included, and they show more pronounced charge oscillations in the region of distortion. Perhaps the most striking effect is the difference between the lowest singlet and triplet excited states, which can only be observed when Coulomb interactions are included. Our findings show that triplet excitons are much more localised than singlet excitons, and they are accompanied by an enhanced lattice distortion, in agreement with other theoretical predictions and experimental evidence [130–134].

The nature of the photoexcited states and the issue of charge photogeneration in conjugated polymers in dilute solution were also addressed. Our results show that the $1\,^1B_u$ photoexcited state corresponds to a polaron-exciton, while the $2\,^1B_u$ state is a superposition with equal weights of exciton and oppositely charged polarons. The conclusion is the same whether Coulomb interactions are included or not. This result, together with the similar energies and transition dipole moments of those excitations, has been used to argue that the charge carriers in conjugated polymers are photogenerated directly on ultrafast time scales, with a quantum yield of about 25% [43]. However, as our calculations with an external electric field clearly indicate, the polarons of the $2\,^1B_u$ photoexcited state do not behave as free charges. In order to get a measurable photocurrent, the charge carriers must be produced on longer time scales through exciton dissociation mechanisms, such as the field-induced splitting.

Chapter 7

Dynamics of photoexcitations in coupled *cis*-polyacetylene chains

7.1 Equations of motion

This chapter is devoted to the study of interchain interaction effects on the dynamics of low-lying excitations in coupled *cis*-polyacetylene chains. To this end, the formalism described in chapter 5 is applied to a system of two parallel chains, considering different regimes of the interchain coupling strength. The system is modelled by the following coupled-chain Hamiltonian, introduced in section 3.5:

$$\begin{aligned}\hat{H} = & -\sum_{q,i_q,\sigma} t_{i_q}\left(\hat{c}^{\dagger}_{i_q\sigma}\,\hat{c}_{i_q+1,\sigma}+\hat{c}^{\dagger}_{i_q+1,\sigma}\,\hat{c}_{i_q\sigma}\right)-t_{\perp}\sum_{\langle i_1,i_2\rangle,\sigma}\left(\hat{c}^{\dagger}_{i_1\sigma}\,\hat{c}_{i_2\sigma}+\hat{c}^{\dagger}_{i_2\sigma}\,\hat{c}_{i_1\sigma}\right)+\\ & +U\sum_{q,i_q}\left(\hat{n}_{i_q\uparrow}-\frac{1}{2}\right)\left(\hat{n}_{i_q\downarrow}-\frac{1}{2}\right)+\frac{1}{2}{\sum_{q,q',i_q,j_{q'}}}'\, v_{i_q j_{q'}}\left(\hat{n}_{i_q}-1\right)\left(\hat{n}_{j_{q'}}-1\right)+\\ & +\frac{1}{2M}\sum_{q,i_q}p^2_{i_q}+\frac{K}{2}\sum_{q,i_q}\left(u_{i_q+1}-u_{i_q}\right)^2.\end{aligned} \tag{7.1}$$

In the above expression, i_q runs over sites of chain q ($q=1,2$), the symbol $\sum_{\langle i_1,i_2\rangle}$ means that the sum is restricted to pairs of neighbouring sites in the opposite strands (i.e., sites facing each other), and $\sum'$ is used to indicate that the onsite terms $v_{i_q i_q}$ are excluded from the summation. The intrachain hopping integral, t_{i_q}, and the

Ohno potential, $v_{i_q j_{q'}}$, respectively read

$$\begin{aligned} t_{i_q} &= t_0 - \alpha\,(u_{i_q+1} - u_{i_q}) + (-1)^{i_q+1}\,t_{\rm e}, \\ v_{i_q j_{q'}} &= \frac{U}{\sqrt{1 + (\beta\, r_{i_q j_{q'}}/r_0)^2}}, \end{aligned} \tag{7.2}$$

while the interchain hopping integral, $t_\perp$, is calculated as a function of the interchain distance, d (expressed in angstroms), using

$$t_\perp = \frac{t_0}{10}\,\exp\left(1 - \frac{d}{5}\right), \tag{7.3}$$

which provides a value of ~ 0.2 eV at a distance of 5 Å, typical of dense conjugated polymer films [56]. The remaining model parameters are taken as those appropriate for *cis*-polyacetylene, which were used in the previous chapter for the SSH + PPP model (see table 6.1). Also, note that the end sites for both chains are kept fixed, and that the nuclei are constrained to move only along the chains.

To derive the equations of motion for the nuclear and electronic degrees of freedom, we now proceed as in section 6.1. The force on atom $k_{q'}$, $k_{q'} = 2, \ldots, N_{q'} - 1$, is written as a sum of electronic and nuclear contributions:

$$F_{k_{q'}} \equiv F^{(\rm e)}_{k_{q'}} + F^{(\rm n)}_{k_{q'}} = -\frac{\partial}{\partial u_{k_{q'}}} V_{\rm e} - \frac{\partial}{\partial u_{k_{q'}}} V_{\rm n}, \tag{7.4}$$

where $V_{\rm e}$ is of the form (5.66), and

$$V_{\rm n} = \frac{K}{2} \sum_{q,i_q} (u_{i_q+1} - u_{i_q})^2 + \frac{1}{2} {\sum_{q,q'',i_q,j_{q''}}}' v_{i_q j_{q''}}. \tag{7.5}$$

Let us start with the nuclear contribution to the force. We can write

$$F^{(\rm n)}_{k_{q'}} = -K \sum_{q,i_q} (u_{i_q+1} - u_{i_q})\,\frac{\partial}{\partial u_{k_{q'}}} (u_{i_q+1} - u_{i_q}) - \frac{1}{2} {\sum_{q,q'',i_q,j_{q''}}}' \frac{\partial v_{i_q j_{q''}}}{\partial r_{i_q j_{q''}}}\,\frac{\partial r_{i_q j_{q''}}}{\partial u_{k_{q'}}}. \tag{7.6}$$

The distance between sites i_q and $j_{q''}$ can be calculated as

$$r_{i_q j_{q''}} = \sqrt{(x_{i_q} - x_{j_{q''}})^2 + (y_{i_q} - y_{j_{q''}})^2}, \tag{7.7}$$

with the Cartesian components

$$\begin{aligned} x_{i_q} &= \left[i_q - 1 - (q-2)\,\frac{N_2 - N_1}{2} \right] r_0 + u_{i_q}, \\ y_{i_q} &= (q-1)\,d, \end{aligned} \tag{7.8}$$

where we have assumed $N_2 \geq N_1$. The derivative of the distance with respect to the lattice displacement $u_{k_{q'}}$ is thus given by

$$\frac{\partial r_{i_q j_{q''}}}{\partial u_{k_{q'}}} = \frac{x_{i_q} - x_{j_{q''}}}{r_{i_q j_{q''}}} \left(\delta_{i_q k_{q'}} - \delta_{j_{q''} k_{q'}}\right). \tag{7.9}$$

Inserting the above expression into equation (7.6), yields

$$\begin{aligned} F^{(\mathrm{n})}_{k_{q'}} = & -K \sum_{q,i_q} \left(u_{i_q+1} - u_{i_q}\right) \left(\delta_{i_q+1,k_{q'}} - \delta_{i_q k_{q'}}\right) - \\ & - \frac{1}{2} \sum_{q,q''} \sum_{i_q, j_{q''}} \frac{\partial v_{i_q j_{q''}}}{\partial r_{i_q j_{q''}}} \frac{x_{i_q} - x_{j_{q''}}}{r_{i_q j_{q''}}} \left(\delta_{i_q k_{q'}} - \delta_{j_{q''} k_{q'}}\right). \end{aligned} \tag{7.10}$$

From (7.2), we find

$$\frac{\partial v_{i_q j_{q''}}}{\partial r_{i_q j_{q''}}} = - \frac{(\beta/r_0)^2 \, r_{i_q j_{q''}}}{1 + (\beta \, r_{i_q j_{q''}}/r_0)^2} \, v_{i_q j_{q''}}, \tag{7.11}$$

and the nuclear contribution to the force reads

$$F^{(\mathrm{n})}_{k_{q'}} = K \left(u_{k_{q'}+1} + u_{k_{q'}-1} - 2\, u_{k_{q'}}\right) - \sum_{q,i_q} d_{i_q k_{q'}}, \tag{7.12}$$

where we have introduced

$$d_{i_q k_{q'}} = \frac{(\beta/r_0)^2 \left(x_{i_q} - x_{k_{q'}}\right)}{1 + (\beta \, r_{i_q k_{q'}}/r_0)^2} \, v_{i_q k_{q'}}. \tag{7.13}$$

Let us now consider the electronic contribution to the force. With the help of equations (3.32) and (3.33), and the usual LCAO expansion of the molecular orbitals,

$$|\phi_{k_\mu}\rangle = \sum_{q,i_q} C_{i_q k_\mu} |\chi_{i_q}\rangle, \tag{7.14}$$

it is possible to rewrite the open-shell electronic energy as

$$\begin{aligned} V_{\mathrm{e}} = & - \sum_{\mu} \sum_{q,i_q} n^\mu \left[P^\mu_{i_q i_q} \left(\frac{U}{2} + {\sum_{q'',j_{q''}}}' v_{i_q j_{q''}} \right) + P^\mu_{i_q+1,i_q} \, t_{i_q} + P^\mu_{i_q-1,i_q} \, t_{i_q-1} \right] + \\ & + \frac{1}{4} \sum_{\mu,\nu} \sum_{q,q''} \sum_{i_q, j_{q''}} n^\mu \, n^\nu \left(2\, a^{\mu\nu} P^\mu_{i_q i_q} P^\nu_{j_{q''} j_{q''}} - b^{\mu\nu} P^\mu_{j_{q''} i_q} P^\nu_{i_q j_{q''}}\right) v_{i_q j_{q''}} - \\ & - \sum_{\mu} \sum_{\langle i_1, i_2 \rangle} n^\mu \left(P^\mu_{i_1 i_2} + P^\mu_{i_2 i_1}\right) t_\perp, \end{aligned} \tag{7.15}$$

where the projector matrix elements read

$$P^{\mu}_{i_q j_{q''}} = \sum_{k_\mu} C_{i_q k_\mu} C^{*}_{j_{q''} k_\mu}. \tag{7.16}$$

Using the result (6.17) to compute the energy gradient, yields

$$\begin{aligned} F^{(\mathrm{e})}_{k_{q'}} = & \sum_{\mu} \sum_{q, i_q} n^{\mu} \left[P^{\mu}_{i_q i_q} \sum_{q'', j_{q''}}{}' \frac{\partial v_{i_q j_{q''}}}{\partial u_{k_{q'}}} + P^{\mu}_{i_q+1, i_q} \frac{\partial t_{i_q}}{\partial u_{k_{q'}}} + P^{\mu}_{i_q-1, i_q} \frac{\partial t_{i_q-1}}{\partial u_{k_{q'}}} \right] - \\ & - \frac{1}{4} \sum_{\mu,\nu} \sum_{q, q''} \sum_{i_q, j_{q''}} n^{\mu} n^{\nu} \left(2\, a^{\mu\nu} P^{\mu}_{i_q i_q} P^{\nu}_{j_{q''} j_{q''}} - b^{\mu\nu} P^{\mu}_{j_{q''} i_q} P^{\nu}_{i_q j_{q''}} \right) \frac{\partial v_{i_q j_{q''}}}{\partial u_{k_{q'}}}. \end{aligned} \tag{7.17}$$

Writing

$$\frac{\partial v_{i_q j_{q''}}}{\partial u_{k_{q'}}} = \frac{\partial v_{i_q j_{q''}}}{\partial r_{i_q j_{q''}}} \frac{\partial r_{i_q j_{q''}}}{\partial u_{k_{q'}}} \tag{7.18}$$

and making use of (7.9) and (7.11), together with

$$\frac{\partial t_{i_q}}{\partial u_{k_{q'}}} = \alpha \left(\delta_{i_q k_{q'}} - \delta_{i_q+1, k_{q'}} \right), \tag{7.19}$$

leads to the final expression

$$\begin{aligned} F^{(\mathrm{e})}_{k_{q'}} = & \sum_{\mu} n^{\mu} \left[\sum_{q, i_q} \left(P^{\mu}_{i_q i_q} + P^{\mu}_{k_{q'} k_{q'}} \right) d_{i_q k_{q'}} + 2\, \alpha \left(\mathrm{Re}\, P^{\mu}_{k_{q'}, k_{q'}+1} - \mathrm{Re}\, P^{\mu}_{k_{q'}, k_{q'}-1} \right) \right] - \\ & - \frac{1}{2} \sum_{\mu,\nu} n^{\mu} n^{\nu} \sum_{q, i_q} \Big[a^{\mu\nu} \left(P^{\mu}_{i_q i_q} P^{\nu}_{k_{q'} k_{q'}} + P^{\mu}_{k_{q'} k_{q'}} P^{\nu}_{i_q i_q} \right) - \\ & \qquad - b^{\mu\nu}\, \mathrm{Re} \left(P^{\mu}_{k_{q'} i_q} P^{\nu}_{i_q k_{q'}} \right) \Big] d_{i_q k_{q'}}. \end{aligned} \tag{7.20}$$

The lattice displacements thus evolve according to

$$M\, \ddot{u}_{k_{q'}} = F_{k_{q'}}, \tag{7.21}$$

for $k_{q'} = 2, \ldots, N_{q'} - 1$, with the total force given by the sum of contributions (7.12) and (7.20).

As discussed in chapter 5, the time-dependent wave equation that governs the evolution of the electronic degrees of freedom can be solved through the multiconfigurational time-dependent Hartree-Fock approach. Combining expressions (5.63) and (7.14), the optimal equations of motion for general open-shell states read

$$\mathrm{i}\, \hbar\, \dot{C}_{i_q k_\mu} = \sum_{q', j_{q'}} R_{i_q j_{q'}} C_{j_{q'} k_\mu}, \tag{7.22}$$

where

$$R_{i_q j_{q'}} = \sum_{\substack{\mu,\nu \\ (n^\mu \neq n^\nu)}} \sum_{q'',q'''} \sum_{k_{q''},l_{q'''}} P^\nu_{i_q k_{q''}} \frac{n^\nu F^\nu_{k_{q''} l_{q'''}} - n^\mu F^\mu_{k_{q''} l_{q'''}}}{n^\nu - n^\mu} P^\mu_{l_{q'''} j_{q'}}. \tag{7.23}$$

Using (3.32) and (3.33), the Fock matrix for shell μ can be written explicitly in the atomic orbitals basis set as

$$\begin{aligned} F^\mu_{i_q j_{q'}} = &- \Bigg\{ \left[\frac{U}{2} + {\sum_{q'',k_{q''}}}' v_{i_q k_{q''}} \right] \delta_{i_q j_{q'}} + t_{i_q} \delta_{i_q+1,j_{q'}} + t_{i_q-1} \delta_{i_q-1,j_{q'}} - \\ &- \left[\sum_\nu \sum_{q'',k_{q''}} n^\nu a^{\mu\nu} P^\nu_{k_{q''} k_{q''}} v_{i_q k_{q''}} \right] \delta_{i_q j_{q'}} \Bigg\} \delta_{qq'} - \\ &- t_\perp \delta_{i_q-(N_q-N_{q'})/2,j_{q'}} \left(1 - \delta_{qq'}\right) - \frac{1}{2} \sum_\nu n^\nu b^{\mu\nu} P^\nu_{i_q j_{q'}} v_{i_q j_{q'}}. \end{aligned} \tag{7.24}$$

As in the previous chapter, the coupled set of differential equations (7.21) and (7.22) will be integrated numerically using an eighth-order Runge-Kutta method with adaptive step-size control [125].

7.2 Interchain coupling effect on the dynamics of the $1\,^1B_u$ photoexcited state

We now specialise to the case of a $1\,^1B_u$ photoexcited state. The initial conditions are obtained by considering the chains to be uncoupled, so that the required minimisations can be performed separately for each strand. The ionic momenta are set to zero, and the initial displacements correspond to the minima of the ground state potential energy surfaces (which are found using the BFGS method, as in the previous chapter). The orbital coefficients are obtained by setting up a HOMO $\rightarrow$ LUMO excitation (or $1 \rightarrow 1$, using the notation introduced in the previous chapter) on the first chain, while the second one remains in the ground state. The interchain coupling is then turned on, and the initial conditions are propagated via numerical integration of the equations of motion, as discussed in the previous section.

Figure 7.1 shows the time evolutions of the dimerisation [43, 44],

$$\delta_{i_q} = \frac{(-1)^{i_q+1}}{4} (u_{i_q+1} + u_{i_q-1} - 2\,u_{i_q}), \tag{7.25}$$

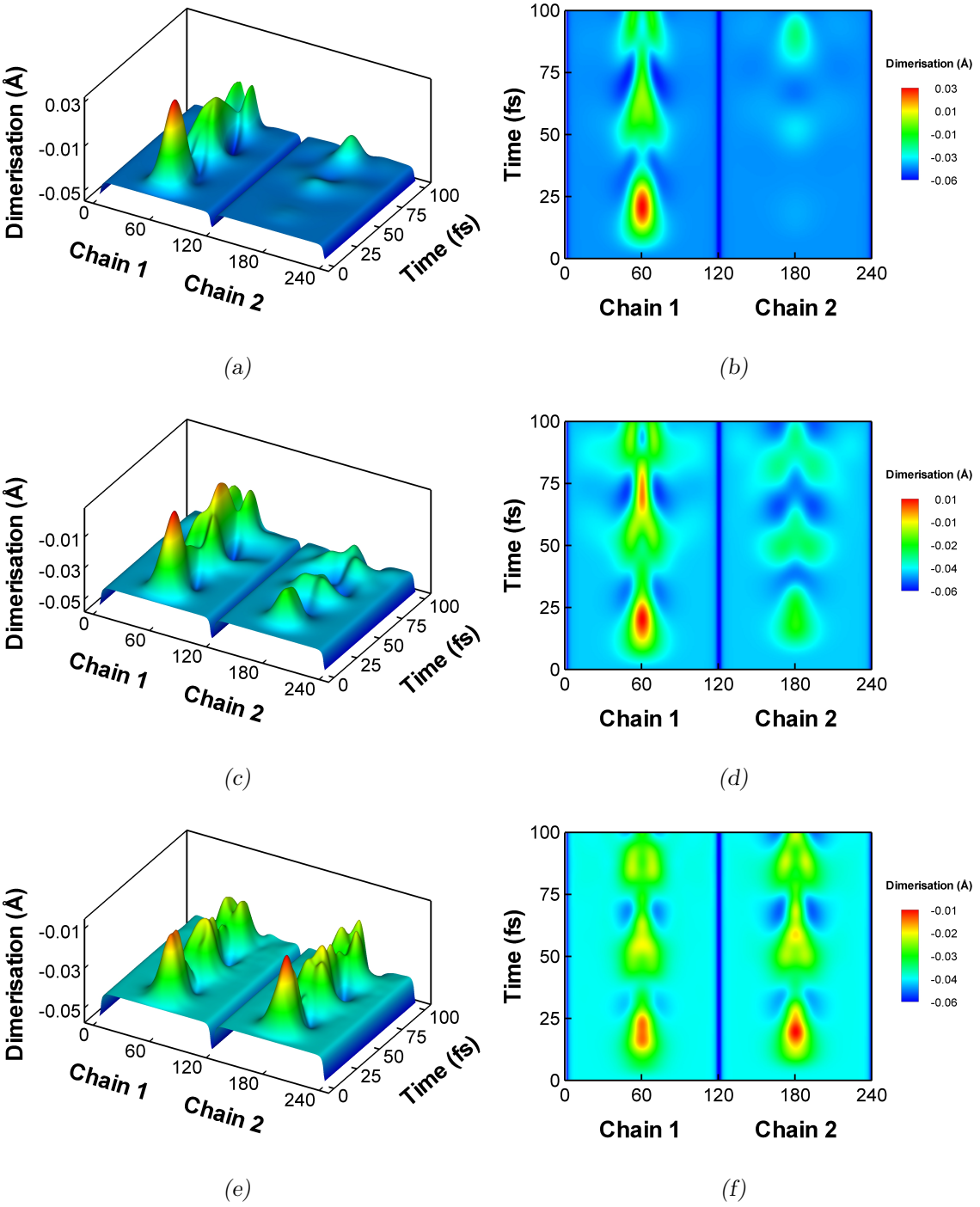

Figure 7.1: Side [(a), (c) and (e)] and top [(b), (d) and (f)] views of the time evolutions of the dimerisation pattern, obtained for a $1\,^1B_u$ photoexcited state in a system of two coupled 120*-site* cis*-polyacetylene chains. The photoexcitation is initially localised on the first chain, and three different regimes of the interchain coupling strength are considered: (a), (b) weak coupling ($d = 15$ Å), (c), (d) intermediate coupling ($d = 10$ Å) and (e), (f) strong coupling ($d = 5$ Å). Note that, for visualisation purposes, the second chain has been shifted by* 120 *sites.*

calculated for a system of two coupled 120-site *cis*-polyacetylene chains, considering three different regimes of the interchain coupling strength. As can be seen, when the interchain distance is large ($d = 15$ Å), the lattice relaxes to form a single local deformation, which is essentially confined to the first strand. Indeed, in this weak coupling limit, the distortion of the second chain slowly builds up, and within the investigated time window is only a small fraction of that observed for the first strand. The evolution of the dimerisation pattern closely resembles that of an isolated chain, with a succession of peaks and troughs only on the first strand, corresponding to a dynamical oscillation between the A and B phases, as discussed in section 6.3. As the chains are brought closer together, the lattice distortion quite rapidly becomes spread out across the two strands. In the intermediate coupling case ($d = 10$ Å), such interchain distribution is uneven (the dimerisation peaks are much more pronounced on the first strand), while in the strong coupling regime ($d = 5$ Å) a mirror-like pattern is obtained, with two separated local deformations (one on each strand) of about the same amplitude. The degree of delocalisation across strands increases with the interchain coupling strength, which suggests that interchain interactions play a fundamental role in determining the intra- or interchain character of the states produced upon photoexcitation.

In order to better understand the effect of interchain coupling on the nature of the $1\,^1B_u$ photoexcited state, we propose an interpretation based on a few many-

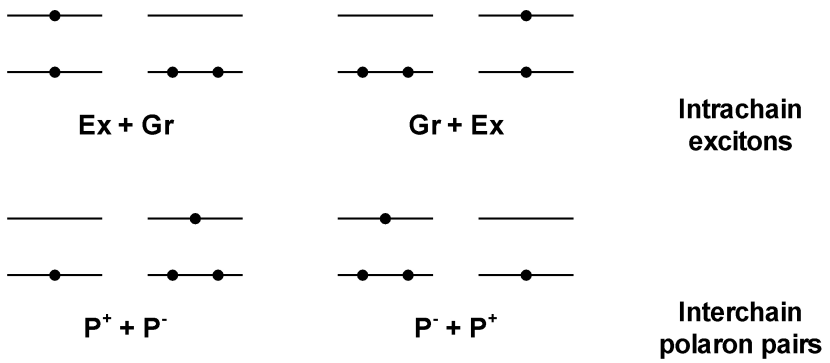

*Figure 7.2: Configurations required to understand the nature of the $1\,^1B_u$ photoexcited state in a system of two coupled polymer chains. These involve combinations of a few species localised on the different strands: exciton (*Ex*), ground state (*Gr*), hole- or positive polaron (*P^+*) and electron- or negative polaron (*P^-*).*

body states built from single-particle eigenfunctions localised on different chains. The idea is to obtain the instantaneous adiabatic orbitals, $\{\varphi_{i_q}^{(v)}, \varphi_{i_q}^{(c)}\}$, separately for each strand through the self-consistent field procedure, and use them to construct a number of many-body states with a well-defined nature. These are then projected onto the time-evolving many-body wavefunction, Ψ, in order to quantify its intra- or interchain character. It is sufficient to consider the four possible configurations that arise from distributing a hole and an electron respectively over the HOMOs and LUMOs of each strand (which are generally located in the gaps, as we have already seen in section 6.3). As depicted in figure 7.2, depending on how the gap states are populated, species with different character emerge, namely, an exciton localised on one of the chains, and two oppositely charged polarons localised on different strands. In this sense, the time-evolving many-body wavefunction is approximated as

$$\begin{aligned} |\Psi\rangle \approx C_{\mathrm{Ex+Gr}}\,|\Phi_{\mathrm{Ex+Gr}}\rangle + C_{\mathrm{Gr+Ex}}\,|\Phi_{\mathrm{Gr+Ex}}\rangle + C_{\mathrm{P^+ + P^-}}\,|\Phi_{\mathrm{P^+ + P^-}}\rangle + \\ + C_{\mathrm{P^- + P^+}}\,|\Phi_{\mathrm{P^- + P^+}}\rangle, \end{aligned} \tag{7.26}$$

where each configuration, Φ_x ($x = \mathrm{Ex+Gr}$, $\mathrm{Gr+Ex}$, $\mathrm{P^+ + P^-}$, or $\mathrm{P^- + P^+}$), is built using the valence band states $\varphi_{i_q}^{(v)}$, $i_q = 2, \ldots, N_q/2$, and the necessary orbitals from the sets $\{\varphi_{1_q}^{(v)}, \varphi_{1_q}^{(c)}\}$. The probability of each case is then given by

$$p_x = \left|C_x\right|^2 = \left|\langle \Phi_x | \Psi \rangle\right|^2, \tag{7.27}$$

and can be readily calculated from the knowledge of the time-evolving and adiabatic single-particle orbitals, as discussed in the previous chapter.

Figure 7.3 shows the time evolutions of the four configurational probabilities, obtained for a system of two coupled 120-site *cis*-polyacetylene chains, separated by the same distances considered before. The first thing to notice is that, in all cases, the four contributions sum to well above 70% most of the time, which confirms that expression (7.26) provides a reasonably good approximation to the time-evolving wavefunction. It is seen that, when the interchain distance is large, the wavefunction is mostly described by the configuration representing an exciton on chain one, in agreement with the results obtained for the dimerisation. Note that, even if the calculation is extended to much longer time scales, the interchain exciton transfer is never significant in this weak coupling limit, as clearly shown in figure 7.4. This is

likely a consequence of treating the ions classically in the Ehrenfest approach, as a fully quantum method should predict complete transfer in the long run. The curves obtained in the weak coupling regime exhibit fast oscillations with small amplitude, modulated by the slower dynamical phase oscillation process. The fast oscillations are not exclusive of interchain dynamics, and are also present in the single-strand case (see figure 7.5). They can be understood by expanding the time-evolving single-particle orbitals in terms of the adiabatic states. Since these have different energies, there will be phases of different frequencies associated with them, leading to the observed oscillations. As the interchain distance decreases, this nonadiabatic effect

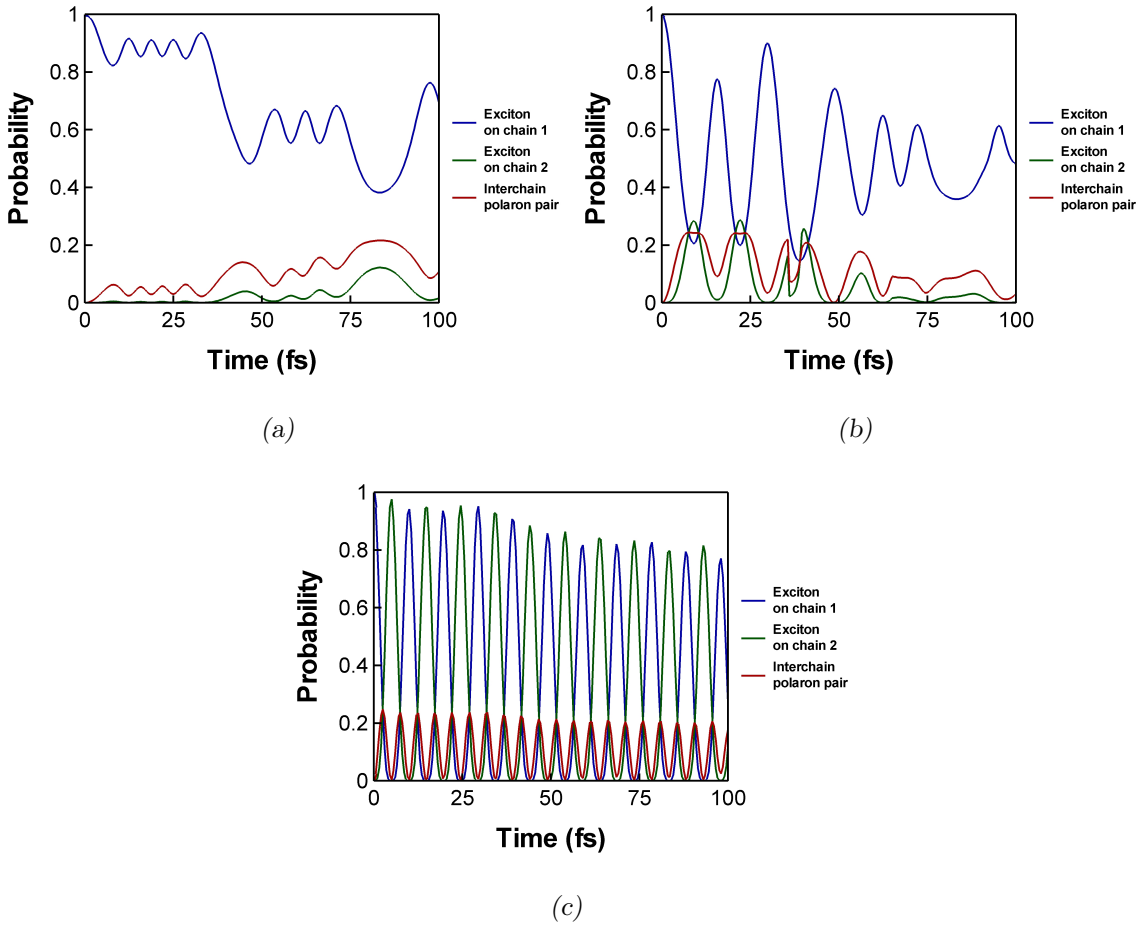

Figure 7.3: Probability of each of the configurations introduced to study the nature of the $1\,^1B_u$ *photoexcited state, obtained for a system of two coupled* 120*-site* cis*-polyacetylene chains, considering three different regimes of the interchain coupling strength: (a) weak coupling (*$d = 15$ Å*), (b) intermediate coupling (*$d = 10$ Å*) and (c) strong coupling (*$d = 5$ Å*). Note that, in all panels, the curves corresponding to interchain polaron pairs overlap.*

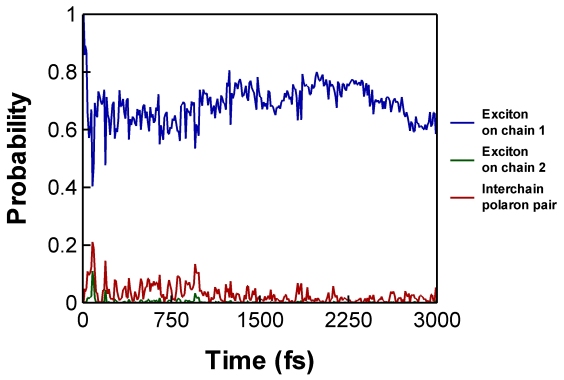

Figure 7.4: Long-time dynamics of the yields of the configurations introduced to study the nature of the $1\,^1B_u$ *photoexcited state, obtained for a system of two coupled* 120*-site* cis*-polyacetylene chains in the weak coupling limit of the interchain coupling strength (*$d = 15$ Å*). Note that the curves corresponding to interchain polaron pairs overlap.*

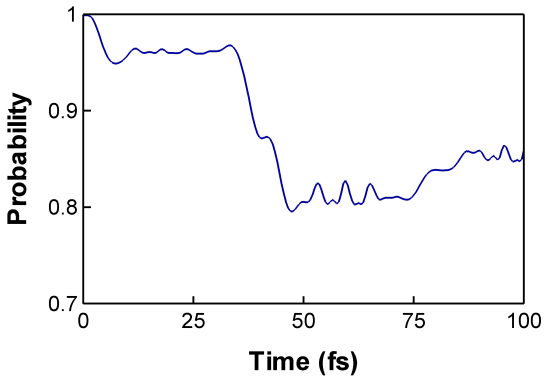

Figure 7.5: Time evolution of the lowest exciton yield, calculated for a $1\,^1B_u$ *photoexcited state in a single* 120*-site* cis*-polyacetylene chain. This is obtained by building a* HOMO $\rightarrow$ LUMO *excitation using the appropriate instantaneous adiabatic orbitals, and projecting the resulting configuration onto the time-evolving many-body wavefunction.*

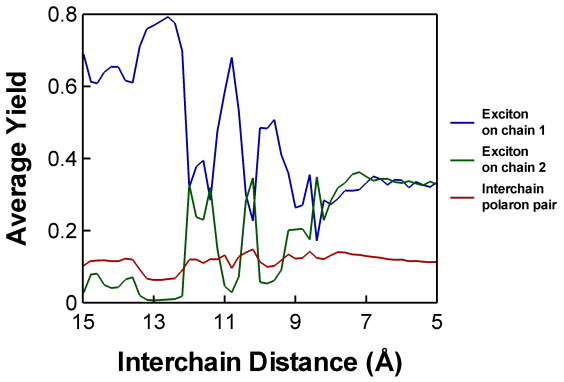

Figure 7.6: Average yields of the configurations introduced to study the nature of the $1\,^1B_u$ *photoexcited state, calculated as a function of interchain distance for a system of two coupled* 120*-site* cis*-polyacetylene chains. Note that the curves corresponding to interchain polaron pairs overlap.*

becomes less noticeable, and faster and more pronounced oscillations take over, as the ultrafast processes of exciton hopping and dissociation into polaron pairs start to play a significant role. Indeed, as depicted in figure 7.3(b), the yields of the configurations associated with an exciton on chain two and with interchain polaron pairs increase considerably, and peak in less than 10 fs. In the strong coupling regime, the dynamics is completely dominated by such ultrafast processes, leading to a constant interchange between the four possible states: the intrachain exciton curves oscillate out-of-phase and with comparable amplitude, while those corresponding to the polaron pairs display a smaller amplitude and peak in between them [see figure 7.3(c)].

To have an idea of the predominance of each configuration over the whole time interval (denoted T), it is useful to further calculate the *average yield*,

$$\langle p_x \rangle = \frac{1}{T} \int_0^T p_x\,(t)\,\mathrm{d}t. \tag{7.28}$$

The results obtained from 51 simulations (up to 100 fs) with the interchain distance varying in the range 15–5 Å are shown in figure 7.6. The three different regimes of the interchain coupling strength can be clearly identified. For the longer distances ($d \gtrsim 12$ Å), the dominant configuration is that corresponding to an exciton on the first strand, whose average yield can reach values as high as 80%. A second region follows, which is marked by a sharp decrease (increase) of the yield of exciton on chain one (two), as well as a definite trend of increasing the average yields of inter-

chain polaron pairs. Such intermediate coupling regime is also characterised by wild oscillations of the intrachain exciton curves, due to the finite nature of the investigated time window. Finally, when the chain separation is small ($d \lesssim 8$ Å), the yields of intrachain excitons stabilise at around 35%, while those of oppositely charged polarons sum to about 25%, in agreement with other theoretical investigations and experimental evidence [39, 42, 56]. These results emphasise the importance of interchain interactions in governing the ultrafast processes of exciton hopping and dissociation into polaron pairs, which ultimately determine the intra- or interchain character of the photogenerated species.

7.3 Interchain coupling effect on the dynamics of the $2\,^1B_u$ photoexcited state

Let us now turn to the case of a $2\,^1B_u$ photoexcited state. The initial conditions are prepared as described in the previous section, with the difference that in this case a HOMO $-$ 1 $\rightarrow$ LUMO + 1 (or simply 2 $\rightarrow$ 2) excitation is created on the first strand instead (we recall that the second one is kept in the ground state). The dimerisation patterns obtained through the numerical integration of the equations of motion for a system of two coupled 120-site *cis*-polyacetylene chains, separated by three different interchain distances, are shown in figure 7.7. As can be seen, when the chain separation is large ($d = 15$ Å), the lattice relaxes to form two separated local deformations, which remain confined to the first chain. There is a dynamical oscillation between the A and B phases at the centre of the regions of lattice distortion, leading to alternating peaks and troughs only on the first strand, thus resembling the dynamics obtained for an isolated chain (see section 6.4). Similarly to what was found for the $1\,^1B_u$ photoexcited state, as the interchain distance decreases the lattice distortion quite rapidly becomes spread out across the two strands, with the interchain distribution being more even when the coupling strength is larger. Indeed, in the strong coupling limit ($d = 5$ Å) a mirror-like pattern is obtained, with four separated local deformations (two on each strand) of about the same amplitude. It is clear that the degree of delocalisation across strands increases as the chains

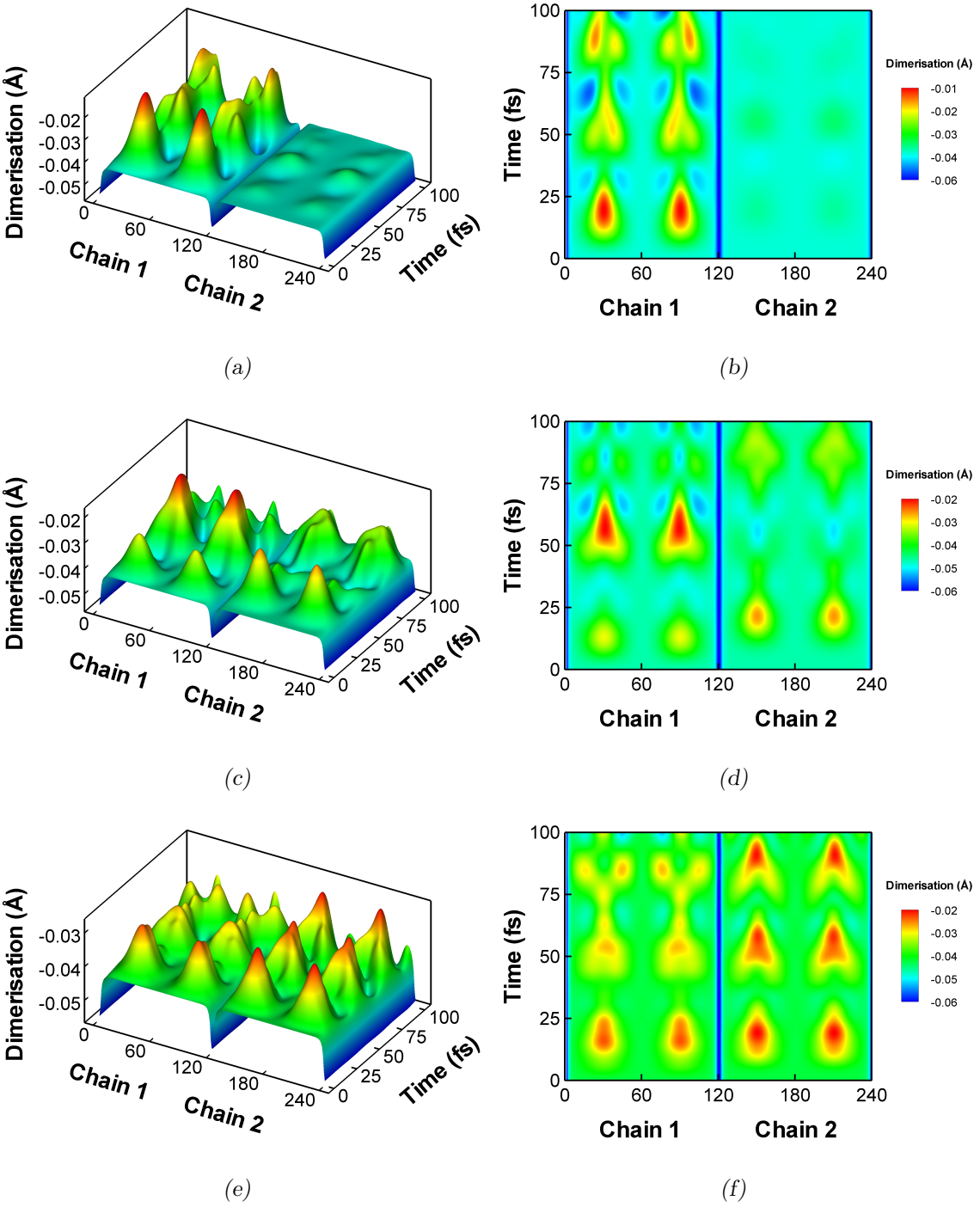

Figure 7.7: Side [(a), (c) and (e)] and top [(b), (d) and (f)] views of the time evolutions of the dimerisation pattern, obtained for a $2\,^1B_u$ photoexcited state in a system of two coupled 120*-site* cis*-polyacetylene chains. The photoexcitation is initially localised on the first chain, and three different regimes of the interchain coupling strength are considered: (a), (b) weak coupling ($d = 15$ Å), (c), (d) intermediate coupling ($d = 10$ Å) and (e), (f) strong coupling ($d = 5$ Å). Note that, for visualisation purposes, the second chain has been shifted by* 120 *sites.*

are brought closer together, which suggests that the nature of the photogenerated species depends critically on the strength of interchain interactions.

As discussed in the previous section, the nature of the photoexcited state lends itself to an interpretation in terms of a few configurations built from the instantaneous adiabatic single-particle orbitals of each chain, $\{\varphi_{i_q}^{(v)}, \varphi_{i_q}^{(c)}\}$. If we calculate their energies using expression (6.35), we find that, in general, each strand exhibits two pairs of nearly-degenerate states oscillating back and forth between the bands and the gap, as shown in figure 7.8 for the strong coupling regime. Hence, in analogy with the case of a $2\,^1B_u$ photoexcited state in an isolated chain, the symmetric and antisymmetric combinations

$$\begin{aligned} |\chi_{L_q,R_q}^{(v)}\rangle &= \frac{1}{\sqrt{2}}\left(|\varphi_{1_q}^{(v)}\rangle \pm |\varphi_{2_q}^{(v)}\rangle\right), \\ |\chi_{L_q,R_q}^{(c)}\rangle &= \frac{1}{\sqrt{2}}\left(|\varphi_{1_q}^{(c)}\rangle \pm |\varphi_{2_q}^{(c)}\rangle\right) \end{aligned} \tag{7.29}$$

do not change the minima of the electronic energies, and are localised on the left or right sides of the chains (see figure 7.9). A good description of the time-evolving many-body wavefunction requires distributing a hole and an electron over such gap states, instead of merely the HOMOs and LUMOs of each strand. This gives rise

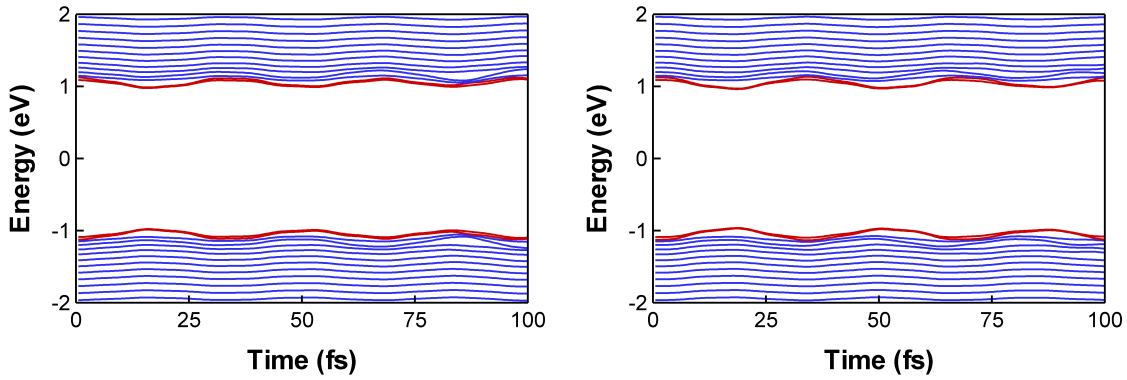

(a) *(b)*

Figure 7.8: Time evolutions of the energies of the instantaneous adiabatic orbitals (close to the band edges), obtained for the first (a) and second (b) strands of a system of two coupled 120*-site* cis*-polyacetylene chains, considering a* $2\,^1B_u$ *photoexcitation initially localised on the first strand and an interchain distance of* 5 Å*. The energies of the gap states are shown in red (note that these constitute sets of two pairs of nearly-degenerate states).*

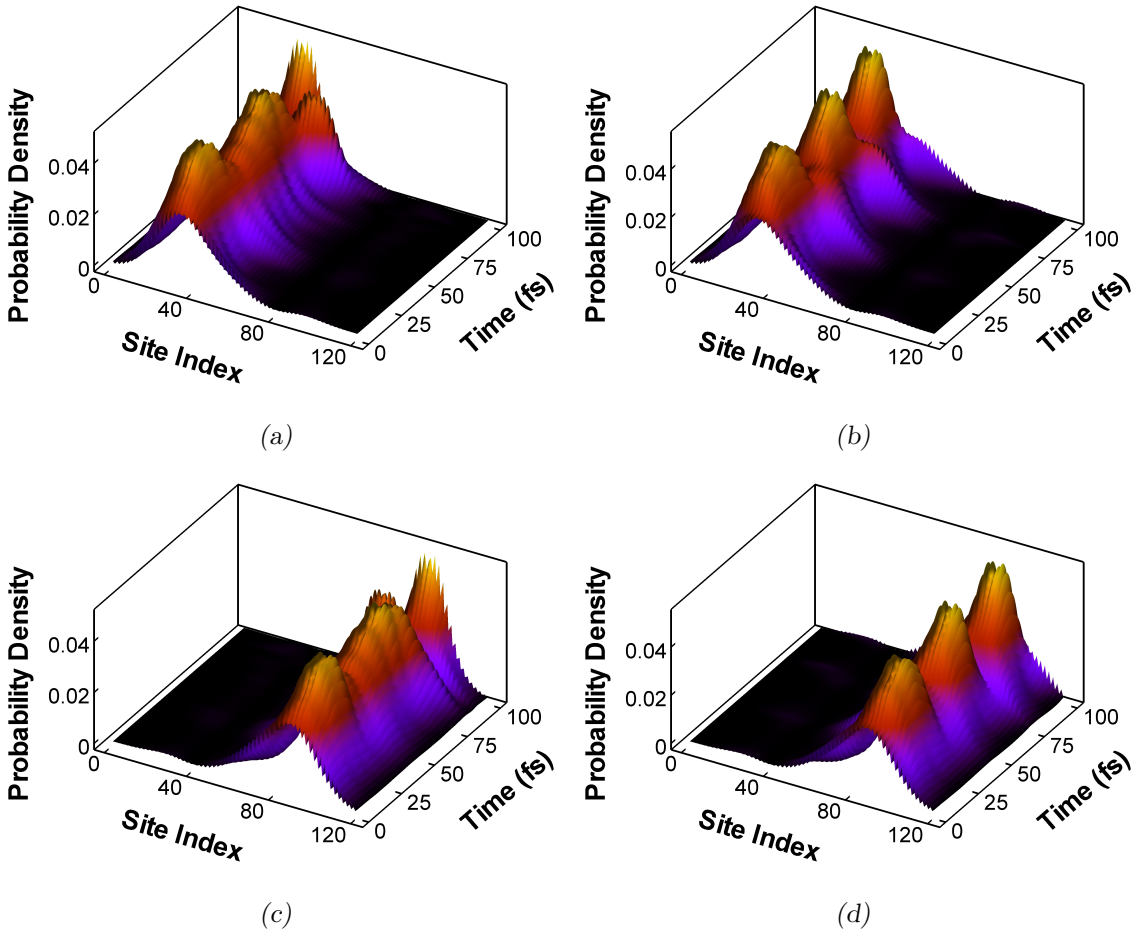

Figure 7.9: Probability densities associated with the symmetric and antisymmetric combinations of the gap states, obtained for the first [(a) and (c)] and second [(b) and (d)] strands of a system of two coupled 120*-site* cis*-polyacetylene chains, considering a* $2\,^1B_u$ *photoexcitation initially localised on the first strand and an interchain distance of* 5 Å*. Such linear superpositions lead to states localised on the left [(a) and (b)] or right [(c) and (d)] sides of the chains.*

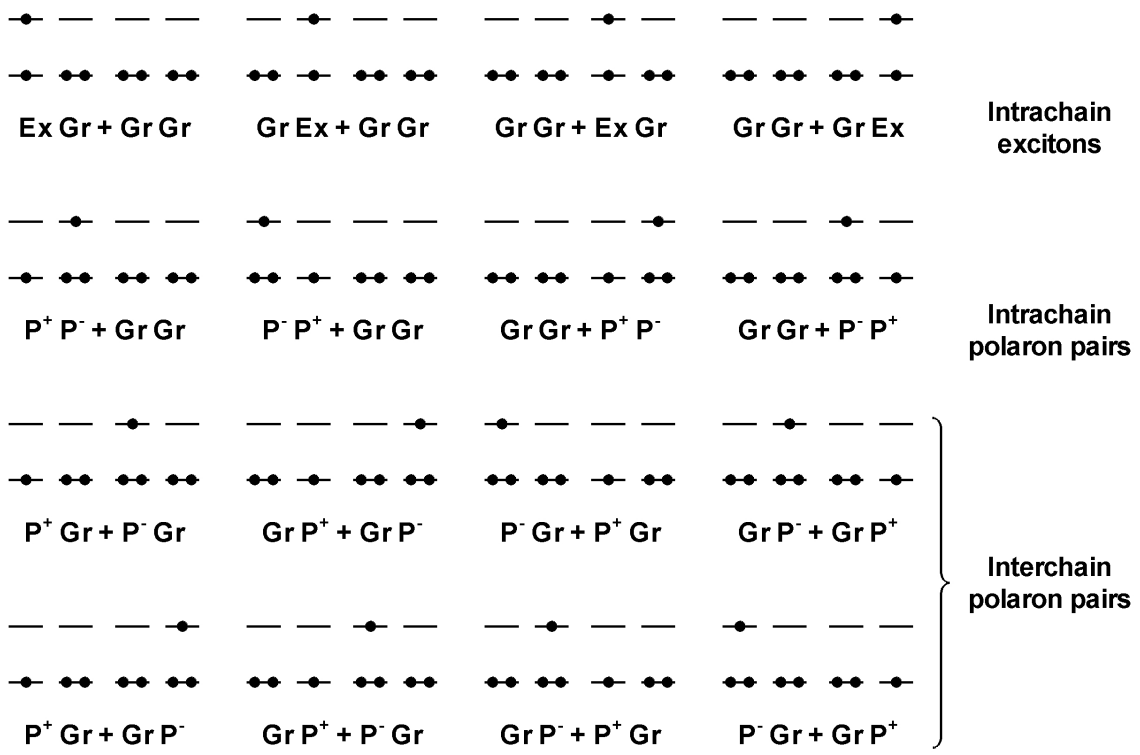

*Figure 7.10: Configurations required to understand the nature of the $2\,^1B_u$ photoexcited state in a system of two coupled polymer chains. These involve combinations of a few species localised on the left and right sides of the different strands: exciton (*Ex*), ground state (*Gr*), hole- or positive polaron (*P^+*) and electron- or negative polaron (*P^-*).*

to 16 possible configurations, depicted in figure 7.10. The emerging species (whose character depends on how the gap states are populated) can be classified as intrachain excitons, as well as intra- or interchain oppositely charged polaron pairs (see figure 7.10). Thus, in this case, the time-evolving wavefunction is approximated by the expansion

$$|\Psi\rangle \approx \sum_x C_x\,|\Phi_x\rangle, \tag{7.30}$$

where the sum runs over the 16 configurations of figure 7.10 (labelled by x), which are built using the valence band states $\varphi_{i_q}^{(v)}$, $i_q = 3, \ldots, N_q/2$, and the necessary orbitals from the sets $\left\{\chi_{L_q}^{(v)}, \chi_{R_q}^{(v)}, \chi_{L_q}^{(c)}, \chi_{R_q}^{(c)}\right\}$.

Figure 7.11 shows the time evolutions of the 16 configurational probabilities, calculated for a system of two coupled 120-site *cis*-polyacetylene chains, considering the same regimes of the interchain coupling strength as before. Notice that, in all

cases, only three species are independent. Indeed, the four curves associated with an exciton or an oppositely charged polaron pair localised on chain one all overlap, and the same happens for those localised on chain two, as well as for the eight curves corresponding to interchain polaron pairs. Also, notice that the 16 contributions sum to well above 70% most of the time, thus confirming the validity of the approximate expansion (7.30). It is clear from the figure that, when the interchain distance is large, the wavefunction is mostly described by a superposition with equal weights of exciton and oppositely charged polarons confined to the first strand. Similarly to what was observed for the $1\,^1B_u$ photoexcited state, in such weak coupling limit,

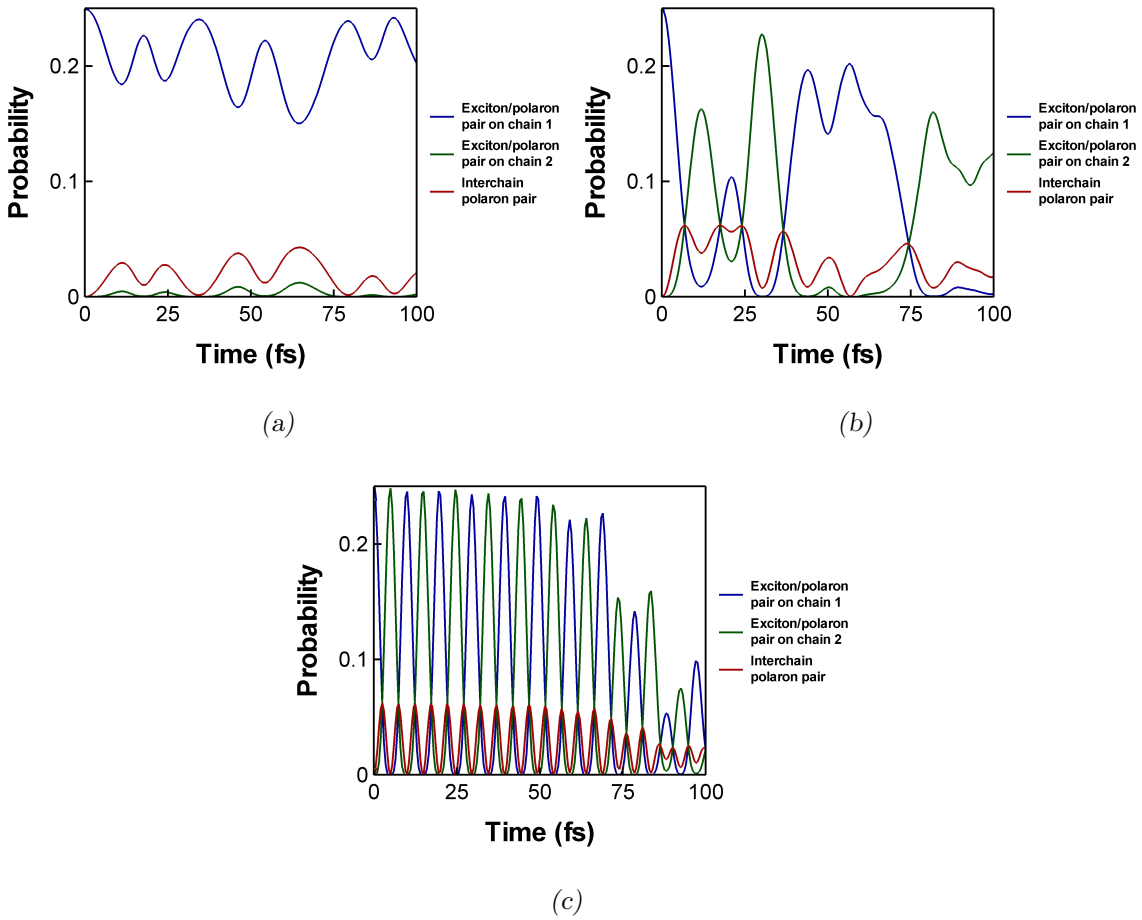

Figure 7.11: Probability of each of the configurations introduced to study the nature of the $2\,^1B_u$ *photoexcited state, obtained for a system of two coupled* 120*-site* cis*-polyacetylene chains, considering three different regimes of the interchain coupling strength: (a) weak coupling (*$d = 15$ Å*), (b) intermediate coupling (*$d = 10$ Å*) and (c) strong coupling (*$d = 5$ Å*). Note that, in all cases, only three species are independent.*

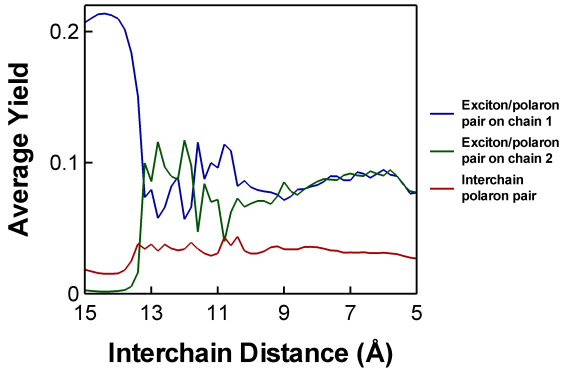

Figure 7.12: Average yields of the configurations introduced to study the nature of the $2\,^1B_u$ *photoexcited state, calculated as a function of interchain distance for a system of two coupled* 120*-site* cis*-polyacetylene chains. Note that only three species are independent.*

the curves exhibit small-amplitude oscillations related to the nonadiabatic mixing of single-particle orbitals with associated phases of different frequencies, but the modulation by the dynamical phase oscillation process is less apparent. As the chains are brought closer together, faster and more pronounced oscillations take over, as ultrafast processes analogous to exciton hopping and dissociation into polaron pairs become increasingly important. In this case, it is the intrachain exciton/polaron pair superposition that can move between chains *as a whole entity*, in addition to being dissociated into interchain polaron pairs. This behaviour is consistent with the findings of section 6.5, where it was shown that the polarons of the superposition are entangled with the exciton and do not behave as free charges. As the interchain coupling strength increases, the dynamics becomes dominated by ultrafast interchain processes, leading to a constant interchange between the three independent species, whose yields oscillate with "periods" of the order of 10 fs.

As discussed in the previous section, the predominance of each configuration over the whole time interval is given by its average yield, which can be calculated using equation (7.28). The results obtained from 51 simulations (up to 100 fs) with the chain separation ranging between 15 and 5 Å are shown in figure 7.12. As before, three distinct regimes of the interchain coupling strength can be clearly identified, although the zone boundaries do not precisely match those observed in the case of a $1\,^1B_u$ photoexcited state. For the longer chain separations ($d \gtrsim$ 13–14 Å), the

$2\,^1B_u$ photoexcitation corresponds to a superposition with equal weights of exciton and oppositely charged polarons localised on the first strand, whose components can reach yields in excess of 20%, giving a total probability of finding the system in any one of them of about 90%. A sharp drop (rise) of the curves associated with an exciton/polaron pair on chain one (two), together with a significant increase of the average yields of interchain polaron pairs, signals the beginning of an intermediate coupling stage. This region also exhibits somewhat wide oscillations of the intrachain curves, as a consequence of the finite nature of the investigated time window. Finally, when the interchain distance is small ($d \lesssim$ 8–9 Å), the yields of the superposition components total some 35% for each strand, while those of oppositely charged interchain polarons sum to about 25%, which agrees well with other theoretical predictions and experimental observations [39, 42, 56]. These results strongly support the decisive role played by interchain interactions in governing ultrafast processes analogous to exciton hopping and dissociation into polaron pairs, which ultimately determine the intra- or interchain character of the species produced upon photoexcitation.

7.4 The $1\,^1B_u$ photoexcited state for chains of different lengths

It is also instructive to investigate how the dynamics of the photoexcited states is changed when the chains have different lengths. As a typical example, we consider a $1\,^1B_u$ photoexcitation in a system of two coupled strands, with $N_1 = 60$ and $N_2 = 120$ sites. The initial conditions are prepared as described in section 7.2, with the different chain lengths being set up. The $1 \rightarrow 1$ excitation is created on the shorter strand, while the longer one remains in the ground state, and the evolution of the coupled system is computed by numerical integration of the equations of motion derived in section 7.1. Figure 7.13 shows the time evolutions of the dimerisation, obtained for the weak and strong coupling limits of the interchain coupling strength. As can be seen, when the interchain distance is large, the asymmetry of the chains has no significant effect. Indeed, similarly to what was found for the symmetric case

of section 7.2, the dynamics exhibits a single lattice distortion confined to the first strand. In the strong coupling regime, on the other hand, the mirror-like pattern observed for the symmetric case at the same chain separation is broken. In this case, the amplitude of the lattice deformation that delocalises to the longer strand is increased, while on the shorter chain the distortion is broader, particularly at later times, and eventually loses its single peak profile.

In order to understand the effect of chain length difference on the nature of the photoexcited state, we can perform the four-state configurational analysis introduced

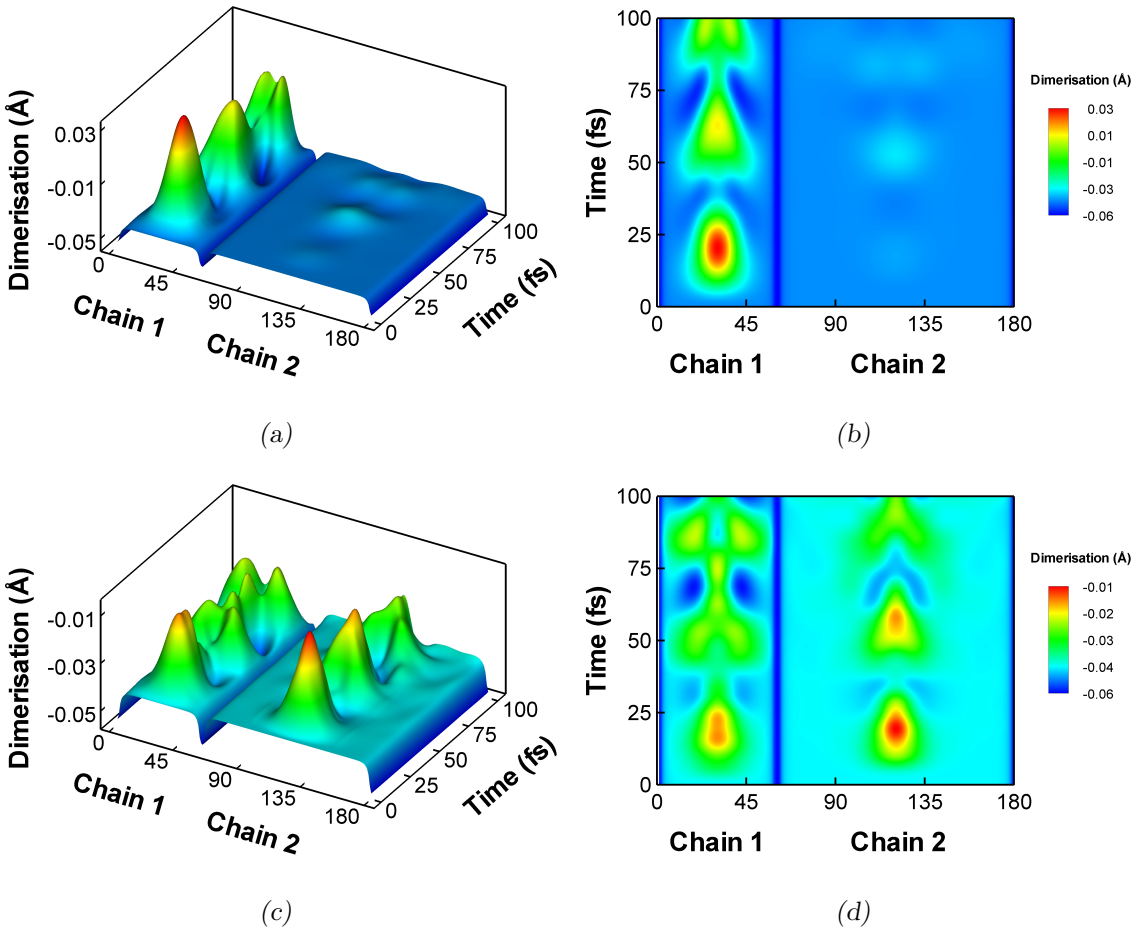

Figure 7.13: Side [(a) and (c)] and top [(b) and (d)] views of the time evolutions of the dimerisation pattern, obtained for a $1\,^1B_u$ *photoexcited state in a system of two coupled* cis*-polyacetylene chains with* $N_1 = 60$ *and* $N_2 = 120$ *sites. The photoexcitation is initially localised on the first chain, and two different regimes of the interchain coupling strength are considered: (a), (b) weak coupling* ($d = 15$ Å) *and (c), (d) strong coupling* ($d = 5$ Å). *Note that, for visualisation purposes, the second chain has been shifted by* 60 *sites.*

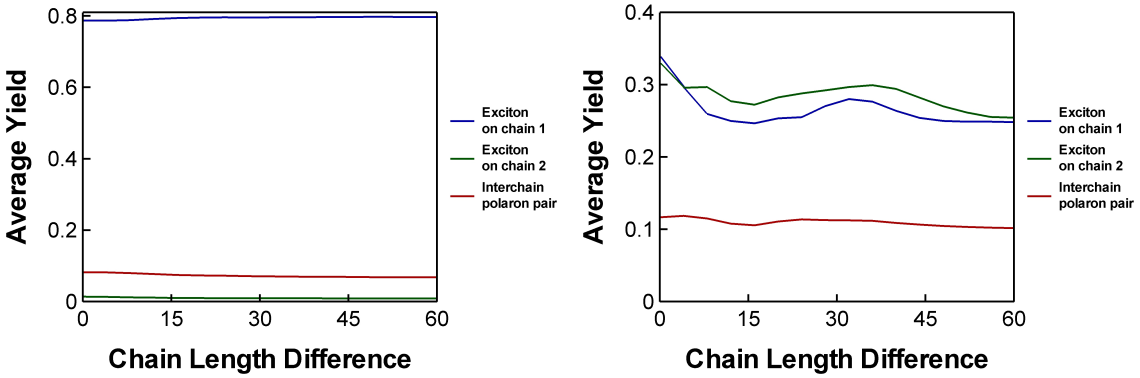

(a) *(b)*

Figure 7.14: Average yields of the configurations introduced to study the nature of the $1\,^1B_u$ *photoexcited state, calculated as a function of chain length difference,* ΔN*, for a system of two coupled* cis*-polyacetylene chains with* $N_1 = 60$ *and* $N_2 = 60 + \Delta N$ *sites. Two different regimes of the interchain coupling strength are considered: (a) weak coupling (*$d = 15$ Å*) and (b) strong coupling (*$d = 5$ Å*). Note that, in both panels, the curves corresponding to interchain polaron pairs overlap.*

in section 7.2. Figure 7.14 shows the average yields of the four configurations for the weak and strong coupling limits of the interchain coupling strength, calculated from sets of 16 simulations (up to 100 fs) with the number of sites of the first chain fixed at $N_1 = 60$ and that of the second one varying in the range $N_2 = 60$–120. In agreement with the results obtained for the dimerisation, in the weak coupling regime the average yields are unchanged as the asymmetry of the chains becomes more pronounced. The dominant configuration is that corresponding to an exciton on the first strand, whose average yield remains constant at a value of about 80%, regardless of the length of the second chain. In contrast, when the chains are brought closer together, the intrachain exciton curves (which overlap for nearly-symmetric cases) quickly split as the second strand becomes longer, with the difference between them reaching values as high as 4% in favour of the exciton localised on the second strand. Hence, in the strong coupling limit, the dominant configuration is that representing an exciton on chain two, which reflects an increased hopping rate towards longer polymer strands, where the exciton energy is lower [61, 66].

Also, note that when the number of sites exceeds a certain threshold value for

both strands ($N_q \gtrsim 100$–120), the effect of chain length difference is undiscernible. Indeed, for such lengths the dynamics of the photoexcited states always resemble that of the symmetric cases, since the band structure properties stabilise after a certain length is reached. This means that, in effect, the system behaves as a set of coupled infinite chains.

7.5 Conclusions

We have studied the effect of interchain interactions on the dynamics of photoexcitations in a prototypical conjugated polymer, by considering a double-strand semiempirical model under different regimes of the interchain coupling strength. Our findings show that interchain interactions have a drastic impact, and are fundamentally important in governing the ultrafast processes of exciton hopping and dissociation into polaron pairs, which ultimately determine the intra- or interchain character of the photogenerated species. In the weak coupling regime, the photoexcitations are essentially confined to the strand where they are created, but as the interchain coupling strength increases, they quite rapidly become delocalised across the two strands. For symmetric systems, mirror-like dimerisation patterns are ultimately obtained in the strong coupling limit. However, as soon as a chain length difference is introduced, the lattice distortion becomes more pronounced on the longer chain, as a consequence of the increased hopping rate towards such longer polymer strands, where the exciton energy is lower [61, 66].

By approximating the time-evolving wavefunction as a sum over a few configurations built from single-particle eigenfunctions localised on different chains, it was possible to quantify the intra- or interchain character of the photoexcited states. Our results show that, when the chains are far apart, the $1\,^1B_u$ photoexcitation corresponds to a polaron-exciton localised on the initially excited strand, while the $2\,^1B_u$ state is an intrachain superposition with equal weights of exciton and oppositely charged polarons. This latter species behaves very much like an exciton, in the sense that it can move between strands as a whole entity, in addition to being dissociated into polaron pairs. As the interchain coupling strength increases, so do

the contributions of exciton-like configurations localised on the chain which was initially kept in the ground state, as well as those associated with interchain polaron pairs. In the strong coupling limit, the yields of intrachain configurations (excitons for the $1\,^1B_u$ state, or exciton/polaron pair superpositions for the $2\,^1B_u$ photoexcitation) total some 35% for each strand, while those of oppositely charged interchain polarons sum to about 25%. Since the $1\,^1B_u$ and $2\,^1B_u$ photoexcitations have similar energies and transition dipole moments [43, 45] and, as shown in section 6.5, the polarons of the intrachain superpositions do not behave as free charges, we can conclude that the charge carrier photogeneration yield varies between nearly zero in the weak coupling regime up to a maximum of about 25% in the strong coupling limit and, as such, depends critically on the strength of interchain interactions. This is in agreement with available experimental evidence [39–42], as well as with other theoretical studies [56].

Chapter 8

Charge transfer dynamics at donor/acceptor interfaces

8.1 Equations of motion

In this chapter, we apply the various methodological tools presented in part II to the study of charge transfer dynamics at donor/acceptor interfaces. As discussed in section 3.5, the photophysics of polymer heterojunctions may be simulated by considering a system of two parallel chains of different materials, described by the Hamiltonian

$$\begin{aligned}\hat{H} = &- \sum_{q,i_q,\sigma} t_{i_q} \left(\hat{c}^\dagger_{i_q\sigma}\,\hat{c}_{i_q+1,\sigma} + \hat{c}^\dagger_{i_q+1,\sigma}\,\hat{c}_{i_q\sigma}\right) - t_\perp \sum_{\langle i_1,i_2\rangle,\sigma} \left(\hat{c}^\dagger_{i_1\sigma}\,\hat{c}_{i_2\sigma} + \hat{c}^\dagger_{i_2\sigma}\,\hat{c}_{i_1\sigma}\right) + \\ &+ \sum_{q,i_q} U_q \left(\hat{n}_{i_q\uparrow} - \frac{1}{2}\right)\left(\hat{n}_{i_q\downarrow} - \frac{1}{2}\right) + \frac{1}{2} {\sum_{q,q',i_q,j_{q'}}}' v_{i_q j_{q'}} \left(\hat{n}_{i_q} - 1\right)\left(\hat{n}_{j_{q'}} - 1\right) + \\ &+ \sum_{q,i_q} \epsilon_{i_q}\,\hat{n}_{i_q} + \sum_{q,i_q} \frac{p^2_{i_q}}{2M_q} + \sum_{q,i_q} \frac{K_q}{2}\left(u_{i_q+1} - u_{i_q}\right)^2.\end{aligned} \tag{8.1}$$

In comparison with the coupled-chain model used in the previous chapter, the above expression introduces chain-dependent parameters and onsite energies, ϵ_{i_q}, which, when adequately defined, can reproduce the energy offset characteristic of the band structure at the interface between two different compounds (see figure 8.1). As before, i_q runs over sites of chain q ($q = 1, 2$, hereafter respectively 'donor', 'acceptor'), the symbol $\sum_{\langle i_1,i_2\rangle}$ means that the sum is restricted to pairs of neighbouring sites in

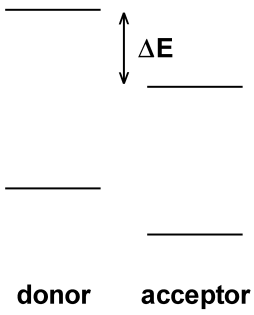

Figure 8.1: Schematic representation of the band structure profile typical of a donor/acceptor interface, with an energy offset, ΔE, between the conduction band edges.

the opposite strands, $\sum'$ is used to indicate that the onsite terms $v_{i_q i_q}$ are excluded from the summation, and the intrachain hopping integral, t_{i_q}, is given by

$$t_{i_q} = t_{0_q} - \alpha_q \left(u_{i_q+1} - u_{i_q}\right) + (-1)^{i_q+1} t_{\mathrm{e}_q}. \tag{8.2}$$

In principle, in order to account for possible interfacial effects, it should be necessary to define a new set of parameters to calculate the interchain quantities $t_\perp$ and $v_{i_q j_{q'}}$ (with $q \neq q'$). However, it is convenient to rely only on the sets of parameters used to describe the polymer chains in isolated form. In this spirit, we assume that arithmetic averages of the donor and acceptor parameters are appropriate, and write the interchain transfer integral, $t_\perp$, and the Ohno potential, $v_{i_q j_{q'}}$, respectively as

$$\begin{aligned} t_\perp &= \frac{\bar{t}_0}{10} \exp\left(1 - \frac{d}{5}\right), \\ v_{i_q j_{q'}} &= \frac{\bar{U}_{qq'}}{\sqrt{1 + \left(\bar{\beta}_{qq'}\, r_{i_q j_{q'}} / \bar{r}_{0_{qq'}}\right)^2}}, \end{aligned} \tag{8.3}$$

where the interchain distance, d, is expressed in angstroms, and

$$\begin{aligned} \bar{t}_0 &= \frac{t_{0_1} + t_{0_2}}{2}, \\ \bar{U}_{qq'} &= \frac{U_q + U_{q'}}{2}, \\ \bar{\beta}_{qq'} &= \frac{\beta_q + \beta_{q'}}{2}, \\ \bar{r}_{0_{qq'}} &= \frac{r_{0_q} + r_{0_{q'}}}{2}. \end{aligned} \tag{8.4}$$

The derivation of the equations of motion, within the framework of the Ehrenfest molecular dynamics and the multiconfigurational time-dependent Hartree-Fock

methods, follows closely that of section 7.1. The result for the nuclear degrees of freedom reads

$$M_{q'}\,\ddot{u}_{k_{q'}} = F_{k_{q'}}. \tag{8.5}$$

The total force, $F_{k_{q'}}$, for atoms $k_{q'} = 2, \ldots, N_{q'} - 1$ (we recall that the end sites for both chains are kept fixed), is given by the sum of the contributions

$$F^{(\mathrm{n})}_{k_{q'}} = K_{q'}\,(u_{k_{q'}+1} + u_{k_{q'}-1} - 2\,u_{k_{q'}}) - \sum_{q,i_q} d_{i_q k_{q'}} \tag{8.6}$$

and

$$\begin{aligned} F^{(\mathrm{e})}_{k_{q'}} = & \sum_{\mu} n^{\mu} \left[\sum_{q,i_q} \left(P^{\mu}_{i_q i_q} + P^{\mu}_{k_{q'} k_{q'}}\right) d_{i_q k_{q'}} + 2\,\alpha_{q'} \left(\mathrm{Re}\, P^{\mu}_{k_{q'},k_{q'}+1} - \mathrm{Re}\, P^{\mu}_{k_{q'},k_{q'}-1}\right)\right] - \\ & - \frac{1}{2} \sum_{\mu,\nu} n^{\mu}\, n^{\nu} \sum_{q,i_q} \Big[a^{\mu\nu} \left(P^{\mu}_{i_q i_q}\, P^{\nu}_{k_{q'} k_{q'}} + P^{\mu}_{k_{q'} k_{q'}}\, P^{\nu}_{i_q i_q}\right) - \\ & \qquad - b^{\mu\nu}\, \mathrm{Re}\left(P^{\mu}_{k_{q'} i_q}\, P^{\nu}_{i_q k_{q'}}\right)\Big]\, d_{i_q k_{q'}}, \end{aligned} \tag{8.7}$$

with

$$\begin{aligned} d_{i_q k_{q'}} &= \frac{\left(\bar{\beta}_{qq'}/\bar{r}_{0_{qq'}}\right)^2 (x_{i_q} - x_{k_{q'}})}{1 + \left(\bar{\beta}_{qq'}\, r_{i_q k_{q'}}/\bar{r}_{0_{qq'}}\right)^2}\, v_{i_q k_{q'}}, \\ P^{\mu}_{i_q k_{q'}} &= \sum_{j_\mu} C_{i_q j_\mu}\, C^{*}_{k_{q'} j_\mu}. \end{aligned} \tag{8.8}$$

The intersite distances, $r_{i_q k_{q'}}$, and coordinates along each chain, x_{i_q}, are calculated as in the previous chapter [equations (7.7) and (7.8)], while $C_{i_q j_\mu}$ denote the usual LCAO expansion coefficients.

The equations of motion are completed by solving the time-dependent wave equation for the electronic degrees of freedom, via the multiconfigurational time-dependent Hartree-Fock approximation. In the case of general open-shell states, we have

$$\mathrm{i}\,\hbar\,\dot{C}_{i_q k_\mu} = \sum_{q',j_{q'}} R_{i_q j_{q'}}\, C_{j_{q'} k_\mu}, \tag{8.9}$$

where the unified coupling matrix is expressed in the atomic orbitals basis set as

$$R_{i_q j_{q'}} = \sum_{\substack{\mu,\nu \\ (n^\mu \neq n^\nu)}} \sum_{q'',q'''} \sum_{k_{q''},l_{q'''}} P^{\nu}_{i_q k_{q''}}\, \frac{n^{\nu} F^{\nu}_{k_{q''} l_{q'''}} - n^{\mu} F^{\mu}_{k_{q''} l_{q'''}}}{n^{\nu} - n^{\mu}}\, P^{\mu}_{l_{q'''} j_{q'}}, \tag{8.10}$$

and the Fock matrix for shell μ reads

$$F^{\mu}_{i_q j_{q'}} = -\Bigg\{ \left[\frac{U_q}{2} + \sum_{q'',k_{q''}}{}' v_{i_q k_{q''}} \right] \delta_{i_q j_{q'}} + t_{i_q}\, \delta_{i_q+1, j_{q'}} + t_{i_q-1}\, \delta_{i_q-1, j_{q'}} - \\ - \epsilon_{i_q}\, \delta_{i_q j_{q'}} - \left[\sum_{\nu} \sum_{q'',k_{q''}} n^{\nu}\, a^{\mu\nu} P^{\nu}_{k_{q''} k_{q''}}\, v_{i_q k_{q''}} \right] \delta_{i_q j_{q'}} \Bigg\} \delta_{qq'} - \\ - t_{\perp}\, \delta_{i_q-(N_q-N_{q'})/2, j_{q'}} \left(1 - \delta_{qq'}\right) - \frac{1}{2} \sum_{\nu} n^{\nu}\, b^{\mu\nu} P^{\nu}_{i_q j_{q'}}\, v_{i_q j_{q'}}. \tag{8.11}$$

As discussed in the previous chapters, the coupled set of differential equations (8.5) and (8.9) can be efficiently integrated numerically using an eighth-order Runge-Kutta method with adaptive step-size control [125].

8.2 Band offset effect on the dynamics of the $1\,^1B_u$ photoexcited state

The simplest way to obtain a band structure profile as depicted in figure 8.1, with an energy offset at the interface between two phases, is to set the onsite energies to zero for all sites of the donor chain, while for the acceptor chain they are all lowered by ΔE. In this section, we consider only the effect of such a *band offset parameter*, and choose the remaining model parameters (for both strands) as those appropriate to describe *cis*-polyacetylene using the SSH + PPP model (listed in table 6.1). As an illustrative example, we take the case of a $1\,^1B_u$ photoexcitation in a system of two coupled 120-site *cis*-polyacetylene chains, with a band offset of $\Delta E = 0.3$ eV. As described in section 7.2, the initial conditions are prepared by treating the chains independently. The ionic momenta are set to zero, and the lattice displacements are obtained by minimising the ground state potential energy surfaces. To determine the orbital coefficients, a $1 \rightarrow 1$ excitation (i.e., HOMO $\rightarrow$ LUMO) is created on the donor phase, while the acceptor remains in the ground state. The interchain coupling is then turned on, the appropriate onsite energies are set up, and the initial conditions are propagated through the numerical integration of the equations of motion given in the previous section.

Figure 8.2 shows the time evolutions of the dimerisation, calculated using equa-

tion (7.25) for two different regimes of the interchain coupling strength. As can be seen, when the chains are far apart ($d = 15$ Å), the introduction of a band offset between them has no noticeable effect. Indeed, the dynamics is comparable to that obtained for the weak coupling case of section 7.2, with a single lattice distortion confined to the first strand (the donor). In the strong coupling regime, on the other hand, the symmetric pattern characteristic of the case of levelled bands at the same chain separation ($d = 5$ Å) is lost. In this case, most of the weight of the lattice deformation is retained on the donor phase. Additionally, the distortions on both

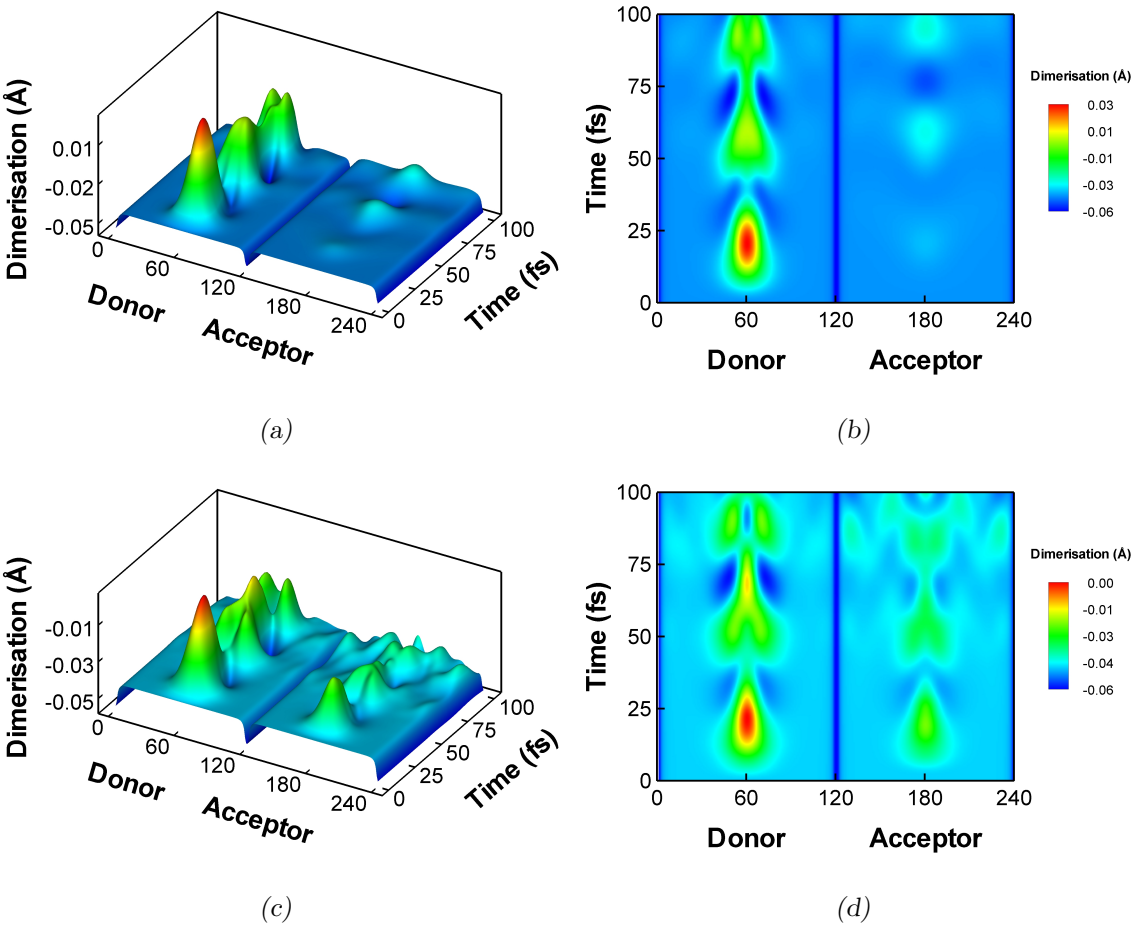

Figure 8.2: Side [(a) and (c)] and top [(b) and (d)] views of the time evolutions of the dimerisation pattern, obtained for a $1\,^1B_u$ photoexcited state in a system of two coupled 120-site cis-polyacetylene chains with a band offset of $\Delta E = 0.3$ eV. The photoexcitation is initially localised on the donor chain, and two different regimes of the interchain coupling strength are considered: (a), (b) weak coupling ($d = 15$ Å) and (c), (d) strong coupling ($d = 5$ Å). Note that, for visualisation purposes, the acceptor chain has been shifted by 120 sites.

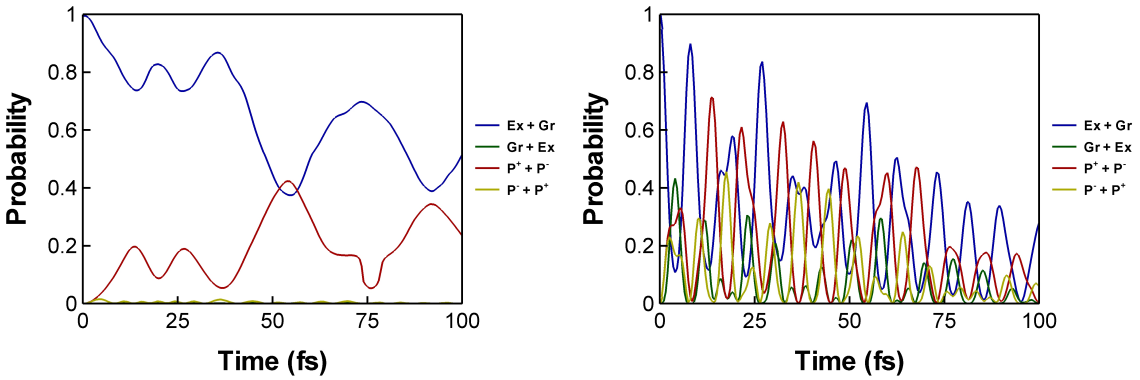

Figure 8.3: Probability of each of the configurations introduced in the previous chapter to study the nature of the $1\,^1B_u$ *photoexcited state, obtained for a system of two coupled* 120*-site cis-polyacetylene chains with a band offset of* $\Delta E = 0.3$ eV*. Two different regimes of the interchain coupling strength are considered: (a) weak coupling (*$d = 15$ Å*) and (b) strong coupling (*$d = 5$ Å*).*

strands progressively become broader, and eventually lose their initial single peak profiles, an effect that is particularly drastic for the acceptor chain.

It is also instructive to perform the four-state configurational analysis introduced in section 7.2. Figure 8.3 shows the time evolutions of the four configurational probabilities, obtained for the same system considered before, by taking the weak and strong coupling limits of the interchain coupling strength. The first thing to notice is that the degeneracy of the curves associated with interchain polaron pairs is lifted in favour of the configuration produced via electron transfer from the donor to the acceptor (i.e., $\mathrm{P}^+ + \mathrm{P}^-$, with a hole-polaron localised on the donor chain and an electron-polaron on the acceptor chain). In the weak coupling regime, the probability of such a configuration slowly builds up, at the same time as the curve corresponding to an exciton on the donor strand decreases. It is seen that these two states are sufficient to describe the whole dynamics, even though, on average, the yield of the charged species configuration is not as important, in agreement with the results obtained for the dimerisation. In the strong coupling limit, the four curves exhibit fast oscillations, all with a significant amplitude at the early stages of the dynamics. However, in contrast to the weak coupling case, the quality of the approximation deteriorates considerably with time, and thus the four-state model

is insufficient to describe the full extent of the band offset effect.

A better understanding requires adding higher-order intrachain excitons and interchain polaron pairs. In particular, it is necessary to further consider the many-body states depicted in figure 8.4, which are produced by transitions between the HOMO and LUMO of the donor and the acceptor orbitals of the same symmetry (a_u or b_g) that are closest to the band edges, HOMO $-$ 2 and LUMO + 2. Taking such configurations into account, the approximation to the time-evolving many-body wavefunction reads

$$|\Psi\rangle \approx |\Psi'\rangle + C_{\mathrm{Gr+Ex_3}}\,|\Phi_{\mathrm{Gr+Ex_3}}\rangle + C_{\mathrm{P^+ + P_3^-}}\,|\Phi_{\mathrm{P^+ + P_3^-}}\rangle + C_{\mathrm{P^- + P_3^+}}\,|\Phi_{\mathrm{P^- + P_3^+}}\rangle, \quad (8.12)$$

where Ψ' is given by expression (7.26) and the higher-order states, $\Phi_{\mathrm{Gr+Ex_3}}$, $\Phi_{\mathrm{P^+ + P_3^-}}$ and $\Phi_{\mathrm{P^- + P_3^+}}$, are built from the appropriate instantaneous adiabatic single-particle levels of each strand, which are obtained as discussed in the previous chapter. Also, notice that, to simplify the notation, the excitonic configuration $\mathrm{Gr} + \mathrm{Ex_3}$ has been defined as consisting of three different states (its configurational probability is given by the sum of the individual components, see figure 8.4).

Figure 8.5 shows the average yields of the many-body states involved in the above approximation, calculated via equation (7.28) for the weak and strong coupling limits

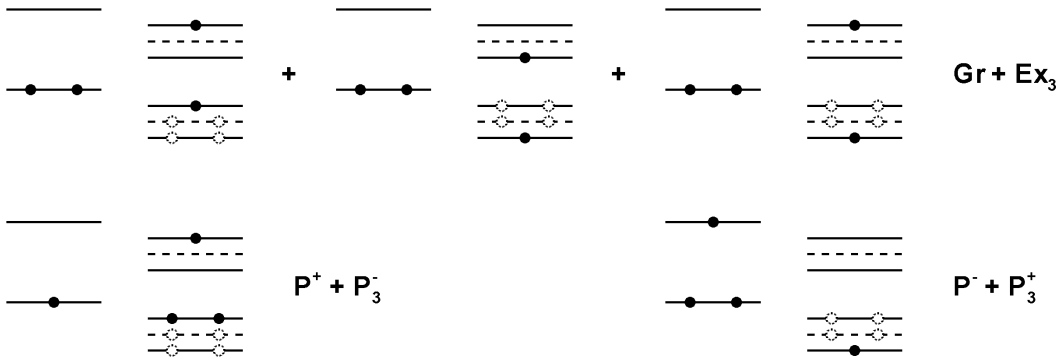

Figure 8.4: Higher-order configurations required to understand the nature of the $1\,^1B_u$ *photoexcited state in a donor/acceptor system. These involve combinations of the usual species localised on the donor strand – ground state (*Gr*), hole-polaron (*$\mathrm{P^+}$*) and electron-polaron (*$\mathrm{P^-}$*) – with higher-order states localised on the acceptor, of excitonic (*$\mathrm{Ex_3}$*) and polaronic (*$\mathrm{P_3^-}$ *and* $\mathrm{P_3^+}$*) character. These latter species are obtained by populating the acceptor orbitals that are closest to, and possess the same symmetry as the band edges,* HOMO $-$ 2 *and* LUMO + 2.

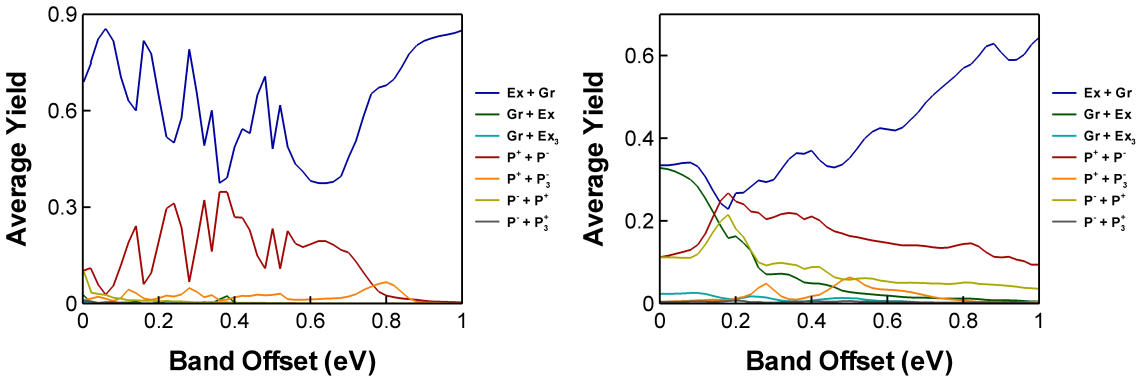

Figure 8.5: Average yields of the configurations introduced to study the nature of the $1\,^1B_u$ *photoexcited state (including higher-order configurations), calculated as a function of band offset for a system of two coupled* 120*-site* cis*-polyacetylene chains. Two different regimes of the interchain coupling strength are considered: (a) weak coupling (*$d = 15$ Å*) and (b) strong coupling (*$d = 5$ Å*).*

of the interchain coupling strength, from sets of 51 simulations (up to 100 fs) with the band offset varying in the range 0–1 eV. As can be seen, in both cases there is an optimal value of the band offset for which the charge transfer process is maximised. In the weak coupling regime, the optimal point occurs at a band offset of about $\Delta E = 0.4$ eV. Even for such a large interchain distance, the yields of oppositely charged polarons total some 35%, a value considerably higher than that observed in the case of levelled bands. However, the configuration corresponding to an exciton localised on the donor strand is always the most prevalent one. In the strong coupling limit, the charge transfer process is maximised at around $\Delta E = 0.2$ eV. In this region, the yields of the polaronic configurations sum to about 50%, and the dominant species is the interchain polaron pair $\mathrm{P}^+ + \mathrm{P}^-$. The predominance of such a species is consistent with a charge generation mechanism governed by a one-step electron transfer from the donor to the acceptor. However, since the configuration associated with an exciton on the acceptor strand also carries a significant yield, we cannot exclude a contribution arising from a two-step process, whereby hole transfer to the donor follows exciton hopping to the acceptor, as discussed in section 2.4. Finally, it is seen that the importance of the higher-order states tends to increase with the band offset, particularly in the case of the interchain polaron pair $\mathrm{P}^+ + \mathrm{P}_3^-$,

whose average yield can reach values close to 10%. This can be understood as a consequence of the increased electronic transition probability as the higher-lying acceptor orbital becomes more closely matched to the LUMO of the donor. The presence of a peak at around $\Delta E = 0.3$ eV also suggests that such a species is responsible for the broadening observed in the results obtained for the dimerisation in the strong coupling regime, since the degree of delocalisation typically increases with the order of the excitation [43, 131].

8.3 The $1\,^1B_u$ photoexcited state for chains with different model parameters

We now turn to the case in which the polymer strands are described by different sets of parameters. As in the previous section, we consider a $1\,^1B_u$ photoexcitation in a system of two coupled 120-site chains, separated by a distance of 15 or 5 Å. Additionally, a band offset of $\Delta E = 0.5$ eV is introduced, in order to obtain a band structure profile characteristic of a donor/acceptor interface. For the donor phase, the model parameters are taken as the SSH + PPP choices to describe *cis*-polyacetylene (see table 6.1). For the acceptor, the same is done for all but one of the parameters, which is varied in a range of values typical of conjugated polymers [44, 45]. In particular, we focus on the effect of varying the parameters (one at a time) in the set $\{K, t_0, \alpha, U, \beta\}$. The initial conditions are prepared as described in the previous section, with the different model parameters being set up, and the evolution of the coupled system is computed by numerical integration of the equations of motion given in section 8.1.

Figures 8.6 through 8.10 show the average yields of the configurations introduced to describe the $1\,^1B_u$ photoexcitation (including higher-order states) for the weak and strong coupling limits of the interchain coupling strength, calculated from sets of 51 simulations (up to 100 fs) in which one of the key parameters listed above is varied for the acceptor strand. As can be seen, in all cases the maximum of the charge carrier photogeneration yield is not significantly different from the value obtained when the model parameters are equal for both chains and the same band offset is

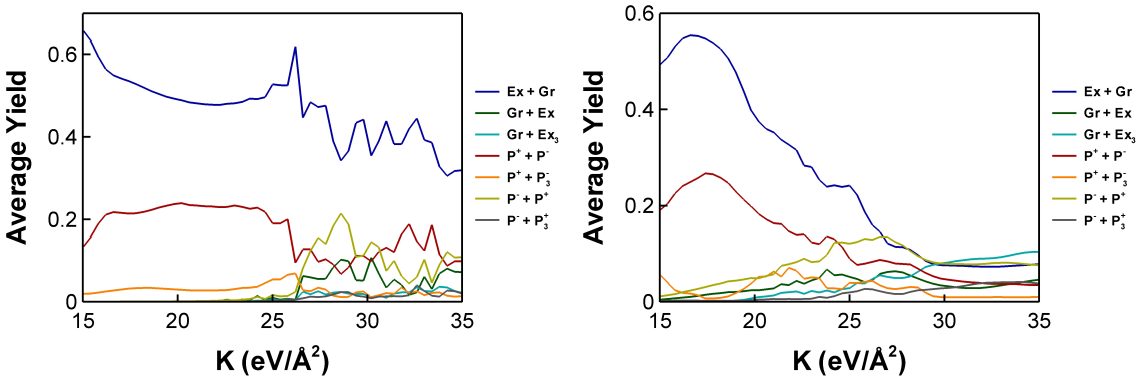

(a) *(b)*

Figure 8.6: Average yields of the configurations introduced to study the nature of the $1\,^1B_u$ *photoexcited state (including higher-order configurations), obtained by varying the parameter* K *for the acceptor in a system of two coupled* 120*-site chains with a band offset of* $\Delta E = 0.5$ eV*. The remaining model parameters are taken as those appropriate for* cis*-polyacetylene, and two different regimes of the interchain coupling strength are considered: (a) weak coupling (*$d = 15$ Å*) and (b) strong coupling (*$d = 5$ Å*).*

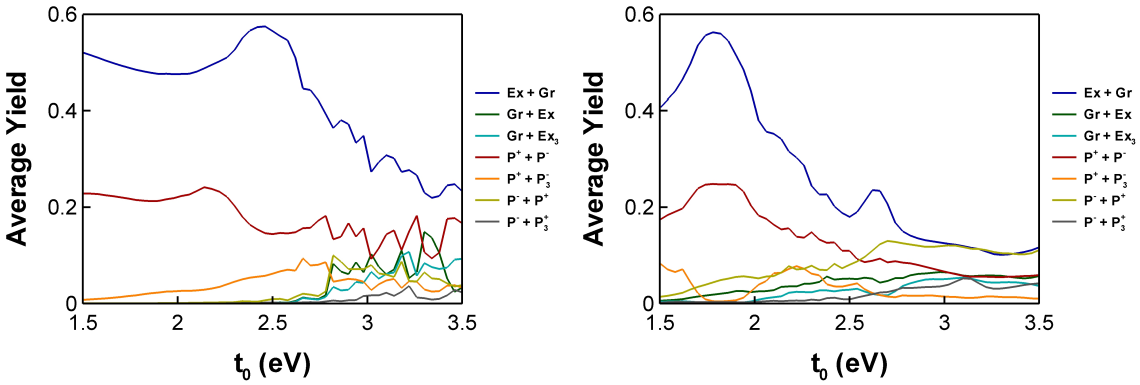

(a) *(b)*

Figure 8.7: Average yields of the configurations introduced to study the nature of the $1\,^1B_u$ *photoexcited state (including higher-order configurations), obtained by varying the parameter* t_0 *for the acceptor in a system of two coupled* 120*-site chains with a band offset of* $\Delta E = 0.5$ eV*. The remaining model parameters are taken as those appropriate for* cis*-polyacetylene, and two different regimes of the interchain coupling strength are considered: (a) weak coupling (*$d = 15$ Å*) and (b) strong coupling (*$d = 5$ Å*).*

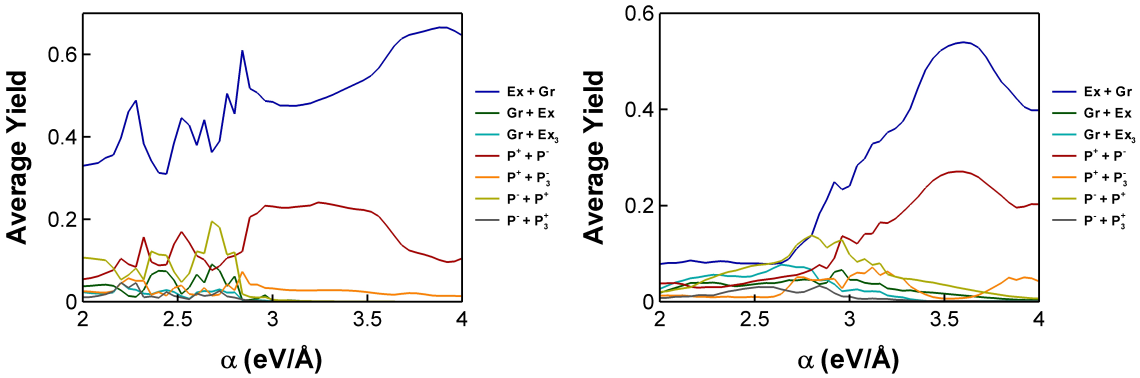

(a) (b)

Figure 8.8: Average yields of the configurations introduced to study the nature of the $1\,^1B_u$ photoexcited state (including higher-order configurations), obtained by varying the parameter α for the acceptor in a system of two coupled 120-site chains with a band offset of $\Delta E = 0.5$ eV. The remaining model parameters are taken as those appropriate for cis*-polyacetylene, and two different regimes of the interchain coupling strength are considered: (a) weak coupling ($d = 15$ Å) and (b) strong coupling ($d = 5$ Å).*

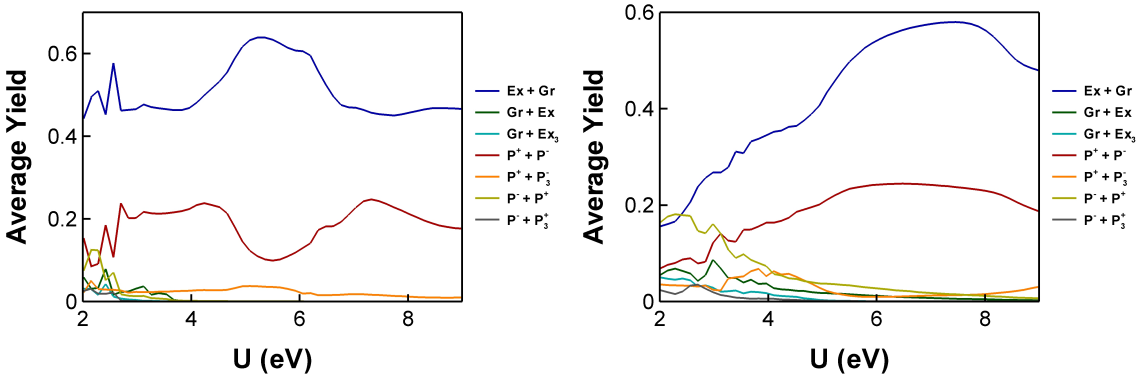

(a) (b)

Figure 8.9: Average yields of the configurations introduced to study the nature of the $1\,^1B_u$ photoexcited state (including higher-order configurations), obtained by varying the parameter U for the acceptor in a system of two coupled 120-site chains with a band offset of $\Delta E = 0.5$ eV. The remaining model parameters are taken as those appropriate for cis*-polyacetylene, and two different regimes of the interchain coupling strength are considered: (a) weak coupling ($d = 15$ Å) and (b) strong coupling ($d = 5$ Å).*

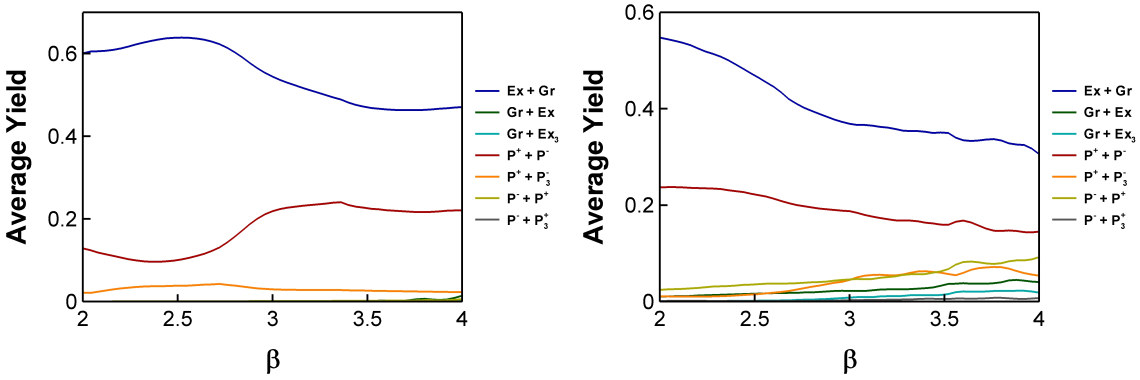

Figure 8.10: Average yields of the configurations introduced to study the nature of the $1\,^1B_u$ photoexcited state (including higher-order configurations), obtained by varying the parameter β for the acceptor in a system of two coupled 120-site chains with a band offset of $\Delta E = 0.5$ eV. The remaining model parameters are taken as those appropriate for cis*-polyacetylene, and two different regimes of the interchain coupling strength are considered: (a) weak coupling ($d = 15$ Å) and (b) strong coupling ($d = 5$ Å).*

considered. Indeed, even though the optimal points may occur when there is a large mismatch between the donor and acceptor parameters (e.g., for U such mismatch is around 40–50%, see figure 8.9), there is only a marginal improvement in the total yields of interchain polaron pairs, of up to 5%. These results suggest that the most important parameter in determining the extent of the charge transfer process is the band offset at the donor/acceptor interface. It is also noteworthy that, in general, the results exhibit similar patterns. Two regions can be distinguished in all cases, except when varying β. One of the regions, which occurs (for instance) when $K \lesssim 25$ eV/Å^2, corresponds to a simple picture where the excitonic configuration Ex + Gr (i.e., with an exciton localised on the donor) and the interchain polaron pair $\mathrm{P}^+ + \mathrm{P}^-$ are sufficient to characterise the photoexcitation. The other region (visible, e.g., for $t_0 \gtrsim 2.5$ eV) is a more complex one, that involves a significant contribution of most, if not all, of the states used to approximate the wavefunction. In particular, for the strong coupling regime the trend is to level the average yields of all the configurations. In such region, the higher-order states acquire an increased importance and, in some cases, it would even be beneficial to include additional ones,

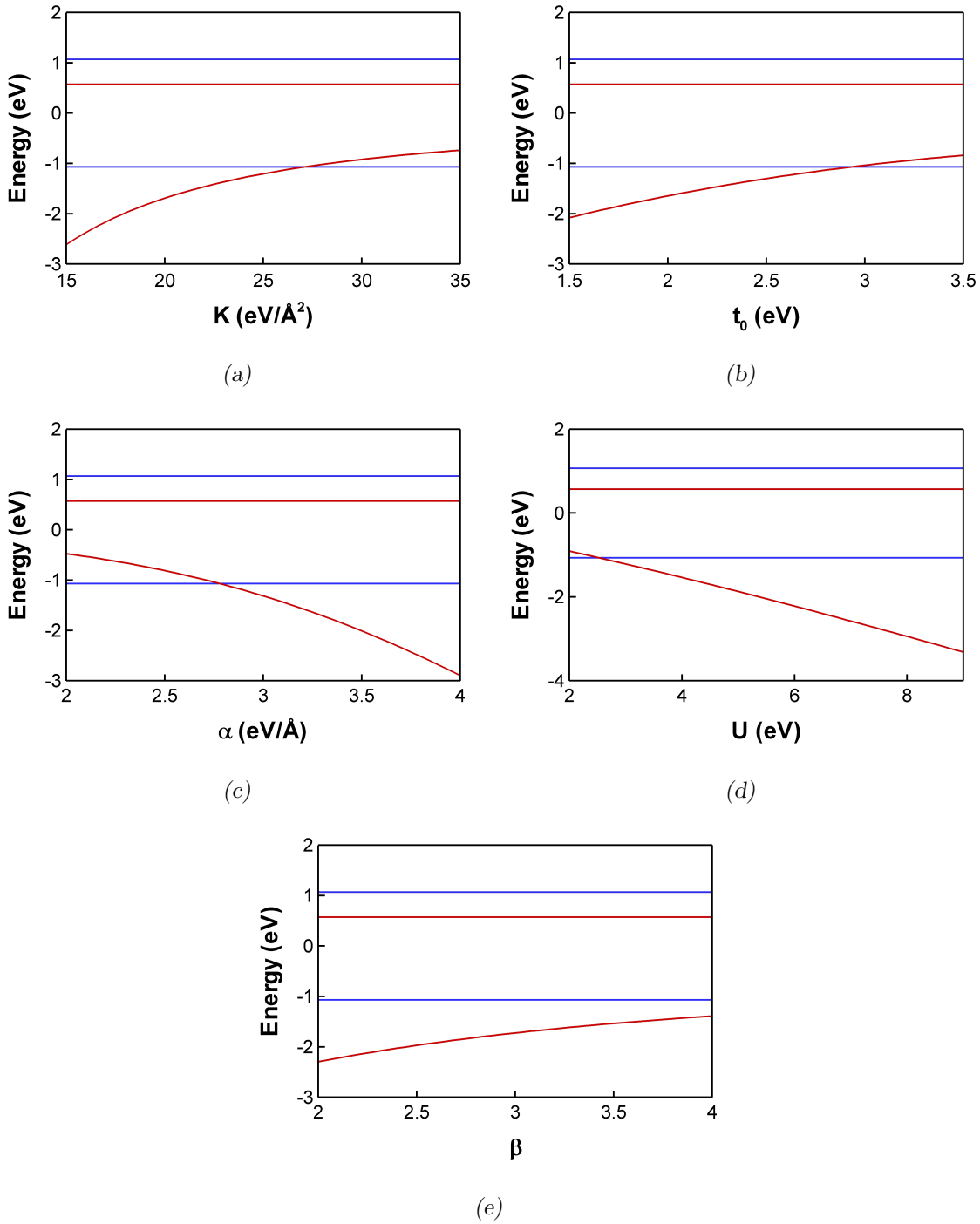

Figure 8.11: Band structure profiles obtained for the ground state of a system of two coupled 120*-site chains with a band offset of* $\Delta E = 0.5$ eV*, by varying the parameters* K *(a),* t_0 *(b),* α *(c),* U *(d) and* β *(e) for the acceptor chain. In all cases, the model parameters that are kept fixed are taken as those appropriate for* cis*-polyacetylene. The energies of the* HOMO *and* LUMO *of the donor strand are shown in blue, while the red lines correspond to those of the acceptor.*

e.g., for $\alpha \lesssim 2.5$ eV/Å in the strong coupling limit [see figure 8.8(b)]. The higher-order configuration Gr + Ex_3 is especially important: its average yield can reach values of about 10% and it can become the most predominant of all configurations, as can be seen in figure 8.6(b). Additionally, there is a reversal of the roles played by the interchain polaron pairs $P^+ + P^-$ and $P^- + P^+$, with the latter generally becoming the most important polaronic configuration, and even the most prevalent of all, as shown in figure 8.9(b).

In order to understand what underlies such patterns, it is instructive to compare the results of figures 8.6 through 8.10 with the band structure profiles obtained for the ground state under the same conditions, which are shown in figure 8.11. As can be seen for nearly all cases, in the vicinity of the zone boundaries observed for the average yields, the HOMO of the acceptor crosses above that of the donor. When the energy difference between the HOMOs is lower than the band offset, electronic transitions involving orbitals close to the valence band edges become more favourable, which explains the increase of the yields of higher-order states, as well as the reversal of the predominance of the interchain polaron pairs $P^+ + P^-$ and $P^- + P^+$. Also, as shown in figure 8.11(e), for the values of β under consideration there is no such crossing, which leads to a single region where the transition between the LUMOs of the donor and acceptor chains is the most likely one, and thus the $1\,^1B_u$ photoexcitation is largely described by the configurations Ex+Gr and P^++P^-. These results indicate that, for a donor/acceptor system, the shape of the (ground state) band structure profile can be used to predict, at least qualitatively, the nature of the species produced upon photoexcitation.

8.4 Conclusions

We have studied the charge transfer dynamics at donor/acceptor interfaces, by varying several key parameters of a π-electron model with interchain interactions. Our findings suggest that the dynamics of photoexcitations in a polymer heterojunction is determined by the shape of the ground state band structure profile. The most important parameter in predicting the extent of the charge transfer process is the

band offset at the donor/acceptor interface. The precise value that maximises the charge transfer depends critically on the strength of interchain interactions. Our results show that the total yield of oppositely charged interchain polarons is increased in comparison with the case of levelled bands, approaching 35% in the weak coupling regime and about 50% in the strong coupling limit. While these figures are consistent with the experimentally observed enhancement of the charge carrier photogeneration yield in certain polymer/fullerene composites [135], the studied model is insufficient to explain most technologically relevant cases [30–32, 136], for which the charge transfer is much more complete.

When the chain separation is small, we find that, in the vicinity of the optimal charge transfer point, the most prevalent species is the interchain polaron pair $P^+ + P^-$. This is consistent with a charge generation mechanism governed by a one-step electron transfer from the donor to the acceptor. However, since the configuration representing an exciton localised on the acceptor also exhibits a significant yield, we cannot exclude a contribution arising from a two-step process [68], whereby hole transfer to the donor follows exciton hopping to the acceptor.

Another important result is obtained when the band offset is such that higher-lying acceptor orbitals become closely matched to the LUMO of the donor, or when the energy difference between the HOMOs is lower than the band offset. In such cases, electronic transitions between the HOMO and LUMO of the donor and the acceptor orbitals close to the band edges increase in probability, which can lead to the reversal of the predominance of the interchain polaron pairs $P^+ + P^-$ and $P^- + P^+$, and requires adding higher-order states in order to capture the nature of the photoexcitation. The importance of these states is manifested in the dimerisation pattern as a significant broadening of the lattice distortions, and in the emergence of distinct regions in the results obtained for the average yields as a function of several parameters. We find that the higher-order configurations $P^+ + P_3^-$ and $Gr + Ex_3$ provide the most significant contributions, with average yields close to 10%.

Part IV

Conclusion

Chapter 9

Summary and outlook

We have developed a nonadiabatic molecular dynamics method, which allows for the coupled evolution of classical ions and of multiconfigurational electronic wavefunctions. The proposed scheme effectively establishes a compromise between efficiency and accuracy in the description of the coupled electron-nuclear dynamics and the excited electronic states, which enables the study of large systems. Furthermore, it is designed to take into account the appropriate spin symmetry of the electronic wavefunction, by retaining the smallest possible number of configurations that captures its essential features. This provides a powerful tool to study the dynamics of photoexcited states, and highlight the differences between singlet and triplet excited states, which can be quite significant.

By applying the formalism to the dynamics of low-lying excitations in a prototypical conjugated polymer, described by simple semiempirical models, both with and without Coulomb interactions, a number of important differences were uncovered. Our findings suggest that the inclusion of electron-electron interactions leads to an increased degree of localisation, both for polarons and photoexcited states. It also suppresses the phase oscillation process characteristic of the dynamics of photoexcitations, and enhances the charge oscillations associated with polaronic distortions. The most significant effect comes to light by comparing the evolutions of the lowest singlet and triplet excited states, which can only differ when Coulomb interactions are considered. Our results show that the degree of localisation and the amplitude of lattice distortion are much higher for the triplet state, which agrees well with

other theoretical investigations and experimental evidence [130–134].

Next, the method was employed to study the effect of interchain interactions on the dynamics of photoexcited states in a prototypical conjugated polymer, by considering a double-strand semiempirical model under different regimes of the interchain coupling strength. Our findings show that the degree of delocalisation across strands increases with the coupling strength, which suggests that interchain interactions play a fundamental role in determining the intra- or interchain character of the states produced upon photoexcitation. In the weak coupling regime, the photoexcitations keep to the strand where they are created. In the strong coupling limit, on the other hand, mirror-like dimerisation patterns are ultimately obtained for chains of the same length. By introducing a difference in chain length, this symmetry is lost and the lattice deformation becomes more pronounced on the longer chain, which reflects an increased hopping rate towards longer polymer strands, where the exciton energy is lower [61, 66].

The nature of the photoexcited states and the issue of charge photogeneration have also been discussed. Our results show that, in the case of conjugated polymers in dilute solution, for which the interchain interactions are weak, the $1\,^1B_u$ photoexcitation can be described by a polaron-exciton confined to a single strand, whereas the $2\,^1B_u$ state corresponds to an intrachain superposition with equal weights of exciton and oppositely charged polaron pairs. Most importantly, we have shown that the polarons of the intrachain superposition do not behave as free charges. In fact, this latter species behaves similarly to an exciton, since it can move between polymer strands as a whole entity, in addition to being dissociated into polaron pairs. For dense conjugated polymer films, the ultrafast processes of exciton hopping and dissociation into polaron pairs produce additional species, which are essential to fully characterise the photoexcited states, and become increasingly important with the interchain coupling strength. In the strong coupling limit, the yields of exciton-like intrachain configurations sum to about 35% for each strand (regardless of its initial state), while those of oppositely charged interchain polarons total some 25%. We are led to the conclusion that the charge carrier photogeneration yield varies between nearly zero in the weak coupling regime up to a maximum of about 25%

in the strong coupling limit and, thus, depends critically on the strength of interchain interactions. This result is in agreement with other theoretical predictions and experimental observations [39–42, 56].

Finally, we have studied the charge transfer dynamics at donor/acceptor interfaces, by varying several key parameters of a π-electron model with interchain interactions. Our findings suggest that the relative positions of the HOMOs and LUMOs obtained for the ground state of each strand can be used to predict the charge transfer mechanism and the nature of the species produced upon photoexcitation. Maximising the charge transfer requires fine-tuning of the band offset at the donor/acceptor interface, and depends critically on the strength of interchain interactions. In the most favourable case, oppositely charged interchain polarons account for about 50% of the character of the photoexcitation. The most prevalent species is likely produced via a one-step electron transfer from the donor to the acceptor, but a contribution arising from a two-step process [68], whereby hole transfer to the donor follows exciton hopping to the acceptor, cannot be excluded. When the band offset is such that higher-lying acceptor orbitals become closely matched to the LUMO of the donor, the contribution of higher-order polaronic states becomes vital to fully describe the nature of the photoexcitation. This is evidenced in the dimerisation pattern as a considerable broadening of the lattice deformations. Additionally, when the energy difference between the HOMOs is lower than the band offset, hole transfer from the donor to the acceptor can become the most favourable transfer mechanism, thus reversing the charges of the predominant polarons in the opposite strands. In this region, particularly for the strong coupling regime, the general trend is to level the yields of many configurations, with a notable increase in the contribution of higher-order states of excitonic character.

While the maximum value obtained for the total yield of interchain polaron pairs, of about 50% in the strong coupling limit, can explain the experimentally observed enhancement of the charge carrier photogeneration yield in certain polymer/fullerene composites [135], most technologically relevant cases exhibit a much more complete charge transfer process [30–32, 136]. A possible explanation for this discrepancy is the lack of further chains in the investigated donor/acceptor model to allow the

charges to escape from each other. An immediate extension of the work presented in this thesis is to include additional strands in the polymer heterojunction model. Not only would this allow us to clarify the extent of the charge transfer process, it would also make it possible to study the separation of charges prior to collection at the electrodes, which is the next step crucial to understanding the operation of polymer-based solar cells [33, 34, 37].

Another possible extension is to go beyond the mean-field approach in the description of the excited electronic states, through the use of a multiconfigurational formalism with *time-dependent coefficients*. This would allow us to model more rigorously the two-electron processes responsible for exciton transfer between molecules [66], which may be especially important to capture the correct flow of energy between polymer strands in the weak coupling regime. Including the effect of *spin-orbit coupling* [45, 61] is another interesting possibility. Although typically weak, this would allow transitions between singlet and triplet states, which for some systems could lead to very different dynamics.

It would also be interesting to go beyond the π-electron approximation, by considering *all-valence-electron* semiempirical methods [137], such as the *Austin model 1* (AM1) or *parametric method 3* (PM3). This would allow for more general movement of atoms, which could have important consequences for the dynamics. It would also provide a more realistic description of the excited electronic states, and possibly enable a direct comparison with experimental results. Another worthy research direction is to increase the level of accuracy in the description of the coupled electron-nuclear dynamics, by combining the multiconfigurational approach developed in this thesis with the method of *correlated electron-ion dynamics* [114, 116]. Including the quantum fluctuations of ions may open additional ultrafast vibrational decay pathways and produce rapid de-excitation of excitons, in which case the dynamics would be very different. The yields of the photogenerated species could be changed significantly, with profound impact on the performance of organic devices, such as polymer-based solar cells.

References

[1] C. K. Chiang, C. R. Fincher, Jr., Y. W. Park, A. J. Heeger, H. Shirakawa, E. J. Louis, S. C. Gau, and A. G. MacDiarmid, "Electrical conductivity in doped polyacetylene", *Physical Review Letters* **39**, 1098 (1977)

[2] H. Shirakawa, E. J. Louis, A. G. MacDiarmid, C. K. Chiang, and A. J. Heeger, "Synthesis of electrically conducting organic polymers: Halogen derivatives of polyacetylene, $(CH)_x$", *Journal of the Chemical Society, Chemical Communications*, 578 (1977)

[3] S. R. Forrest, "The path to ubiquitous and low-cost organic electronic appliances on plastic", *Nature* **428**, 911 (2004)

[4] J. R. Sheats, "Manufacturing and commercialization issues in organic electronics", *Journal of Materials Research* **19**, 1974 (2004)

[5] E. Smela, "Conjugated polymer actuators for biomedical applications", *Advanced Materials* **15**, 481 (2003)

[6] P. Novák, K. Müller, K. S. V. Santhanam, and O. Haas, "Electrochemically active polymers for rechargeable batteries", *Chemical Reviews* **97**, 207 (1997)

[7] O. Levi, G. Perepelitsa, D. Davidov, A. J. Agranat, I. Benjamin, S. Shalom, R. Neumann, and Y. Avny, "Holographic storage in conjugated-polymer composites", *Physical Review B* **57**, R12647 (1998)

[8] P. Andersson, M. Berggren, and T. Kugler, "Switchable optical polarizer based on electrochromism in stretch-aligned polyaniline", *Applied Physics Letters* **83**, 1307 (2003)

[9] N. Tessler, G. J. Denton, and R. H. Friend, "Lasing from conjugated-polymer microcavities", *Nature* **382**, 695 (1996)

[10] M. D. McGehee and A. J. Heeger, "Semiconducting (conjugated) polymers as materials for solid-state lasers", *Advanced Materials* **12**, 1655 (2000)

[11] Q. Pei, G. Yu, C. Zhang, Y. Yang, and A. J. Heeger, "Polymer light-emitting electrochemical cells", *Science* **269**, 1086 (1995)

[12] J. H. Burroughes, D. D. C. Bradley, A. R. Brown, R. N. Marks, K. Mackay, R. H. Friend, P. L. Burns, and A. B. Holmes, "Light-emitting diodes based on conjugated polymers", *Nature* **347**, 539 (1990)

[13] D. Braun and A. J. Heeger, "Visible light emission from semiconducting polymer diodes", *Applied Physics Letters* **58**, 1982 (1991)

[14] N. C. Greenham, S. C. Moratti, D. D. C. Bradley, R. H. Friend, and A. B. Holmes, "Efficient light-emitting diodes based on polymers with high electron affinities", *Nature* **365**, 628 (1993)

[15] R. H. Friend, R. W. Gymer, A. B. Holmes, J. H. Burroughes, R. N. Marks, C. Taliani, D. D. C. Bradley, D. A. dos Santos, J. L. Brédas, M. Lögdlund, and W. R. Salaneck, "Electroluminescence in conjugated polymers", *Nature* **397**, 121 (1999)

[16] L. Chen, D. W. McBranch, H.-L. Wang, R. Helgeson, F. Wudl, and D. G. Whitten, "Highly sensitive biological and chemical sensors based on reversible fluorescence quenching in a conjugated polymer", *Proceedings of the National Academy of Sciences of the United States of America* **96**, 12287 (1999)

[17] J. Janata and M. Josowicz, "Conducting polymers in electronic chemical sensors", *Nature Materials* **2**, 19 (2003)

[18] J. H. Burroughes, C. A. Jones, and R. H. Friend, "New semiconductor device physics in polymer diodes and transistors", *Nature* **335**, 137 (1988)

[19] H. Fuchigami, A. Tsumura, and H. Koezuka, "Polythienylenevinylene thin-film transistor with high carrier mobility", *Applied Physics Letters* **63**, 1372 (1993)

[20] C. D. Dimitrakopoulos and P. R. L. Malenfant, "Organic thin film transistors for large area electronics", *Advanced Materials* **14**, 99 (2002)

[21] G. Yu, J. Wang, J. McElvain, and A. J. Heeger, "Large-area, full-color image sensors made with semiconducting polymers", *Advanced Materials* **10**, 1431 (1998)

[22] T. Tani, P. M. Grant, W. D. Gill, G. B. Street, and T. C. Clarke, "Photo-transport effects in polyacetylene, $(CH)_x$", *Solid State Communications* **33**, 499 (1980)

[23] S. Glenis, G. Horowitz, G. Tourillon, and F. Garnier, "Electrochemically grown polythiophene and poly(3-methylthiophene) organic photovoltaic cells", *Thin Solid Films* **111**, 93 (1984)

[24] N. S. Sariciftci, D. Braun, C. Zhang, V. I. Srdanov, A. J. Heeger, G. Stucky, and F. Wudl, "Semiconducting polymer-buckminsterfullerene heterojunctions: Diodes, photodiodes, and photovoltaic cells", *Applied Physics Letters* **62**, 585 (1993)

[25] J. J. M. Halls, K. Pichler, R. H. Friend, S. C. Moratti, and A. B. Holmes, "Exciton diffusion and dissociation in a poly(*p*-phenylenevinylene)/C_{60} heterojunction photovoltaic cell", *Applied Physics Letters* **68**, 3120 (1996)

[26] G. Yu, J. Gao, J. C. Hummelen, F. Wudl, and A. J. Heeger, "Polymer photovoltaic cells: Enhanced efficiencies via a network of internal donor-acceptor heterojunctions", *Science* **270**, 1789 (1995)

[27] S. E. Shaheen, C. J. Brabec, N. S. Sariciftci, F. Padinger, T. Fromherz, and J. C. Hummelen, "2.5% efficient organic plastic solar cells", *Applied Physics Letters* **78**, 841 (2001)

[28] J. Y. Kim, S. H. Kim, H.-H. Lee, K. Lee, W. Ma, X. Gong, and A. J. Heeger, "New architecture for high-efficiency polymer photovoltaic cells using solution-based titanium oxide as an optical spacer", *Advanced Materials* **18**, 572 (2006)

[29] J. Y. Kim, K. Lee, N. E. Coates, D. Moses, T.-Q. Nguyen, M. Dante, and A. J. Heeger, "Efficient tandem polymer solar cells fabricated by all-solution processing", *Science* **317**, 222 (2007)

[30] S. H. Park, A. Roy, S. Beaupré, S. Cho, N. Coates, J. S. Moon, D. Moses, M. Leclerc, K. Lee, and A. J. Heeger, "Bulk heterojunction solar cells with internal quantum efficiency approaching 100%", *Nature Photonics* **3**, 297 (2009)

[31] Y. Liang, Z. Xu, J. Xia, S.-T. Tsai, Y. Wu, G. Li, C. Ray, and L. Yu, "For the bright future – Bulk heterojunction polymer solar cells with power conversion efficiency of 7.4%", *Advanced Materials* **22**, E135 (2010)

[32] J. You, L. Dou, K. Yoshimura, T. Kato, K. Ohya, T. Moriarty, K. Emery, C.-C. Chen, J. Gao, G. Li, and Y. Yang, "A polymer tandem solar cell with 10.6% power conversion efficiency", *Nature Communications* **4**, 1446 (2013)

[33] S. Günes, H. Neugebauer, and N. S. Sariciftci, "Conjugated polymer-based organic solar cells", *Chemical Reviews* **107**, 1324 (2007)

[34] C. Deibel and V. Dyakonov, "Polymer-fullerene bulk heterojunction solar cells", *Reports on Progress in Physics* **73**, 096401 (2010)

[35] N. S. Sariciftci, L. Smilowitz, A. J. Heeger, and F. Wudl, "Photoinduced electron transfer from a conducting polymer to buckminsterfullerene", *Science* **258**, 1474 (1992)

[36] N. S. Sariciftci and A. J. Heeger, "Reversible, metastable, ultrafast photoinduced electron transfer from semiconducting polymers to buckminsterfullerene and in the corresponding donor/acceptor heterojunctions", *International Journal of Modern Physics B* **8**, 237 (1994)

[37] J.-L. Brédas, J. E. Norton, J. Cornil, and V. Coropceanu, "Molecular understanding of organic solar cells: The challenges", *Accounts of Chemical Research* **42**, 1691 (2009)

[38] N. S. Sariciftci (Ed.), *Primary photoexcitations in conjugated polymers: Molecular exciton versus semiconductor band model*, World Scientific: Singapore (1998)

[39] D. Moses, A. Dogariu, and A. J. Heeger, "Ultrafast detection of charged photocarriers in conjugated polymers", *Physical Review B* **61**, 9373 (2000)

[40] I. B. Martini, A. D. Smith, and B. J. Schwartz, "Exciton-exciton annihilation and the production of interchain species in conjugated polymer films: Comparing the ultrafast stimulated emission and photoluminescence dynamics of MEH-PPV", *Physical Review B* **69**, 035204 (2004)

[41] P. B. Miranda, D. Moses, and A. J. Heeger, "Ultrafast photogeneration of charged polarons on conjugated polymer chains in dilute solution", *Physical Review B* **70**, 085212 (2004)

[42] C.-X. Sheng, M. Tong, S. Singh, and Z. V. Vardeny, "Experimental determination of the charge/neutral branching ratio η in the photoexcitation of π-conjugated polymers by broadband ultrafast spectroscopy", *Physical Review B* **75**, 085206 (2007)

[43] Z. An, C. Q. Wu, and X. Sun, "Dynamics of photogenerated polarons in conjugated polymers", *Physical Review Letters* **93**, 216407 (2004)

[44] A. J. Heeger, S. Kivelson, J. R. Schrieffer, and W. P. Su, "Solitons in conducting polymers", *Reviews of Modern Physics* **60**, 781 (1988)

[45] W. Barford, *Electronic and optical properties of conjugated polymers*, Clarendon Press: Oxford (2005)

[46] S. Roth and D. Carroll, *One-dimensional metals: Conjugated polymers, organic crystals, carbon nanotubes*, Wiley: Weinheim (2004)

[47] W. P. Su and J. R. Schrieffer, "Soliton dynamics in polyacetylene", *Proceedings of the National Academy of Sciences of the United States of America* **77**, 5626 (1980)

[48] E. J. Mele, "Transient structural response to photoexcitation in polyacetylene", *Physical Review B* **26**, 6901 (1982)

[49] S. R. Phillpot, A. R. Bishop, and B. Horovitz, "Amplitude breathers in conjugated polymers", *Physical Review B* **40**, 1839 (1989)

[50] H. W. Streitwolf, "Dynamics of a bond-disordered Peierls chain and mixed gap states", *Physical Review B* **58**, 14356 (1998)

[51] P. H. de Oliveira Neto, W. F. da Cunha, R. Gargano, and G. M. e Silva, "Dynamics of photoexcitations with interchain coupling in conjugated polymers", *International Journal of Quantum Chemistry* **108**, 2442 (2008)

[52] C. L. Wang and F. Martino, "Photogenerated exciton-breather state in *trans*-polyacetylene", *Physical Review B* **34**, 5540 (1986)

[53] W. Förner and W. Utz, "Nonlinear charge carriers in polyacetylene", *Journal of Molecular Modeling* **4**, 12 (1998)

[54] A. Yamashiro and A. Takahashi, "Photoexcitation and relaxation processes in polyacetylene", *Journal of the Physical Society of Japan* **67**, 2938 (1998)

[55] S. Tretiak, A. Saxena, R. L. Martin, and A. R. Bishop, "Photoexcited breathers in conjugated polyenes: An excited-state molecular dynamics study", *Proceedings of the National Academy of Sciences of the United States of America* **100**, 2185 (2003)

[56] Y. Meng, B. Di, X. J. Liu, Z. An, and C. Q. Wu, "Interchain coupling effects on dynamics of photoexcitations in conjugated polymers", *Journal of Chemical Physics* **128**, 184903 (2008)

[57] A. R. Blythe and D. Bloor, *Electrical properties of polymers*, Cambridge University Press: Cambridge (2005)

[58] M. Tinkham, *Group theory and quantum mechanics*, McGraw-Hill: New York (1964)

[59] C. Soci, *Elementary photoexcitations in conjugated polymers studied by optical spectroscopy and photoconductivity*, PhD thesis, University of Pavia (2005)

[60] B. E. Kohler, C. Spangler, and C. Westerfield, "The $2\,^1A_g$ state in the linear polyene 2,4,6,8,10,12,14,16-octadecaoctaene", *Journal of Chemical Physics* **89**, 5422 (1988)

[61] M. Pope and C. E. Swenberg, *Electronic processes in organic crystals and polymers*, Oxford University Press: Oxford (1999)

[62] R. Kersting, U. Lemmer, R. F. Mahrt, K. Leo, H. Kurz, H. Bässler, and E. O. Göbel, "Femtosecond energy relaxation in π-conjugated polymers", *Physical Review Letters* **70**, 3820 (1993)

[63] G. Lanzani, G. Cerullo, C. Brabec, and N. S. Sariciftci, "Time domain investigation of the intrachain vibrational dynamics of a prototypical light-emitting conjugated polymer", *Physical Review Letters* **90**, 047402 (2003)

[64] C. Gadermaier, G. Cerullo, C. Manzoni, U. Scherf, E. J. W. List, and G. Lanzani, "Dynamics of higher photoexcited states in m-LPPP probed with sub-20 fs time resolution", *Chemical Physics Letters* **384**, 251 (2004)

[65] C. Gadermaier and G. Lanzani, "Photophysics of conjugated polymers: The contribution of ultrafast spectroscopy", *Journal of Physics: Condensed Matter* **14**, 9785 (2002)

[66] Th. Förster, "10th Spiers memorial lecture – Transfer mechanisms of electronic excitation", *Discussions of the Faraday Society* **27**, 7 (1959)

[67] C. J. Brabec, G. Zerza, G. Cerullo, S. de Silvestri, S. Luzzati, J. C. Hummelen, and S. Sariciftci, "Tracing photoinduced electron transfer process in conjugated polymer/fullerene bulk heterojunctions in real time", *Chemical Physics Letters* **340**, 232 (2001)

[68] M. T. Lloyd, Y.-F. Lim, and G. G. Malliaras, "Two-step exciton dissociation in poly(3-hexylthiophene)/fullerene heterojunctions", *Applied Physics Letters* **92**, 143308 (2008)

[69] E. Hückel, "Quantentheoretische beiträge zum benzolproblem. I. Die elektronenkonfiguration des benzols und verwandter verbindungen", *Zeitschrift für Physik* **70**, 204 (1931)

[70] E. Hückel, "Quantentheoretische beiträge zum problem der aromatischen und ungesättigten verbindungen. III.", *Zeitschrift für Physik* **76**, 628 (1932)

[71] S. Risser, S. Klemm, D. W. Allender, and M. A. Lee, "Hückel model calculations of polarizability and hyperpolarizability for conjugated molecules", *Molecular Crystals and Liquid Crystals* **150b**, 631 (1987)

[72] B. E. Kohler, "A simple model for linear polyene electronic structure", *Journal of Chemical Physics* **93**, 5838 (1990)

[73] R. E. Peierls, *Quantum theory of solids*, Clarendon Press: Oxford (1955)

[74] R. Pariser and R. G. Parr, "A semi-empirical theory of the electronic spectra and electronic structure of complex unsaturated molecules. I.", *Journal of Chemical Physics* **21**, 466 (1953)

[75] R. Pariser and R. G. Parr, "A semi-empirical theory of the electronic spectra and electronic structure of complex unsaturated molecules. II.", *Journal of Chemical Physics* **21**, 767 (1953)

[76] J. A. Pople, "Electron interaction in unsaturated hydrocarbons", *Transactions of the Faraday Society* **49**, 1375 (1953)

[77] Y. Tanabe, "Electronic structure of conductive and conjugated polymers", *in* Y. Tanabe (Ed.), *Macromolecular science and engineering: New aspects*, Springer: Berlin (1999)

[78] K. Schulten and M. Karplus, "On the origin of a low-lying forbidden transition in polyenes and related molecules", *Chemical Physics Letters* **14**, 305 (1972)

[79] K. Schulten, I. Ohmine, and M. Karplus, "Correlation effects in the spectra of polyenes", *Journal of Chemical Physics* **64**, 4422 (1976)

[80] M. Chandross, S. Mazumdar, S. Jeglinski, X. Wei, Z. V. Vardeny, E. W. Kwock, and T. M. Miller, "Excitons in poly(*para*-phenylenevinylene)", *Physical Review B* **50**, 14702 (1994)

[81] M. Chandross, S. Mazumdar, M. Liess, P. A. Lane, Z. V. Vardeny, M. Hamaguchi, and K. Yoshino, "Optical absorption in the substituted phenylene-based conjugated polymers: Theory and experiment", *Physical Review B* **55**, 1486 (1997)

[82] W. P. Su, J. R. Schrieffer, and A. J. Heeger, "Solitons in polyacetylene", *Physical Review Letters* **42**, 1698 (1979)

[83] W. P. Su, J. R. Schrieffer, and A. J. Heeger, "Soliton excitations in polyacetylene", *Physical Review B* **22**, 2099 (1980)

[84] S. A. Brazovskiĭ and N. N. Kirova, "Excitons, polarons, and bipolarons in conducting polymers", *JETP Letters* **33**, 4 (1981)

[85] A. R. Bishop, D. K. Campbell, and K. Fesser, "Polyacetylene and relativistic field theory models", *Molecular Crystals and Liquid Crystals* **77**, 253 (1981)

[86] C. L. Wang, Z. B. Su, and F. Martino, "Bipolaron dynamics in nearly degenerate quasi-one-dimensional polymers", *Physical Review B* **33**, 1512 (1986)

[87] M. Hultell and S. Stafström, "Impact of ring torsion on the intrachain mobility in conjugated polymers", *Physical Review B* **75**, 104304 (2007)

[88] M. Hultell and S. Stafström, "Impact of ring torsion dynamics on intrachain charge transport in conjugated polymers", *Physical Review B* **79**, 014302 (2009)

[89] S. T. Epstein, *The variation method in quantum chemistry*, Academic Press: New York (1974)

[90] R. McWeeny, *Methods of molecular quantum mechanics*, Academic Press: London (1989)

[91] W. H. Press, S. A. Teukolsky, W. T. Vetterling, and B. P. Flannery, *Numerical recipes in C: The art of scientific computing*, Cambridge University Press: Cambridge (1992)

[92] D. J. Thouless, *The quantum mechanics of many-body systems*, Academic Press: New York (1972)

[93] J. P. Dahl, H. Johansen, D. R. Truax, and T. Ziegler, "On the derivation of necessary conditions on Hartree-Fock orbitals", *Chemical Physics Letters* **6**, 64 (1970)

[94] F. W. Bobrowicz and W. A. Goddard, III, "The self-consistent field equations for generalized valence bond and open-shell Hartree-Fock wave functions", *in* H. F. Schaefer, III (Ed.), *Methods of electronic structure theory*, Plenum Press: New York (1977)

[95] W. D. Edwards and M. C. Zerner, "A generalized restricted open-shell Fock operator", *Theoretica Chimica Acta* **72**, 347 (1987)

[96] C. Kollmar, "Convergence optimization of restricted open-shell self-consistent field calculations", *International Journal of Quantum Chemistry* **62**, 617 (1997)

[97] G. Karl and V. A. Novikov, "Variational estimates for excited states", *Physical Review D* **51**, 5069 (1995)

[98] M. F. Guest and V. R. Saunders, "On methods for converging open-shell Hartree-Fock wave-functions", *Molecular Physics* **28**, 819 (1974)

[99] B. N. Plakhutin, E. V. Gorelik, and N. N. Breslavskaya, "Koopmans' theorem in the ROHF method: Canonical form for the Hartree-Fock Hamiltonian", *Journal of Chemical Physics* **125**, 204110 (2006)

[100] C. C. J. Roothaan, "New developments in molecular orbital theory", *Reviews of Modern Physics* **23**, 69 (1951)

[101] G. G. Hall, "The molecular orbital theory of chemical valency. VIII. A method of calculating ionization potentials", *Proceedings of the Royal Society A* **205**, 541 (1951)

[102] D. H. Sleeman, "The determination of SCF LCAO solutions for open shell configurations", *Theoretica Chimica Acta* **11**, 135 (1968)

[103] J. Koutecký and V. Bonačić, "On convergence difficulties in the iterative Hartree-Fock procedure", *Journal of Chemical Physics* **55**, 2408 (1971)

[104] D. R. Hartree, *The calculation of atomic structures*, John Wiley & Sons: New York (1957)

[105] V. R. Saunders and I. H. Hillier, "A «level-shifting» method for converging closed shell Hartree-Fock wave functions", *International Journal of Quantum Chemistry* **7**, 699 (1973)

[106] P. Pulay, "Improved SCF convergence acceleration", *Journal of Computational Chemistry* **3**, 556 (1982)

[107] I. V. Ionova and E. A. Carter, "Error vector choice in direct inversion in the iterative subspace method", *Journal of Computational Chemistry* **17**, 1836 (1996)

[108] J. Douady, Y. Ellinger, R. Subra, and B. Levy, "Exponential transformation of molecular orbitals: A quadratically convergent SCF procedure. I. General formulation and application to closed-shell ground states", *Journal of Chemical Physics* **72**, 1452 (1980)

[109] T. H. Fischer and J. Almlöf, "General methods for geometry and wave function optimization", *Journal of Physical Chemistry* **96**, 9768 (1992)

[110] J. Nocedal, "Updating quasi-Newton matrices with limited storage", *Mathematics of Computation* **35**, 773 (1980)

[111] J. C. Tully, "Nonadiabatic dynamics", *in* D. L. Thompson (Ed.), *Modern methods for multidimensional dynamics computations in chemistry*, World Scientific: Singapore (1998)

[112] M. Griebel, S. Knapek, and G. Zumbusch, *Numerical simulation in molecular dynamics: Numerics, algorithms, parallelization, applications*, Springer: Berlin (2007)

[113] H. Goldstein, *Classical mechanics*, Addison-Wesley: Cambridge, Massachusetts (1950)

[114] A. P. Horsfield, D. R. Bowler, A. J. Fisher, T. N. Todorov, and C. G. Sánchez, "Beyond Ehrenfest: Correlated non-adiabatic molecular dynamics", *Journal of Physics: Condensed Matter* **16**, 8251 (2004)

[115] F. Sterpone, M. J. Bedard-Hearn, and P. J. Rossky, "Nonadiabatic mixed quantum-classical dynamic simulation of π-stacked oligophenylenevinylenes", *Journal of Physical Chemistry A* **113**, 3427 (2009)

[116] L. Stella, R. P. Miranda, A. P. Horsfield, and A. J. Fisher, "Analog of Rabi oscillations in resonant electron-ion systems", *Journal of Chemical Physics* **134**, 194105 (2011)

[117] H. Tamura, J. G. S. Ramon, E. R. Bittner, and I. Burghardt, "Phonon-driven ultrafast exciton dissociation at donor-acceptor polymer heterojunctions", *Physical Review Letters* **100**, 107402 (2008)

[118] P.-G. Reinhard, "A comment on time-dependent variational principles", *Zeitschrift für Physik A* **280**, 281 (1977)

[119] P.-O. Löwdin, "Quantum theory of many-particle systems. I. Physical interpretations by means of density matrices, natural spin-orbitals, and convergence problems in the method of configurational interaction", *Physical Review* **97**, 1474 (1955)

[120] J. Zanghellini, M. Kitzler, C. Fabian, T. Brabec, and A. Scrinzi, "An MCTDHF approach to multielectron dynamics in laser fields", *Laser Physics* **13**, 1064 (2003)

[121] T. Kato and H. Kono, "Time-dependent multiconfiguration theory for electronic dynamics of molecules in an intense laser field", *Chemical Physics Letters* **392**, 533 (2004)

[122] J. Caillat, J. Zanghellini, M. Kitzler, O. Koch, W. Kreuzer, and A. Scrinzi, "Correlated multielectron systems in strong laser fields: A multiconfiguration time-dependent Hartree-Fock approach", *Physical Review A* **71**, 012712 (2005)

[123] M. Nest, T. Klamroth, and P. Saalfrank, "The multiconfiguration time-dependent Hartree-Fock method for quantum chemical calculations", *Journal of Chemical Physics* **122**, 124102 (2005)

[124] O. E. Alon, A. I. Streltsov, and L. S. Cederbaum, "Unified view on multiconfigurational time propagation for systems consisting of identical particles", *Journal of Chemical Physics* **127**, 154103 (2007)

[125] E. Hairer, S. P. Nørsett, and G. Wanner, *Solving ordinary differential equations I: Nonstiff problems*, Springer: Berlin (1987)

[126] J. T. Gammel, D. K. Campbell, S. Mazumdar, S. N. Dixit, and E. Y. Loh, Jr., "Determination of interaction parameters in Peierls-Hubbard models describing finite polyenes and polyacetylene", *Synthetic Metals* **43**, 3471 (1991)

[127] K. Rościszewski and B. Oleś, "A comment on the charge excitation gap for polyacetylene", *Journal of Physics: Condensed Matter* **5**, 7289 (1993)

[128] H. Meider and M. Springborg, "Constrained density-functional calculations for delocalized electrons: Hubbard parameters for polyacetylene", *Chemical Physics Letters* **300**, 339 (1999)

[129] A. Köhler and D. Beljonne, "The singlet-triplet exchange energy in conjugated polymers", *Advanced Functional Materials* **14**, 11 (2004)

[130] D. Beljonne, Z. Shuai, R. H. Friend, and J. L. Brédas, "Theoretical investigation of the lowest singlet and triplet states in poly(paraphenylene vinylene) oligomers", *Journal of Chemical Physics* **102**, 2042 (1995)

[131] D. Beljonne, H. F. Wittmann, A. Köhler, S. Graham, M. Younus, J. Lewis, P. R. Raithby, M. S. Khan, R. H. Friend, and J. L. Brédas, "Spatial extent of the singlet and triplet excitons in transition metal-containing poly-ynes", *Journal of Chemical Physics* **105**, 3868 (1996)

[132] A. P. Monkman, H. D. Burrows, I. Hamblett, S. Navarathnam, M. Svensson, and M. R. Andersson, "The effect of conjugation length on triplet energies, electron delocalization and electron-electron correlation in soluble polythiophenes", *Journal of Chemical Physics* **115**, 9046 (2001)

[133] A. Köhler, J. S. Wilson, R. H. Friend, M. K. Al-Suti, M. S. Khan, A. Gerhard, and H. Bässler, "The singlet-triplet energy gap in organic and Pt-containing phenylene ethynylene polymers and monomers", *Journal of Chemical Physics* **116**, 9457 (2002)

[134] Y. Liu, S. Jiang, K. Glusac, D. H. Powell, D. F. Anderson, and K. S. Schanze, "Photophysics of monodisperse platinum-acetylide oligomers: Delocalization in the singlet and triplet excited states", *Journal of the American Chemical Society* **124**, 12412 (2002)

[135] J. Piris, T. E. Dykstra, A. A. Bakulin, P. H. M. van Loosdrecht, W. Knulst, M. T. Trinh, J. M. Schins, and L. D. A. Siebbeles, "Photogeneration and ultrafast dynamics of excitons and charges in P3HT/PCBM blends", *Journal of Physical Chemistry C* **113**, 14500 (2009)

[136] J. Guo, H. Ohkita, H. Benten, and S. Ito, "Charge generation and recombination dynamics in poly(3-hexylthiophene)/fullerene blend films with different regioregularities and morphologies", *Journal of the American Chemical Society* **132**, 6154 (2010)

[137] J. A. Pople and D. L. Beveridge, *Approximate molecular orbital theory*, McGraw-Hill: New York (1972)